Liquid Metal Embrittlement of Advanced High Strength Steels during Resistance Spot Welding

Soma Csaba Simon
Student Number: 5953529
Date of Defense: August 22, 2025

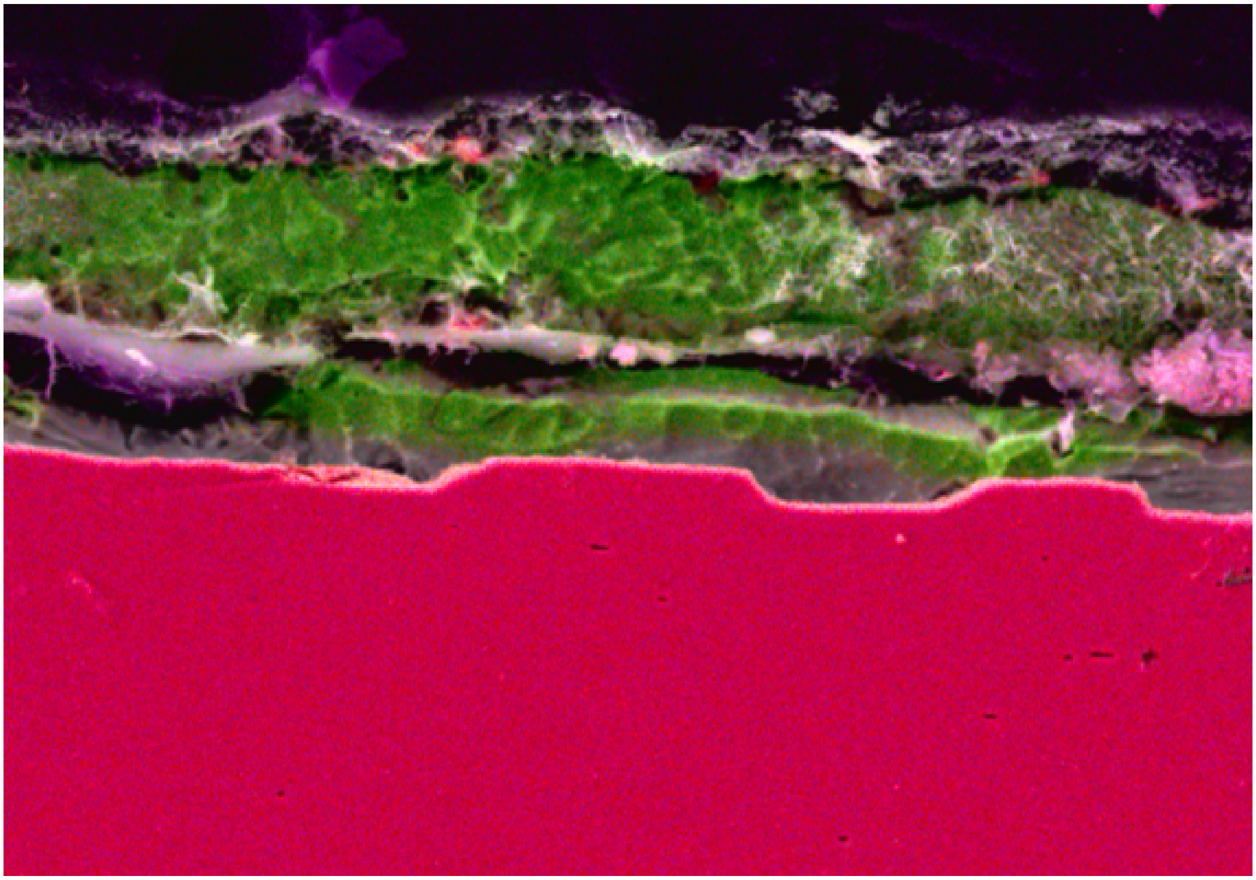

Liquid Metal Embrittlement of Advanced High Strength Steels during Resistance Spot Welding

Soma Csaba Simon
Delft University of Technology
Department of Materials Science and Engineering

Student number:	5953529
Project duration:	December 1, 2024 – August 22, 2025
Supervisor	Marcel Hermans
P.h.D. Supervisor	Gautham Mahadevan

Thesis committee:	Dr. ir. M.J.M. Hermans,	TU Delft, supervisor
	Dr. ing. Y. Ma,	TU Delft
	ir. G. Mahadevan,	TU Delft, supervisor

Contents

1 Introduction 6

2 Theoretical background 8

2.1 Resistance Spot Welding . . . 8
2.2 Twinning Induced Plasticity Steel (TWIP) . . . 11
  2.2.1 Plasticity Mechanisms and Texture of TWIP Steels . . . 12
  2.2.2 Mechanisms for mechanical property improvement . . . 13
  2.2.3 Formability of the steel grade . . . 13
2.3 Liquid Metal Embrittlement (LME) . . . 13
  2.3.1 Factors affecting LME . . . 14
  2.3.2 Mechanism . . . 16
  2.3.3 Ductile-Fracture Models . . . 16
  2.3.4 Grain Boundary-based Models . . . 18
  2.3.5 Brittle-Fracture Models . . . 18
  2.3.6 Dissolution-Condensation Mechanism (DCM) . . . 18
  2.3.7 LME in Fe-Zn System . . . 19
  2.3.8 Experimental method for Fe-Zn system . . . 19
  2.3.9 Predicting LME . . . 20
  2.3.10 Principal observations of LME . . . 20
2.4 Liquid Metal Embrittlement for Spot Welded High-Strength Steels . . . 20
  2.4.1 Factors Influencing LME . . . 21
  2.4.2 Experimental Procedure and Results . . . 21
  2.4.3 Possible Mitigation Methods . . . 23
2.5 Research questions . . . 24

3 Materials, Processing, Characterisation Methodology 25

3.1 Base material and weldments . . . 25
  3.1.1 Welding . . . 25
3.2 Sample preparation . . . 26
3.3 Etching . . . 27
3.4 Characterisation of the Samples . . . 27
  3.4.1 Optical Microscopy . . . 27
  3.4.2 Scanning Electron Microscopy . . . 28
  3.4.3 EDS Technique Overview . . . 28
  3.4.4 EBSD Technique overview . . . 28

4 Results 29

4.1 Base material overview . . . 29
  4.1.1 EDS of the Base Material . . . 29
  4.1.2 EBSD of the Base Material . . . 30
4.2 Optical microscopy . . . 32
  4.2.1 Double Sheet Samples . . . 32
  4.2.2 Triple Sheet Samples . . . 32
4.3 EDS . . . 37
4.4 SEM of welds . . . 37
4.5 EBSD . . . 41

5 Discussion **50**
5.1 Optical Microscopy and SEM results 50
5.2 EDS results 51
5.3 EBSD results 51
5.4 Potential underlying processes and causes 52

6 Conclusion **61**

7 Appendix **68**
7.1 Electrode shapes 68
7.2 Power supply components 68
7.3 Types of High Strength Steels discussed in length 68
7.3.1 Dual-Phase (DP) steels 69
7.3.2 Complex-Phase (CP) Steels 69
7.3.3 Martensitic (MS) Steels 69
7.3.4 Ferritic-Bainitic (FB) Steels 69
7.3.5 Transformation-Induced Plasticity (TRIP) Steels 69
7.4 Hot-Formed (HF) Steels 70
7.5 List of Systems Susceptible to LME 70
7.6 Grain size distribution diagrams for EBSD measurement of HTT samples 71
7.6.1 Grain size distribution diagrams - Area 72
7.6.2 Grain size distribution diagrams - Number fraction 73

Nomenclature

Symbol / Abbreviation	Description
A_g	Uniform elongation
A_{80}	Total elongation over 80 mm gauge length
AHSS	Advanced high-strength steels
Al	Aluminium
C	Carbon
Ce	Cerium
CI	Confidence Index
Cr	Chromium
Cu	Copper
°C	Degrees Celsius
°C/s	Degrees Celsius per second
DCM	Dissolution-Condensation Mechanism
DP	Dual Phase (steel grade)
EDS	Energy Dispersive Spectroscopy
EBSD	Electron Backscatter Diffraction
EG	Electro-Galvanized
FEM	Finite Element Simulations
FEA	Finite Element Analysis
Fe	Iron
F_e	Electrode Force/Pressure [kN]
fcc	Face-Centered Cubic
GA	Galvannealed
GALOP	Grooving Accelerated by Local Plasticity
GI	Hot-dip Galvanized
HAGB	High-Angle Grain Boundary
HAZ	Heat Affected Zone
HCl	Hydrogen Chloride
HT	Hold Time
Hz	Hertz
IPF	Inverse Pole Figure
I_w	Welding Current [kA]
K	Kelvin
kA	Kiloampere
kN	KiloNewton
LCS	Low Carbon Steel
LME	Liquid Metal Embrittlement

Symbol / Abbreviation	**Description**
Mn	Manganese
Mo	Molybdenium
MPa	Megapascal
ms	Millisecond
N	Nitrogen
Ni	Nickel
OM	Optical Microscopy
Q_A	Heat dissipated via natural convection and thermal radiation
Q_E	Heat dissipated via conduction to the electrodes
Q_Q	Heat dissipated via conduction within the material
Q_W	Heat dissipated via forced convection
Q&P	Quenching and Partitioning
RGM	Robertson-Glickman Model
RSW	Resistance Spot Welding
s^{-1}	Per second
SEM	Scanning Electron Microscopy
SFE	Stacking Fault Energy
Si	Silicon
t	Welding time [s]
Ti	Titanium
TRIP	Transformation Induced Plasticity (steel grade)
TWIP	Twinning Induced Plasticity (steel grade)
μm	Micrometer
V	Vanadium
w%	Weight percent
Zn	Zinc
Zr	Zirconium

1. Introduction

Advanced high-strength steels (AHSSs) are a crucial material source for the automotive industry, mainly for their combination of formability, strength, and cost-effectiveness [1]. This combination enables manufacturers to meet the strict safety standards of the industry while also keeping the weight of the vehicle low enough to meet the fuel economy targets, all without compromising the structural integrity of the vehicle [1]. This weight reduction and the resulting fuel efficiency also reduces greenhouse gas emission levels, leading to a lower carbon footprint [1]. In addition, passenger safety is also enhanced by the superior crashworthiness of vehicles made from such steel grades [1]. This is due to the high deformation resistance and energy absorption capabilities of the steel grade, which also allow a pathway to complex designs, which are not rare in the automotive industry [2].

Current research studies focus on optimizing processing methods and microstructure of AHSS, with the aim to further improve this grades' property and addressing current challenges such as hole expansion or springback [2].

Resistance spot welding (RSW) is a crucial joining method used in the automotive industry because of the efficiency of this technique. The principle of RSW is the creation of local melting of the plates to be joined, i.e., formation of a weld nugget, by passing through a current resulting in resistance/Joule heating, primarily at the interface. When the process is complete, the liquid solidifies, forming a solid bond. The quality of the weld is strongly affected by the selected welding parameters. [3]. A specific set of welding parameters result in the optimal weld strength, while using excessive current (heat input generated) results in cracking of the heat affected zone, or in the nugget itself [3].

Understanding and utilizing the relations between welding conditions and quality is essential and critical to ensuring the structural integrity of AHSS automotive applications [3].

The AHSS grades are typically galvanized for corrosion protection. However, the low melting point of zinc results in liquid zinc being present at the surface of the plates during the welding process, potentially penetrating the solid steel grain boundaries. This intergranular penetration of the zinc, in combination with stresses introduced by the welding process, may cause subsequent cracking. This phenomenon is referred to as liquid metal embrittlement (LME), which poses a serious threat by challenging the structural integrity of zinc-coated AHSS grades [4].]. The mechanisms involved in LME are not yet fully understood. However, it is essential to mitigate their effect in order to achieve the full potential of resistance spot welded AHSS in the automotive industry [4].

This thesis investigates the effects of hold time on the presence of LME in a high-manganese content TWIP steel grade. This topic has not received sufficient academic attention thus far, as mainly other welding parameters, such as the welding time, the welding current, or electrode forces were reviewed in prior groundwork. Even if hold time and its effect were briefly mentioned in a few studies, there has not been a comprehensive large-scale investigation, evaluating how it affects the microstructural, crack morphological and chemical content of samples with different hold times.

This topic is of urgent practical relevance, as TWIP steel grades could be the next step in producing more efficient and safer vehicles. Albeit this steel grade is highly sought-after in the industry, at the moment it is not used due to its susceptibility towards LME when using RSW. According to Beal [5], a sufficient amount of austenite in the steel is required for cracks to occur, which makes TWIP steels especially susceptible. The presence of liquid zinc compromises the mechanical integrity of steels by reducing ductility and propagating crack formation under specific stress and temperature conditions [5]. The effect of temperature and stress rate is further studied by Beal et al. [6], delving into zinc caused LME in high-manganese content TWIP steels, a ductility trough was established. This is a temperature range where severe embrittlement is present. The paper shows that LME is dependent at the strain rates, as lower strain rates result in no significant LME, while it also presents an intergranular fracture mode throughout the process. In automotive industry applications, high temperature, high strain rate, high stresses, and a short exposure time to zinc are all present, making TWIP steels especially prone to LME during vehicle production [6].

The thesis also focuses on the evaluation of samples with different holding time values, using several microscopical analysation techniques, followed by the comparison and assessment of the results. Based on the result or the analyses, a comprehensive guideline details the effect of hold time on LME in TWIP steels when welded with RSW process. Studying this question is important both as a conversation starter in the scientific community about the apparent importance of hold time, urging more in-depth analysis of this parameter, as well as allowing vehicle manufacturers to put these materials to use in a safe and standardized manner, by controlling for potential pitfalls in the production process.

2. Theoretical background

In this chapter the resistance spot welding process is introduced, and details are provided on the advanced high strength Twinning Induced Plasticity (TWIP) steels, in sections 2.1. and 2.2 respectively. The phenomenon of liquid metal embrittlement in general and of galvanised steel in particular are described in section 2.3.

2.1. Resistance Spot Welding

Resistance spot welding (RSW) is a method that utilizes an electrical current to generate Joule heating. This leads to local melting of the base metal and ultimately to bonding upon solidification [7]. Joule's Law of heating governs this process, where a localized high current density at the contact resistance points induces the metal melting [8].

In the joining process the metal sheets to be welded are clamped with a certain force between two water cooled electrodes, see Figure2.1. At this stage, a high current of approximately 1-10 kA at a low voltage of around 1-30 V is applied for a typical time of 100 ms. At the location of higher resistance where the most heat is generated, i.e. the interface between the two sheets and the interfaces between electrodes and the sheet surfaces, temperature increase is manifested. In particular, at the sheet-sheet interface as the locations of the electrodes are strongly cooled. This will result in melting and the formation of a weld nugget. This is also shown in Figure2.1.

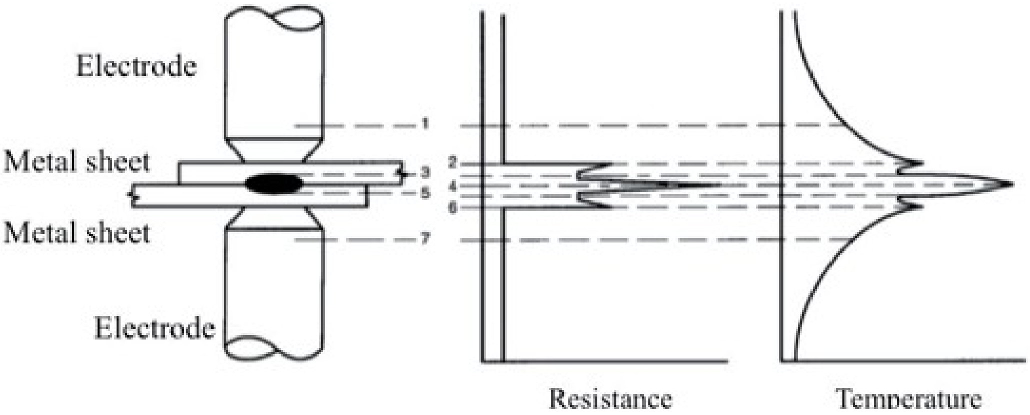

Figure 2.1. Resistance and Temperature values along the welding setup [9]

The total power generated can be calculated by Equation 2.1:

$$P = IV = I^2R = V^2/R \tag{2.1}$$

- P = Power
- I = Current through resistor
- V = Voltage
- R = Resistance

with P the power, I the current (A), V the voltage (V) and R_{tot} the total resistance of the system (Ω). The total resistance is comprised of resistance over the electrode material (R_{el}), the resistance at the interfaces electrode-sheets surface (R_{el-ss}) and the resistance at the interface between the sheets (R_{s-s}).

The process involves the clamping of metallic sheets between a pair of electrodes, through which a high electrical current (1-10 kA) is discharged at low voltages (1-30 V). This resistive heating generates a localized weld nugget at the interface of the metallic sheets, where the temperature reaches its maximum. The total electrical resistance of the system is a composite of the electrode-sheet interface resistance, the bulk resistivity of the sheet material, and the sheet-to-sheet contact resistance [7]. A schematic representation of the RSW process cycle is presented in Figure 2.2.

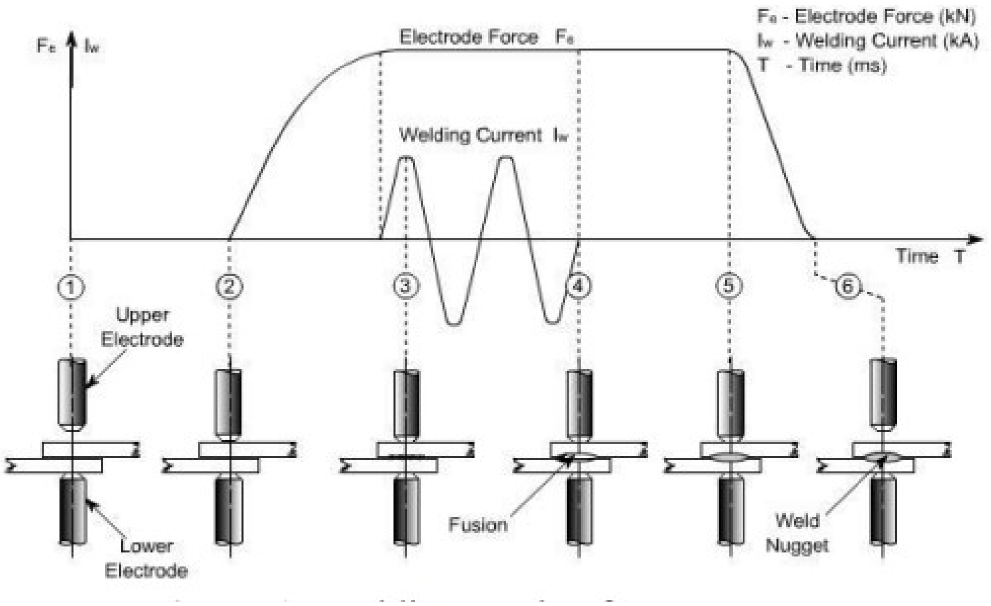

Figure 2.2. Process sequence indicating the welding cycle [10]

The quality of the weld and the bond strength in the welding process, schematically shown in Figure2.2, are significantly impacted by a list of parameters:

Welding force/pressure (F_e): The welding force impacts the overall system resistance, with this being especially present at the interfaces. Equation **??** indicates that if the resistance is reduced, less heat is generated locally. This effect should be eventually compensated by an increase in current to create a sufficiently large nugget. The force is applied at $t2$, the start of the squeeze stage shown in Figure2.2, and is maintained during the welding time ($t3$ to $t4$) until the end of the hold time ($t4$ to $t6$). In the last part from $t5$ to $t6$, the load is gradually released [10]. Note, however, that as the material becomes softer as temperature increases, this could result in unacceptable indentations at higher force levels.

Welding current (I_w): The welding current influences the heat generated throughout the process. The current is applied during the weld time ($t3$-$t4$). The amount for heat generated is also directly linked to the weld time. Figure2.3 indicates that a certain minimum current is required to achieve an appropriate nugget size from a mechanical performance perspective [10] [7].

Welding time (t): As mentioned, the weld time combined with current dictates the amount of heat generated. During the weld time the nugget of liquid metal at the interface between the sheets will grow [10]. If the time becomes too long, the liquid metal may escape, resulting in expulsion [12].

Base material properties: Mostly temperature related properties, such as resistivity, heat capacity and thermal conductivity, also affecting heat generation during RSW [10].

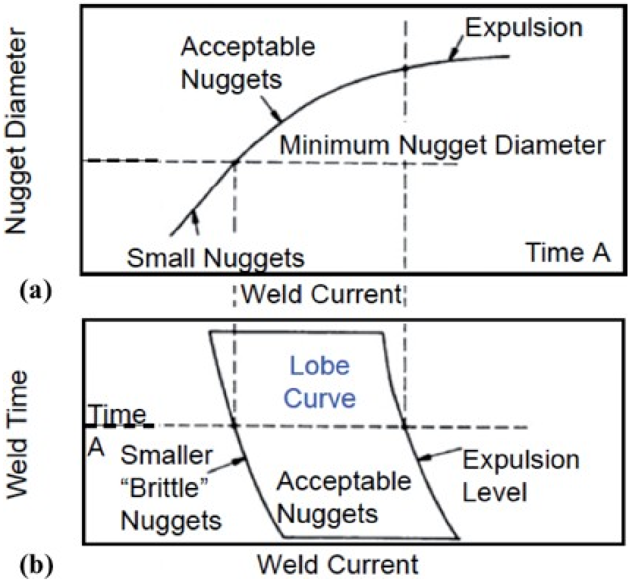

Figure 2.3. relationship between welding current and nugget diameter, b) welding time adjustment with respect to current selected to achieve acceptable nugget sizes [11].

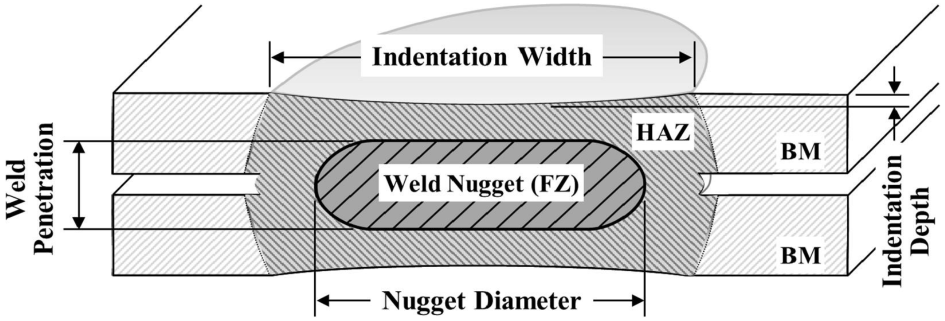

Figure 2.4. Weld Nugget structure of resistance spot welding [13]

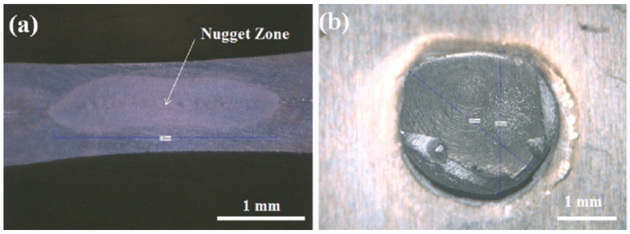

Figure 2.5. Resistance spot welded nugget shown from a) the side b) from the top [14]

Plate thickness: Thicker sheets require higher currents and larger electrodes, compared to thin sheets, to reach an adequate nugget size, as it strongly affects heat dissipation [10].

Surface conditions: Weldability is especially affected by coatings for corrosion resistance, and requires adjustments in the welding setup/parameters to achieve optimal weld quality [10].

Dissimilar material: When welding dissimilar metals, the resistivities might differ which effects the location where heat is generated. This will eventually shift the position of the weld nugget away from the sheets interface. A similar effect is encountered when joining dissimilar plate thicknesses.

Inter-distance between welds: When the resistance spot welds are placed too close to each other, the current could be shunted, as the resistance via the previous weld could be lower than the resistance of the new welding position. It will result in insufficient melting and defect formation.

Stresses: Will be introduced during the welding process due to thermal gradients, thermal expansion and contraction, and plastic deformation[10]. The final residual stress is expected to increase in the nugget in case of thicker plates [10].

As a result of the welding process a weld is produced, schematically shown in Figure2.4 and Figure2.5, combined with a cross-sectional and top view of an actual weld:

2.2. Twinning Induced Plasticity Steel (TWIP)

Twinning induced plasticity steel (TWIP) belong to the class of 2nd generation Advanced High Strength Steels (AHSS). TWIP Steels retain a mainly austenitic phase at room temperature due to the high manganese content (17-24%), which suppresses the phase transformation during cooling. Their primary deformation mechanisms are twinning within the grains and refining the microstructure, which lead to high instantaneous hardening [15]. TWIP steels offer an exceptional combination of strength and formability. Their hardening rate rises to 0.4 at 30% engineering strain, remaining constant until 50% total elongation, with tensile strengths often exceeding 1000 MPa [15]. In Figure2.6 the high-manganese austenitic steel is indicated by the dark-grey envelop towards the right-top corner, indicating the excellent formability and high strength of these steels.

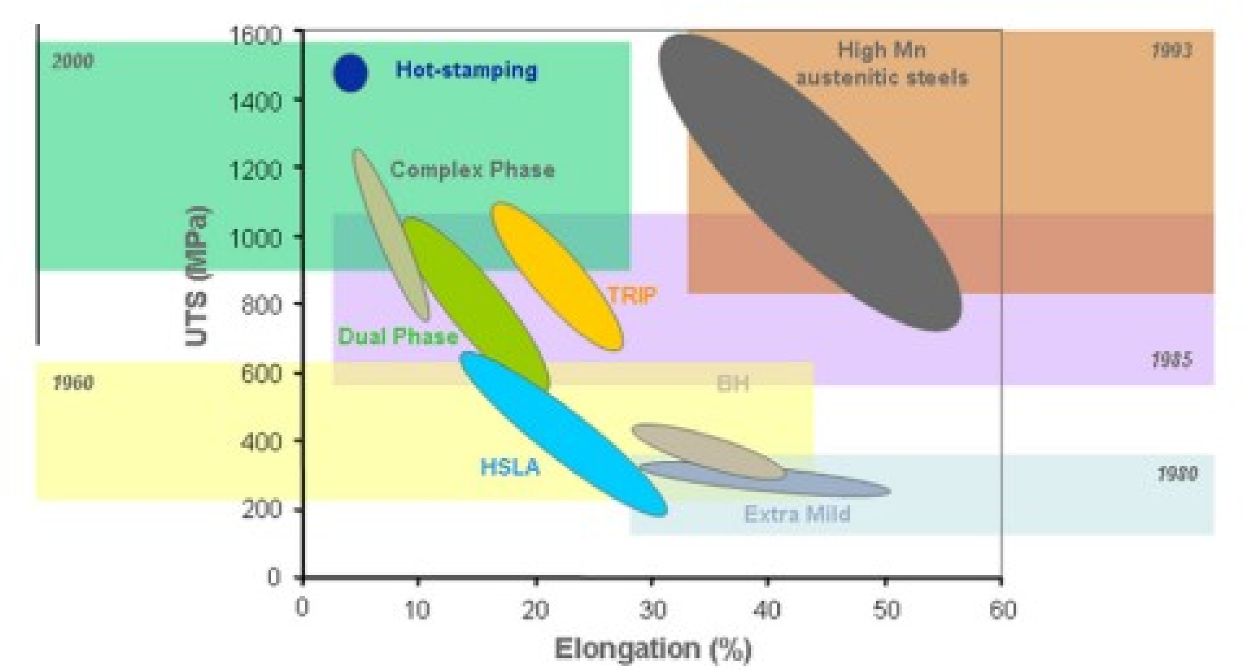

Figure 2.6. Elongation in function of the ultimate tensile strength for usual steels used in the automotive industry [16]

2.2.1. Plasticity Mechanisms and Texture of TWIP Steels

TWIP steels exhibit superior cold formability (over 40%) compared to ferritic steels. Beyond the dislocation glide, mechanical twinning and ϵ-martensite formation are key deformation modes, both involving nanometer-thick, plate-like structures with similar nucleation mechanisms. [16]

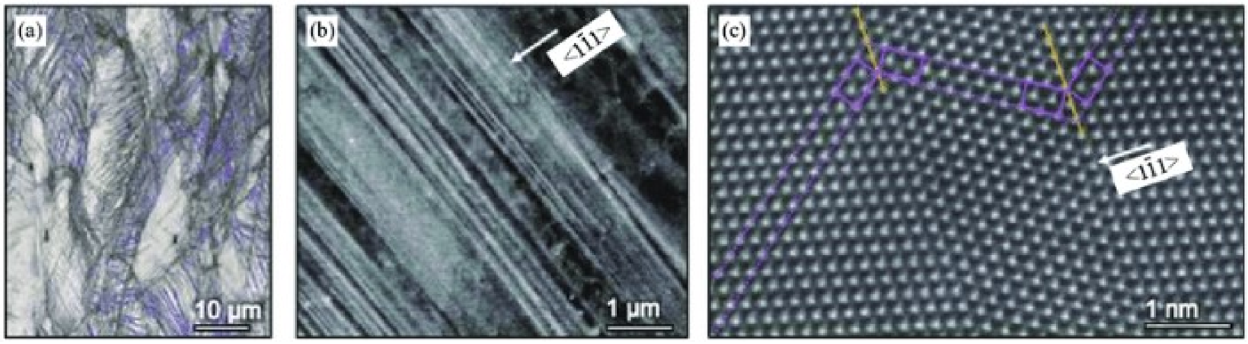

Figure 2.7. Structure of TWIP steel after deformation at room temperature at different magnifications [17]

Mechanical twinning in low-stacking-fault energy (SFE) face-centred cubic (fcc) alloys results from the coordinated glide of intrinsic Shockley partial dislocations on parallel {111} planes (twinning habit plane). This causes crystallographic reorientation while maintaining the fcc lattice. Figure 2.7 and Figure 2.8 show these deformations. This process relocates the carbon atoms from the octahedral to the tetrahedral sites within the twin region, which significantly contributes to the hardening and enhanced-worked hardening. [16].

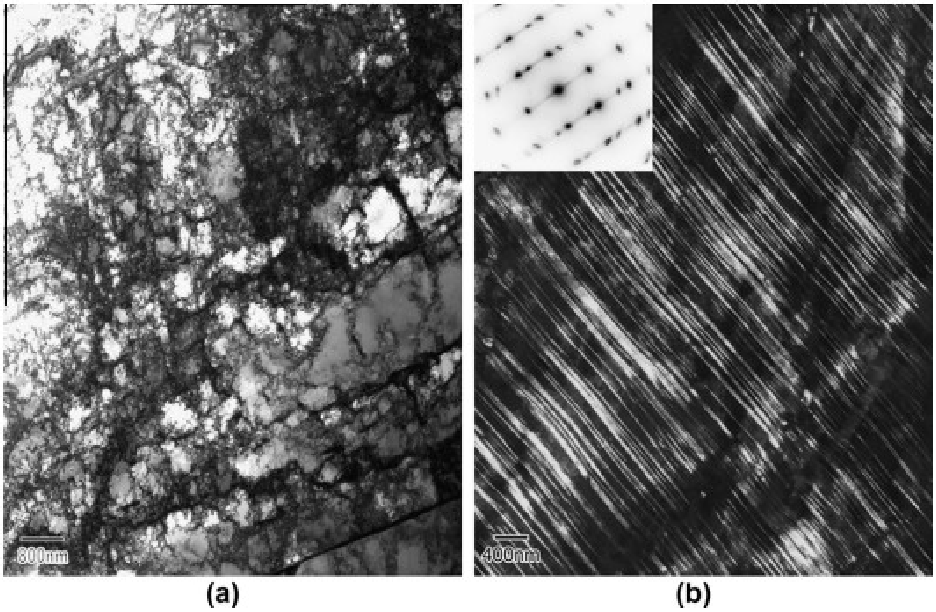

Figure 2.8. Twinning-Induced Plasticity Steels (TWIP) structure showcasing (a) "dislocation cell-like structure" after 20% deformation and (b) mechanical twinning across the structure after 50% strain [16]

E-martensite formation resembles twinning closely, occurring via dislocation glide on every second {111} plane, or equivalently by the glide of the extrinsic Shockley partial dislocations on successive parallel {111} planes. Twinning and E-martensite formation occurs within the same shear bands usually. The SFE strongly influences both mechanisms, as recent studies indicate that there is a linear relationship between the SFE and the final morphology and thickness of mechanical twins [16].

High manganese austenitic TWIP steels possess a fine-grained structure due to rapid recrystallization kinetics and oriented nucleation. This leads to a weak initial texture despite the minor elastic and plastic anisotropy. The texture evolves distinctly with tensile direction, with specific fibres reinforcing the texture along he tensile axis, promoting the twinning kinetics. Consequently, straining in the rolling direction yields a higher twin volume fraction and increased work hardening. Conversely, the material exhibits superior tensile strength and total elongation in the transverse direction [16]. Figure2.8 illustrates TWIP steel microstructure evolution upon varying levels of deformation [16].

2.2.2. Mechanisms for mechanical property improvement

TWIP steels owe their exceptional strain-hardening primarily to deformation twins. Both modelling and experimental evidence confirm that twinning significantly enhances work-hardening compared to dislocation glide alone. For instance, Fe-30Mn alloys, which deform only by dislocation glide, exhibit lower work-hardening, underscoring the impact of twinning. Even carbon-free alloys show substantial strain-hardening due to twinning [16]. Kim et al. [18] further explain twinning's dominant role, limiting dislocation-dislocation interactions (DSA) to less than 3% of total flow stress [18].

Yield strength in TWIP steels can be improved through several methods. While grain refinement is beneficial, its application is limited by processing constraints. Pre-straining significantly increases yield strength but at the cost of reduced ductility and induced anisotropy. However, subsequent recovery treatments can partially restore ductility without compromising yield strength by stabilizing deformation twins [16]. Precipitation strengthening, particularly with vanadium (V) additions, offers substantial yield strength increases while maintaining reasonable ductility. The interaction between precipitation and deformation twinning, especially at higher strains, warrants further investigation [16].

2.2.3. Formability of the steel grade

TWIP steel grades exhibit excellent formability, often surpassing other AHSS grades due to their outstanding balance of strength and elongation. Numerical simulations of yield strength functions effectively describe this characteristic. TWIP steels can be formed into complex shapes with less effort and energy than other high-strength steels, sometimes even easier than mild steel grades [16].

However, a challenge in forming TWIP steels is the occurrence of slant fracture, a premature shear fracture in the thickness direction, not fully explained by traditional necking. The Maximum Shear Stress (MSS) criterion effectively describes TWIP steel fracture behaviour by relating fracture strain to maximum shear stress. The roles of twinning, dynamic strain ageing, and strain rate activity in this phenomenon are crucial and require further investigation [16].

2.3. Liquid Metal Embrittlement (LME)

The resistance of metals to degradation to molten metal is a critical industrial concern. Early investigations into Liquid Metal Embrittlement (LME) stemmed from soldering and brazing, where specific alloys failed when exposed to lead-tin solders, while other steel alloys failed with copper-based brazing [19]. LME is characterized by brittle fracture occurring at stresses below the material's yield strength in an unwetted state [20]. Nuclear power research significantly advanced LME studies, focusing on liquid metal coolants and reactor materials. While LME was historically defined as ductility loss in a solid metal due to liquid metal presence, the diversity of observed behaviours necessitates a more nuanced classification system [19].

Initially, chemical specificity of LME was considered to be binary, occurring only at the melting point of

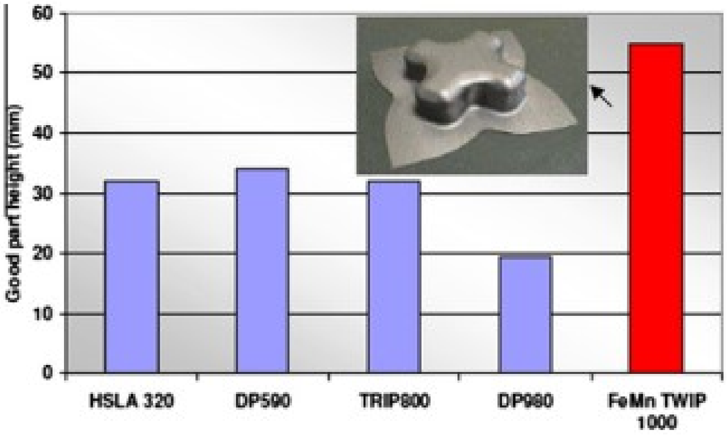

Figure 2.9. Maximum height of different High Strength Steel grades before failure during stamping [16]

one liquid component, with the severity of the phenomenon decreasing at higher temperatures. However, subsequent research revealed a more complex phenomenon. A wider range of systems exhibit embrittlement under previously unconsidered conditions, highlighting the importance of experimental parameters for definitive LME predictions [19].

Reviews often present misleading tables that suggest a narrower LME scope than found in practice. Previously reported non-embrittlement cases were based on limited testing, while extensive investigations later revealed LME in previously unstudied systems [19]. The binary view of LME has been superseded by the recognition of a spectrum of susceptibility. The concept now describes the inherent susceptibility of specific liquid-solid metal pairs, determined by their chemistry. This intrinsic chemical susceptibility is modulated by microstructural, environmental, and mechanical factors that dictate whether ductile or brittle behaviour occurs. Successful predictive methods must integrate both intrinsic chemical susceptibility and extrinsic influencing factors [19].

2.3.1. Factors affecting LME

LME exhibits complex, often contradictory behaviour, making prediction and mitigation difficult [19]. Various factors influence this, including exposure time, temperature, microstructure, prior plastic deformation, compositional effects, and sample stress state. These factors can lead to phenomena, like bond weakening at the crack tip or enhanced local plasticity [20]:

Temperature: Temperature dependence of LME varies, showing either increased embrittlement or "ductility trough" at higher temperatures [19] [22]. Wetting transition complicates this behaviour too [23]. Figure 2.10 shows the effect of temperature.

Exposure time: Exposure time is also a crucial factor, especially for the grain boundary penetration process, as liquid metal infiltration requires sufficient time [19]. However, some systems show minimal sensitivity, suggesting other possible mechanisms [24].

Strain and stress rate: Significantly impacts LME, as higher rates can increase the embrittlement due to rapid surface exposure, while slower rates increase susceptibility when incubation times are significant [19].

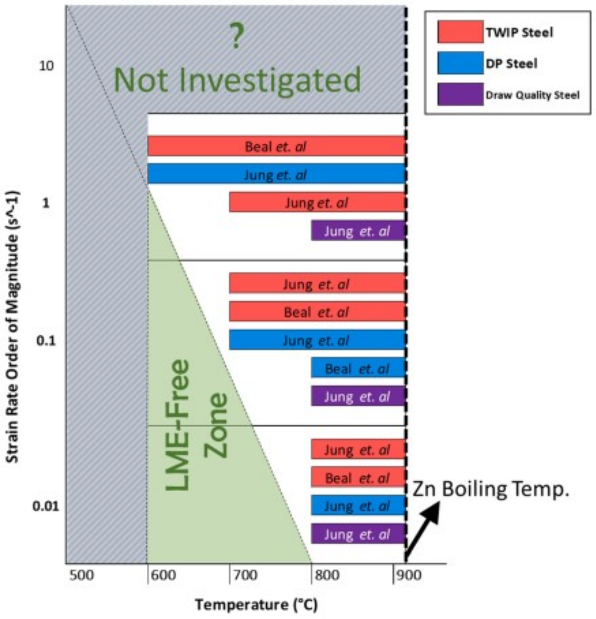

Figure 2.10. Connection between temperature and strain rate for LME cracking in different researched systems showcasing different LME models [21]

Figure 2.10 shows the effect of strain rate. Stress-assisted grain boundary diffusion is vital for theories like the later mentioned Gordon-An scenario [21] [25].

Grain size: Grain size also impacts LME, with coarser grains generally increasing embrittlement, even though exceptions exist [19] [26]. Triaxial stresses from pre-cracks or notches increase embrittlement in a major way, even in systems with minimal LME under uniaxial loading [19].

Increased dissolution: In systems like bismuth-copper, triaxial stresses increase grain coarsening, promoting liquid metal penetration depth.

Enhanced stress-assisted penetration: Tensile stresses strain grain boundaries, facilitating liquid metal infiltration. Triaxial stresses magnify this, leading to more rapid penetration.

Induced notch sensitivity: Liquid metals can induce notch sensitivity even in materials normally not susceptible. This occurs when liquid metal reduces local cleavage strength at the crack tip, increasing susceptibility to brittle fracture.

Prior plastic deformation: Priot plastic deformation generally exacerbates the LME process, especially when plasticity and brittle fracture are both present and complete [19]. This relationship is a system-dependent and complex, as deformation can also enhance penetration of the grain boundary and increase corrosion susceptibility [19].

Material composition: The composition of both solid and liquid metals significantly influences LME. Solid metal impurities, such as ow melting-point inclusions can enhance embrittlement, while some impurities can mitigate it by segregating to the grain boundaries [19]. Liquid metal alloys dissolved from the solid phase can profoundly affect embrittlement. Examples include materials such as aluminium [27], manganese [28], silicon [29] and phosphorus [30] in steel. Dissolved gases such as dissolved oxygen and in a lead-bismuth eutectic can both mitigate or enhance embrittlement. It mainly depends on the formation of surface oxides [19]. Chemical reactions and dissolution between solid and liquid metals, potentially forming intermetallic phases, significantly influence LME susceptibility [19].

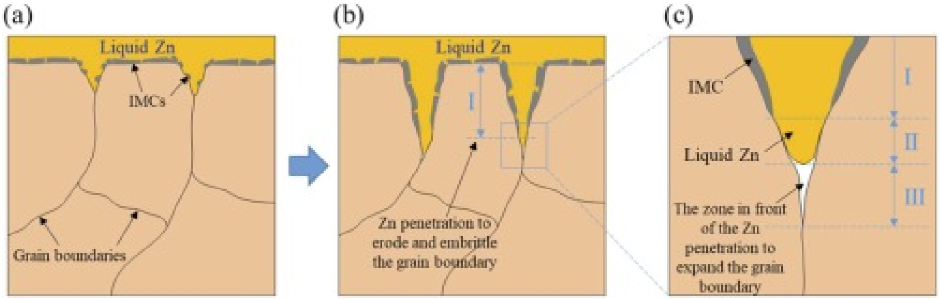

Figure 2.11. LME propagation in the case of liquid Zinc and High-Strength Steel RSW-welds [31]

2.3.2. Mechanism

Despite decades of research, comprehensive LME understanding remains elusive. Proposed explanatory mechanisms generally fall into three categories: grain boundary penetration, corrosion, and interfacial cracking.

Grain boundary penetration: Liquid metal wets and/or penetrates solid metal grain boundaries, leading to decohesion and potential failure, even without applied stress (e.g., gallium-aluminium). Weak intergranular phases can form, further reducing strength [19]. This explains brittle fracture by weakening interatomic bonds [21].

Corrosion-type processes: These involve selective dealloying, dissolved gas influence, or intermetallic phase formation. Similar to aqueous corrosion, factors like flow rate and temperature affect the attack rate. Removing the liquid metal stops the process [19].

Crack initiation at the liquid-solid interface: Occurring intergranularly or transgranularly, similar to stress corrosion cracking. Fracture is instantaneous above critical stress; embrittlement is reversible upon liquid metal removal, and stress is necessary [19].

Several models explaining the mechanism behind LME have been proposed, namely ductile fracture, grain boundary-based, brittle fracture, and dissolution-condensation models, and their mechanisms and properties are discussed below and depicted in Figure 2.12.

2.3.3. Ductile-Fracture Models

Ductile fracture models explain LME through plastic deformation at the crack tip and embrittler atom influence. The Lynch model proposes the adsorption of embrittler atoms which reduces the critical stress, affecting both the nucleation and motion [21]. However, it fails to account for the observed delays in failure [32]. The Hancock-Ives model attributes LME to the dislocation pile-ups at the grain boundaries, which ultimately leads to a localized crack-tip instability. It also facilitates the solid-state diffusion of the embrittler atoms [21]. The Rebinder-Popovich model incorporates the aspects of the Rostoker model, suggesting that the

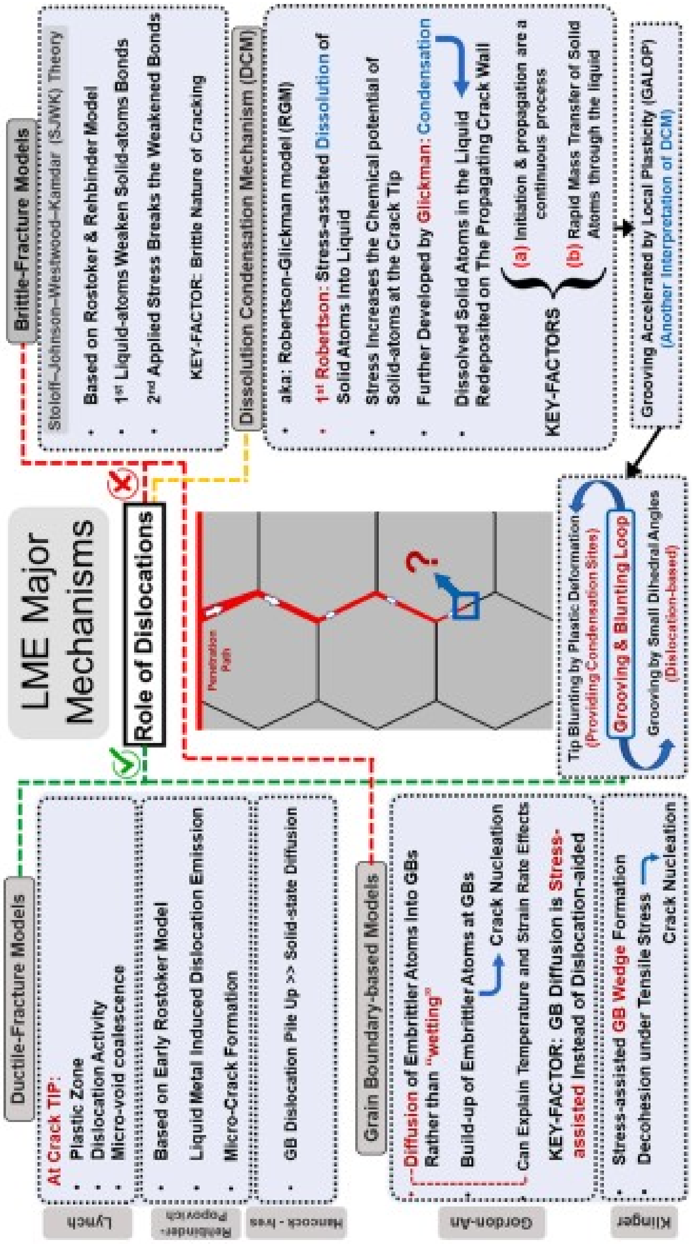

Figure 2.12. Figure showing the various LME mechanisms, describing their individual properties [21]

surface energy modifications enhance the plastic deformation ahead of the crack tip. This increased activity of dislocations promotes microcrack formation due to work-hardening, as microcracks propagate ductility [21].

The advantages of these models are that they explain LME through the plasticity of the crack-tip and by explaining the role of the embrittling atoms. They also highlight the importance of dislocation pile-ups and the impact of surface energy on plastic deformation. On the other hand, disadvantages of these models are that they oversimplify the interactions and neglect the observed delays in failure. They are also not applicable in case of single crystals and are difficult to quantify.

2.3.4. Grain Boundary-based Models

Grain Boundary-based models emphasize the mass transfer of liquid and the stress-assisted grain boundary diffusion during LME. The Gordon-An scenario suggests that the liquid phase mass transfer to the crack tip happens by liquid flow. Krishtal and Gordon-An propose stress-assisted grain boundary diffusion, where the embrittler atoms impede the dislocation slip, hence facilitating crack propagation along the grain boundaries. This then leads to a ductile-to-brittle transition and a higher brittle-to-ductile transition. This model explains LME incubation time through diffusion activation energy [21]. Another model, that of Klinger, describes LME in a similar fashion, where crack nucleation is following the decohesion of grain boundaries under tensile stress. This requires prior diffusion at the boundaries. The liquid metal then advances through these opened boundaries, facilitating a rapid crack propagation by the diffusion and flow of the liquid [25].

The benefit of these models is that they account for liquid mass transfer and describes the atomic decohesion precisely. In addition, they identify the diffusion at the grain boundaries as being stress-assisted and propose that the liquid flow precipitating crack propagation. On the other hand, the main shortcoming are oversimplification, along with having a limited scope and focus only on diffusion.

2.3.5. Brittle-Fracture Models

These models focus on proposing crack nucleation at intersections of dislocation pile-ups and free surfaces, which are stabilized by a liquid metal coating. Rostoker et al. [19] suggest that the crack nuclei grow at intersecting dislocation pile-ups and free surfaces. Their growth is stabilized by liquid metal reducing the surface energy barrier, aligning with the Griffith criterion. This mechanism is reliant on the liquid-solid metal interface having lower energy than the solid-solid interfaces [19]. Stoloff and Johnston emphasize the bond weakening at the crack tip during the adsorption of liquid metal as the main process, but they only partially account for the crack-tip plasticity. Other theories suggest that liquid metal enhances local plasticity. Recent studies propose multi-stage processes, with kinetics influenced by dislocation-based mechanisms and wetting behavior, since corrosion processes (dissolution, oxidation) also significantly influence LME [19].

These models focus on the crack nucleation and connect their findings to the Griffith criterion, which is beneficial, especially so with an emphasis on crack tip behaviour. However, they come short by neglecting crack tip plasticity and offering simplified explanations.

2.3.6. Dissolution-Condensation Mechanism (DCM)

The DCM is also known as the Roberson-Glickman model (RGM). It proposes crack propagation that is driven by the stress-assisted dissolution of solid atoms into the liquid embrittler. The increased chemical potential at the crack tip accelerates the dissolution of solid atoms, with a rapid diffusion transporting the dissolved atoms. For systems such as the Fe-Zn, the DCM has a continuous initiation/propagation concept that contradicts the observed stages [19]. Glicman integrates condensation micromechanism into this model, which involves the redeposition of dissolved atoms on to the propagating crack wall. As such, DCM can be considered a non-electrochemical, environmentally assisted cracking: a type of stress-corrosion cracking [21].

This model evolved into the grooving accelerated by local plasticity model known as GALOP, which builds on the Mullins grain boundary grooving theory. It proposes that the tensile stress is concentrated at the groove tips, leading to a localized plastic deformation, blunting of the crack-tips and surface redeposition. The model assumes a continuous grooving cycle, which requires sufficient grooving rate to overcome the blunting of the crack-tip. While LME is predominantly intergranular, its transgranular form has been reported, consistent with brittle fracture theories (E.g., RGM[21]).

These models explain crack propagation caused by stress-assisted solid-state diffusion, as well as account for rapid diffusion, linking the process to stress-corrosion cracking. GALOP expands the Mullins grooving theory and explains the grooving-blunting cycle. The shortcomings, however, are that DCM contradicts previous multi-stage observations, while also lacking direct evidence due to working with oversimplifies models. As opposed, GALOP provides a complex theory.

2.3.7. LME in Fe-Zn System

The dislocation-dependent crack nucleation is challenged by the absence of dislocations near the LME crack in Fe-Zn systems. Research suggests the brittle grain boundary opening along with liquid penetration, or solid-state grain boundary diffusion of the embrittler atoms [21]. The exact transport mechanism of these atoms along the boundaries is unclear, as liquid Zn was not found at the crack tip. Instead, Fe-Mn phases and Fe-Mn-Zn peritectic reactions occurred which indicate a solid-state diffusion [21]. Disagreements arise from examining post-formation cracks, requiring further studies focusing on the period during formation for definitive conclusions [25].

The DCM/RGM model is not applicable in case of Fe-Zn systems's liquid phase, due to the cracks being filled with Fe-Mn saturated alloy [21]. The liquid Zn presence however confirms the that LME brittle crack propagation and grain boundary diffusion. The stress assisted grain boundary diffusion model explains the penetration of the high-temperature liquid metal. For near room temperature systems, further research is required. Stress is a consistent prerequisite, with stress-assisted grain boundary diffusion vital for diffusion-based theories [25]. The Gordon-An scenario proposes a stress-enhanced diffusion zone ahead of the crack tip [21, 25]. Klinger and Rabkin expanded this model for multi-component systems, making it applicable to LME [25].

2.3.8. Experimental method for Fe-Zn system

Thermomechanical testing, often using a Gleeble machine, studies LME at elevated temperatures and stress levels. Zinc-coated TRIP steel is highly susceptible to LME. DaGiovanni et al. [25] investigated stress effects at 600 °C using unloaded, elastic (190 MPa, 305 MPa), and beyond-elastic (420 MPa) conditions.

Stress being significantly enhanced by Zn diffusion is shown by the experiments, as a specific temperature and a minimum stress were needed to initiate the diffusion and penetration of Zn. No stress was needed for a minimal Zn penetration, but via grain boundary and bulk diffusion, stress significantly increased the concentration of Zn. A substrate separation with liquid zinc penetration into grain boundaries was observed in the highest stress case. Increased stress led to LME crack formation and liquid Zn penetrating grain boundaries, forming a new diffusion zone ahead of the crack tip. This aligns with Razmpoosh's theory for LME microevent mechanisms and the Gordon-An grain boundary model [25].

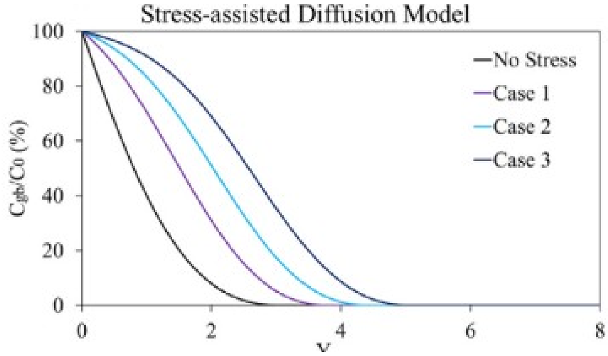

Figure 2.13. Diffusion depth profiles for all cases [25]

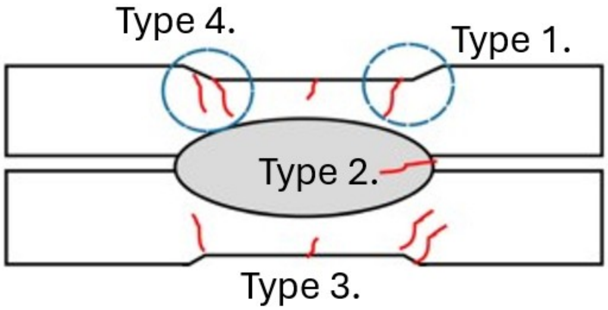

Figure 2.14. Usual LME assisted cracking spots after RSW [34]

2.3.9. Predicting LME

While the influence of testing and metallurgical parameters on LME is well understood, predicting which liquid metal will embrittle specific solid metals remains a challenge [20]. Approaches correlate chemical interactions with LME propensity. Empirical correlations, such as LME susceptibility and electronegativity differences between solid and liquid metals, support the critical role of weakened interatomic bonds. Theoretical models generally predict bond strength.

A direct link between chemical interaction and embrittlement can be established via interfacial energies and thermodynamic properties. Low positive heats of mixing correlate with low interfacial energies, suggesting higher LME propensity, while high positive values indicate weak or absent embrittlement; and negative values suggest strong chemical reaction. Such models successfully predict embrittling behaviour for several liquid metals, such as zinc and cadmium on aluminium, and align with experimental observations of LME in ferrous alloys by various liquid metals [20].

2.3.10. Principal observations of LME

LME is characterized by exceptionally high crack propagation rates, typically centimetres to meters per second [32].

A significant decrease in strain to rupture is observed within a specific temperature range, the so-called ductility trough. Below the solid metal's yield strength, the liquid metal has no discernible influence on mechanical properties and intermetallic compound formation prevents embrittlement. LME requires intimate "wetting" contact between solid and liquid metals. Oxide films or intervening layers, or liquid metal removal after initial contact, inhibit the phenomenon. While solid metal composition generally has limited LME effect, liquid metal composition changes can significantly increase or decrease embrittlement. LME is exacerbated by larger grain sizes, which also elevate the brittle-to-ductile transition temperature.

2.4. Liquid Metal Embrittlement for Spot Welded High-Strength Steels

RSW of AHSS is complicated by a narrower process window when compared to mild steels, brittle weld nuggets, softening of the heat affected zone (HAZ) and compromised mechanical properties. The zinc coatings that serve as corrosion protection of these grades, further complicate the welding process by promoting LME cracking [33].

Studies on LME cracking in AHSS during RSW reveal cracks typically appear on the weld surface in four forms, also shown in Figure 2.14: Type 1 as periphery cracks; Type 2 as cracks extending into the nugget, Type 3 as short nugget cracks; or Type 4 as cracks originating from faying sheet notches [34].

These cracks are often intergranular, linked to the penetration of zinc into the microstructure. Some studies report only zinc, while others also copper enrichment, suggesting the degradation of electrodes and Zn-Cu intermetallic phases as a result. The electrode indentation region is most vulnerable to LME, primarily yielding Type 1 cracks [34].

2.4.1. Factors Influencing LME

LME depends on a series of factors, often with opposing effects. Which of these factors prevails is often an empirical question. This section reviews the main drivers of LME.

Zinc availability The availability of zinc is critical. Molten zinc is usually pushed to the weldment periphery, correlating with Type 1 crack prevalence. Zinc build up at sheet notches can cause Type 4 cracking, though in itself it is insufficient for LME [34]

Effect of temperature Temperature also plays a crucial role, as for zinc-coated steels LME typically occurs between 700-900 °C, well above the melting point of zinc at 427°C. This is most likely due to kinetic limitations and the dissolution of the Fe-Zn intermetallic around 782°C. Above 900°C, liquid zinc evaporates, preventing LME formation [34]. Periphery weldment temperatures often fall within the sensitive range, explaining higher incidence of Type 1 cracks, often exceeding 1000 micrometers [35].

Effect of stress Stress, particularly from the plastic deformation drives LME. Hot tensile tests show that LME assisted failure occurs above the yield strength of the steel grades tested. While during welding (especially in squeeze cycles), compressive stress dominates, tensile stress emerges during hold time and cooling, which potentially promotes crack formation. Misaligned electrodes or an increased heat input can exacerbate LME by increasing the tensile stresses present. Optimizing the welding parameters, such as increasing the electrode force or hold time, can all mitigate LME by prolonging the compressive stress present, thereby aiding cooling [34]. Stronger steel grades exhibit increased LME sensitivity due to higher stress development. Ling et al. found galvanized Q&P980 steel more susceptible than low-carbon steel, especially in dissimilar joints and with multi-pulse welding, due to its lower reactivity with liquid zinc, higher achievable stress, and greater proportion of susceptible grain boundaries [36].

Effect of Microstructure Microstructure significantly influences LME susceptibility in AHSS. TWIP steels, with high austenite fractions, show high LME susceptibility, though a direct correlation with austenite content is debated. DiGiovanni's work on martensitic, austenitic, and ferritic-pearlitic steels exposed to various liquid metals revealed a common intergranular and interlath cracking mechanism, underscoring the role of grain boundary decohesion. Ab initio calculations show that zinc, silicon, and aluminium exhibit negative segregation energy to grain boundaries [37]. Zinc drastically reduces grain boundary cohesion, while silicon slightly enhances it.Auger et al. [38] highlighted that grain boundary plane orientation, particularly high-index planes, strongly influences zinc penetration and LME crack propagation [39]. According to Ikeda et al. [40], LME prefers to follow high-angle grain boundaries when when progressing in the microstructure. Akbari et al. [41] state the same, with the addition that this is possible due to the high angle grain boundaries having a high-enough level of energy for the wetting transition condition to be met.

Effect of Coating Type Coating type also impacts LME: Hot-dip galvanized (GI) coatings increase LME susceptibility compared to galvannealed (GA), or electro-galvanized (EG) coatings, likely due to lower melting point of GI, which makes more liquid zinc available [34].

2.4.2. Experimental Procedure and Results

Resistance spot welding (RSW) of 1.2 mm thick medium manganese steel, coated with 8.0 µm galvanneal zinc, was investigated to understand and mitigate LME cracking. The steel exhibited an ultimate tensile

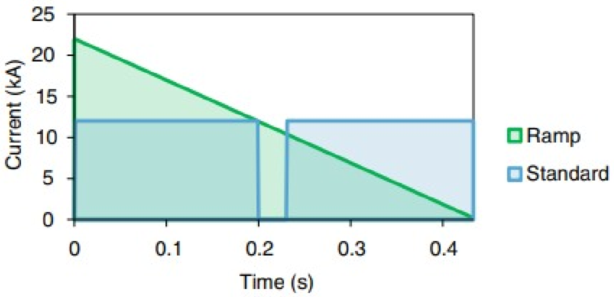

Figure 2.15. Different current schemes for the ramp down method and the standard method [42]

strength of 780 MPa with yield strength of 370 MPa and 16% elongation. Two 2.0 mm thick galvanized mild steel sheets served as counter material. A servo C-type welding gun with a direct current source and dome-shaped Cu-Cr electrodes (16.0 mm body, 6.0 mm tip face, 50.0 mm face radius) were used. Electrodes and sheets were cleaned with acetone. Welding parameters followed ISO 18278-1 (2004), with varied welding time to modulate heat input [33].

LME cracks were detected using several techniques. Initial visual inspection and photographic documentation were performed with a stereo microscope. Zinc coating was removed with 20% HCl to confirm cracks, followed by fluorescent magnetic particle testing. For microstructural analysis, cross-sections were prepared, and EBSD and EDS were used to analyse crack tips and confirm zinc presence, indicating LME [33].

In-situ crack monitoring utilized high-speed camera imaging with a half-cross-sectioned welding setup. A reduced welding current (60%) and time (333 ms) were used, along with a frame rate of 4000 fps, a 5 mm lens, and ultraviolet filters. This allowed observation of crack initiation, propagation, and termination [33].

Finite element simulations (FEM) with SORPAS software analysed temperature and stress distributions. Mechanical, metallurgical, electrical, and thermal models were incorporated, with material properties from the SORPAS database. Contact resistance was calculated using a standard equation, and high mesh density (5000 elements) was applied at the electrode-sheet interface. Simulations were performed with a welding time of 667 ms [33].

Analysis of LME crack morphology reveals distinct regions: initial contact cracks, transient contact cracks, and non-contact cracks. The study focuses on transient and non-contact crack locations. Non-contact cracks were first observed after 167 ms of welding time, exhibiting circumferential growth with increased welding time. A critical welding time of 250 ms was identified for the initial observation of non-contact cracks [33].

Cross-sectional SEM micrographs confirm LME cracks in the non-contact region. EBSD analysis shows intergranular crack growth, while EDS confirms zinc presence at crack tips. High-speed camera images with the half-electrode setup provide further insights into crack initiation and propagation, showing that cracks in the non-contact region are influenced by electrode contact and nugget behaviour [33].

FEM simulations reveal instantaneous temperature drops (ITD) around the electrode-sheet interface, coinciding with electrode indentation. These ITDs are associated with tensile stress development, likely from contact with water-cooled electrodes. Tensile stress and thermal gradient magnitudes increase with welding time [33].

The contact diameter evolution of the weld nugget shows a critical relationship with LME occurrence, predominantly when the nugget diameter to electrode contact diameter ratio exceeds 1.0. A critical welding time was identified when the weld nugget diameter surpassed both contact and electrode radius diameters. The electrode tip face diameter is also a key parameter governing thermal gradient and tensile stress magnitudes [33]. Experimental observations confirm the correlation between welding time exceeding critical time and LME cracking, suggesting critical welding time as a predictor for LME onset. Prior to this time, the thermal gradient was insufficient to induce LME-causing tensile stresses. Rapid nugget diameter growth relative to contact diameter lead to LME crack formation above this critical time [33].

Additionally, Gleeble simulations help investigate the influence of temperature and strain rate on embrittlement. Tests between 600-1000°C with strain rates from 1.3×10^{-3} to $1.3\ \text{s}^{-1}$ showed that embrittlement occurred within a specific temperature range dependent on strain rate. Higher strain rates widened this range and lowered the embrittlement onset temperature. A critical stress for crack initiation was inversely related to temperature. Holding samples at testing temperature before loading mitigated embrittlement, likely due to the formation of FeMnZn intermetallic compounds that consume liquid zinc, impeding penetration [43].

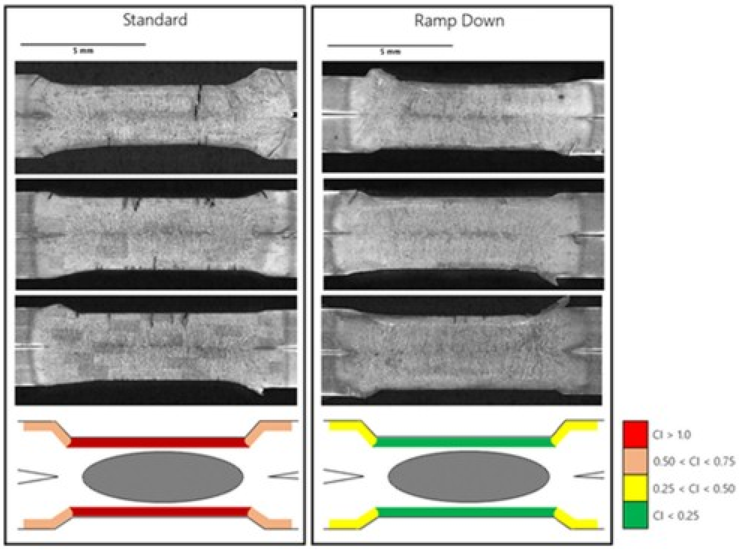

Figure 2.16. Difference in results of the standard current and ramp down current schemes during RSW, shown in photographic images and models indicating the cracking index along the welds[42]

2.4.3. Possible Mitigation Methods

Finding appropriate welding conditions is a possible method for mitigating LME in RSW of advanced high strength steels [42]. A novel ramp-down current profile is investigated to mitigate LME cracking in TRIP1100 AHSS. This method aims to control the thermal history of the weld. Experimental welds from the ramped current strategy are compared to standard constant current welds using crack depth, number, and index to quantify LME. Standard current welds show significant LME [42].

FEA models temperature distributions and reveals high tensile stresses during cooling and electrode release. The ramp-down current method reduces peak temperatures and mitigates tensile stress spikes, as shown in Figures 2.15 and 2.16. Experimental results shows reduced LME cracking with the ramp-down method, explained by minimized time in the LME-active region [42].

A similar study by Bouaziz et al. focuses on mitigating LME during RSW of TWIP steels [44]. LME significantly reduces the weldable current range. An innovative 2-pulse welding technique is proposed: the first pulse forms a strong corona bond with a minimum nugget size, and the second increases nugget size without expulsion or inducing LME. This approach broadened the welding current range by approximately 85.7% and achieved LME-free welds. This is possible as the method controls heat input and minimizes tensile stress in susceptible regions, as confirmed by simulations [44].

2.5. Research questions

Despite extensive research characterizing LME in RSW of TWIP steels concerning various welding parameters, like current and time, a significant gap exists in understanding the direct effect of holding time. During usage in the automotive industry, high temperature, high strain rate, high stresses and a short exposure time to zinc are all present, making TWIP steels especially prone to LME during production of vehicles [6]. Comprehensive studies specifically addressing the influence of this crucial parameter on LME susceptibility and crack formation in TWIP steels remain limited. From this gap of the relevant literature, the main research questions for this thesis are the following:

Are there any variations in LME crack morphology as a function of holding time in TWIP steels?

What is the direct correlation between holding time and the presence of LME in TWIP steels during RSW?

How does holding time influence the localized availability of zinc, and subsequently, its contribution to LME formation?

To what extent does holding time modulate the generation and distribution of residual stresses within RSW of TWIP steels?

Are there any connections between the hold time and the microstructure present in the weld nugget and the heat affected zone? If yes, how does it affect LME susceptibility of the material?

3. Materials, Processing, Characterisation Methodology

This chapter discusses the base material used for the study, along the preparation and testing methods in detail.

3.1. Base material and weldments

A TWIP steel with the thickness of 1.23 mm is used. This steel has a predominantly austenitic microstructure. Tables 3.1 and 3.2 show the chemical composition of the most important alloying elements and that of the zinc coating, respectively. Table 3.3 lists the main mechanical properties of the steel grade.

Table 3.1. Chemical composition of the TWIP grade

Alloying Element	Mn	Al	C	Ni	Ti	N	Si
Content [w%]	17.39	14.90	6.10	3.60	1.09	0.90	0.80

Table 3.2. Chemical composition of the zinc coating

Alloying Element	Zn	Al
Content [w%]	99.8	0.2

Table 3.3. Mechanical properties of the TWIP grade

Property	Rp [MPa]	Rm [MPa]	Ag [%]	A80 [%]
Value	435	900	54.0	-

The steel is a high-manganese content (17.39%) TWIP grade, which also contains nearly 15% aluminium. The zinc coating contains 0.2% aluminium as well. The steel has an outstanding combination of strength and formability.

3.1.1. Welding

Two different welding configurations are induced to introduce LME. In the first setup, two sheets of the TWIP steel were spot welded. Each batch of samples starts with a shunt weld, which is a method used in RSW to establish the initial connection between the sheets prior to the main welds. Subsequently, eight individual welds are produced, constituting the eight samples per batch. In the second setup, TWIP steel was welded with two DX54 deep-drawing steel sheets. This setup allows for the use of welding parameters conducive to LME formation, specifically higher currents and extended welding times, due to the increased thickness of the sample. With this configuration, two batches of welds were produced, each including a shunt weld and eight samples. The batch layout is illustrated in Figure 3.1.

Table3.4 contains the welding parameters used for all three batches. The welding current, force and time were kept constant in this study. The holding time is increased from 5 ms to 355 ms with time intervals of 50 ms. The welding was performed with an ISO5821 F1-16-20-6 CuCr1Zr electrode, using a 1000 MHz MFDC spot welding machine.

For subsequent discussion, samples will be designated by the nomenclature ’HT-number’, where ’number’ represents the duration of the hold time in milliseconds. For instance, a sample subjected to a 55 ms hold time will be referred to as ’HT-55’.

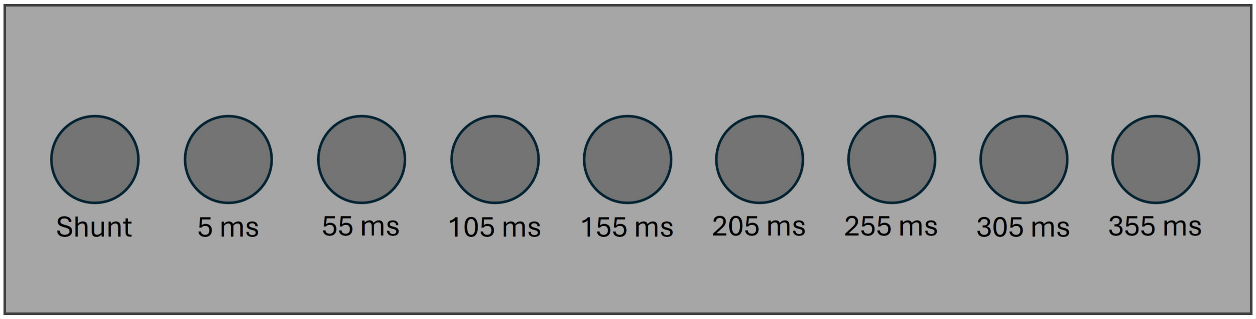

Figure 3.1. Welded sample layout with hold-times indicated in each case

Table 3.4. Welding parameters used in the study

Parameter	Value
Welding current (kA)	7.4
Welding force (kN)	4.5
Welding time (ms)	980
Holding time (ms)	5; 55; 105; 155; 205; 255; 305; 355

3.2. Sample preparation

Samples were cut from the base material and embedded in conductive resin for microstructural evaluation. Metallographic standard preparation procedures were followed, consisting of sand grinding to P4000 and polishing with 3 and 1 μm diamond paste. Samples were cleaned between these steps in an ultrasonic bath.

The preparation of the welded samples followed a similar procedure. The method of weld preparation depends on the presence and location of cracks. Initial identification of cracks is performed using an optical microscope. If no cracks are detected, the weld is sectioned along its middle plane. Conversely, if cracks are observed, the sectioning plane is oriented perpendicular to the crack, as depicted in Figure 3.2. This protocol yields two samples from each weld, both of which were subjected to evaluation.

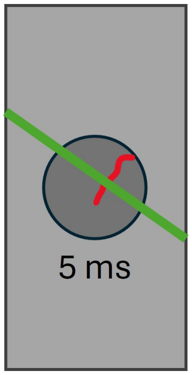

Figure 3.2. Cutting method shown in a sample with a crack

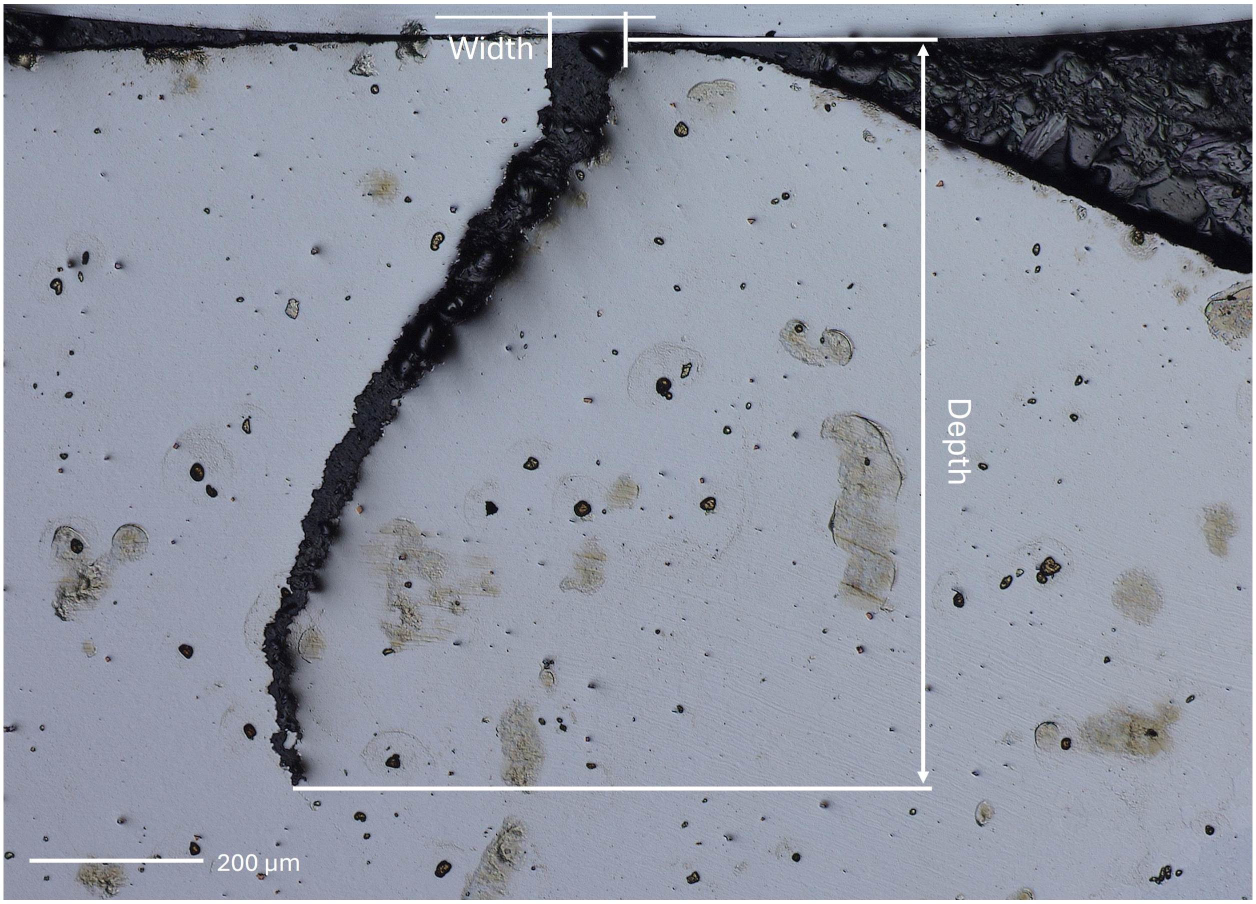

Figure 3.3. Measured crack dimensions

3.3. Etching

Following sectioning, samples underwent an etching procedure to reveal their microstructure. Initial investigations determined that Nital is the most suitable etchant for TWIP steel. A 5% solution is utilized, with an etching time of approximately 40 seconds. The etching step was substituted by the application of OPS liquid for 40 minutes at the final stage of the polishing sequence. This modification was adopted because OPS treatment yielded a clearer and more discernible grain structure, while simultaneously reducing the risk of sample damage.

3.4. Characterisation of the Samples

The processed samples are studied by optical microscopy (OM), Scanning Electron Microscopy (SEM), Energy Dispersive X-ray Spectroscopy (EDS) and the Electron Backscatter Diffraction (EBSD) function of the SEM .

3.4.1. Optical Microscopy

During the OM evaluation, the primary objective was to identify the location of visible cracks and conduct statistical measurements. Crack dimensions are measured, as illustrated in Figure 3.3. Additionally, the distance of each crack from the sample's centre line was measured, and the average distance was calculated. Further statistical analysis involved determining the number of and categorizing these cracks for each sample into two distinct groups: electrode-sample interface cracks and shoulder cracks, as depicted in Figure 3.4. A

Keyence VHX7000N Digital Microscope was used for all optical microscopy observations.

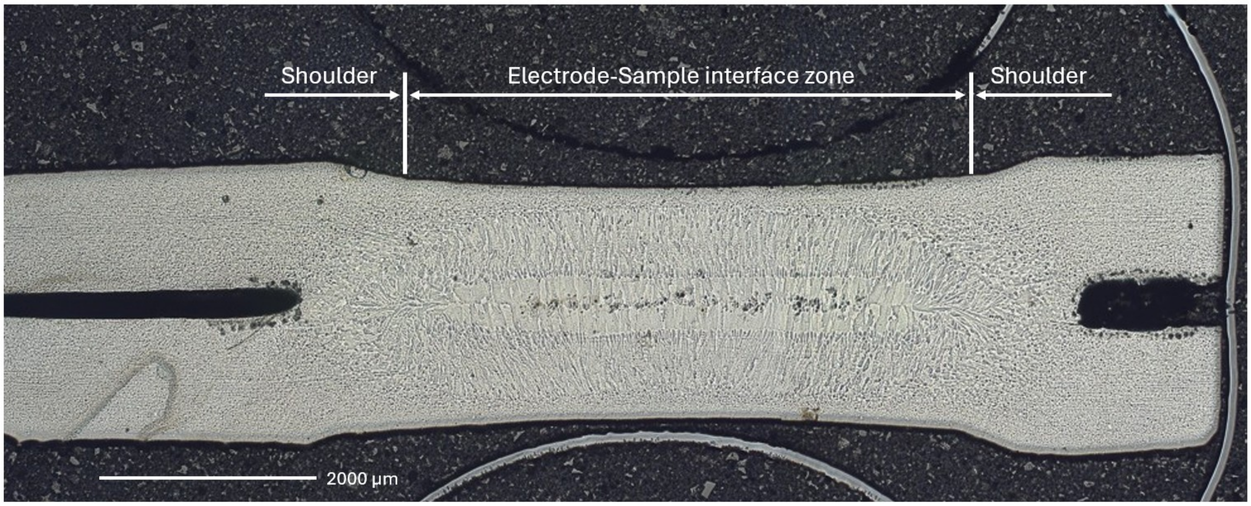

Figure 3.4. The shoulders and the electrode-sample interface zone

3.4.2. Scanning Electron Microscopy

The SEM evaluation served two primary objectives utilizing distinct instruments for specialized tasks. First, a JEOL JSM-IT100 SEM was employed to identify cracks not discernible via optical microscopy. Concurrently, a JEOL JSM-IT800SHL was used to acquire high-magnification images and to conduct EDS and EBSD measurements.

3.4.3. EDS Technique Overview

EDS was employed for two purposes: to characterize the chemical composition of the base material and to confirm the presence of zinc within the observed cracks. The detection of zinc within the crack morphology served as a key indicator for cracks being LME-induced.

3.4.4. EBSD Technique overview

EBSD was utilized to quantify the phase fraction and the grain boundary misorientation distribution, categorized by their angles. Additionally, EBSD provides crucial information to determine whether the observed cracks exhibit an intergranular or transgranular propagation path. The EBSD data were evaluated with EDAX OIM Analysis 8 software, where the following data cleaning steps were taken for each dataset: Grain dilatation, CI (confidence index) Standardization, Neighbour CI correlation and Single Average orientation / grain. These steps are repeated when the resulting maps' indexation is insufficient.

4. Results

4.1. Base material overview

This section presents an evaluation of the base material microstructure using Optical Microscopy, SEM, EDS and EBSD. The base material microstructure is depicted in Figure 4.1. While the rolling direction is distinctly visible in this figure, the underlying microstructure is largely unclear, even after etching. Due to this, further evaluation with EBSD is required.

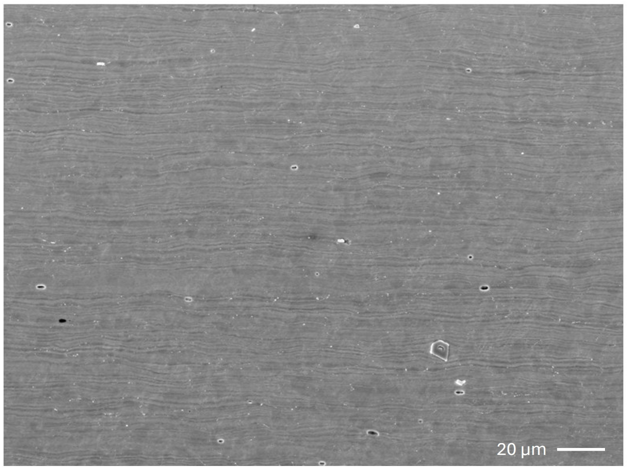

Figure 4.1. SEM picture of the structure of the base material.

The interface between the TWIP steel substrate and the zinc coating is seen in Figures 4.2(a) and 4.2(b) at 150x and 1000x magnification, respectively. The zinc coating on the steel has a thickness of approximately 30 μm. Voids seem to be present in the coating microstructure.

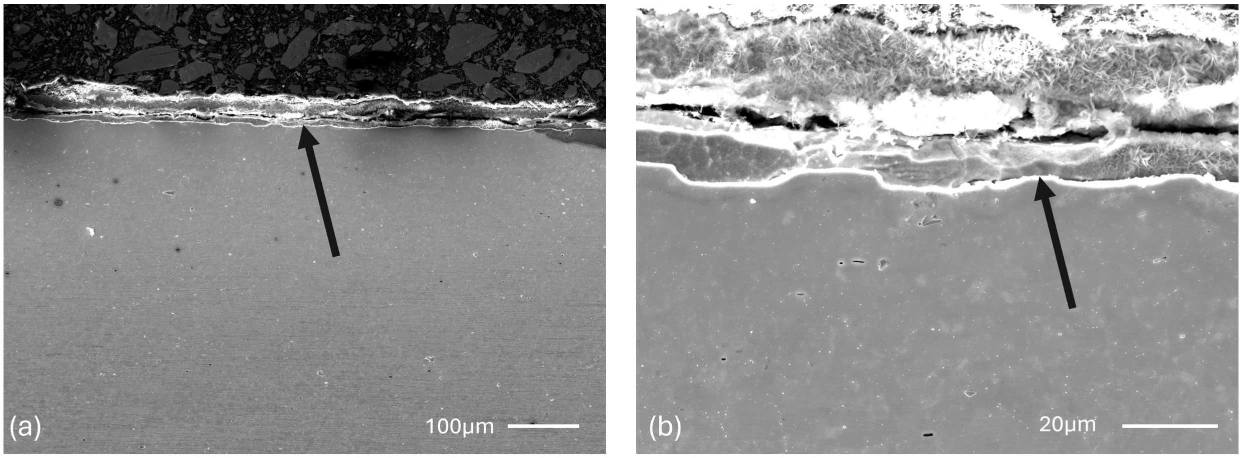

Figure 4.2. SEM pictures of the steel-coating interface at (a) 150x magnification, (b) 1000x magnification

4.1.1. EDS of the Base Material

During the SEM evaluation, an EDS scan of the base material was performed. This analysis aims to determine both the distribution and content of alloying elements. The specific area subjected to the EDS scan is illustrated in Figure 4.3:

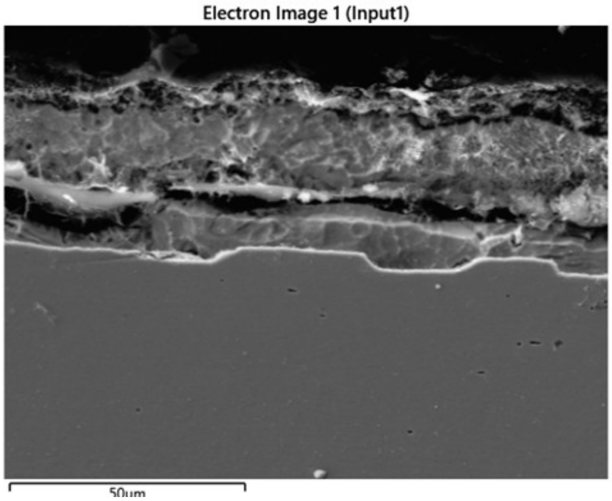

Figure 4.3. EDS area of measurement

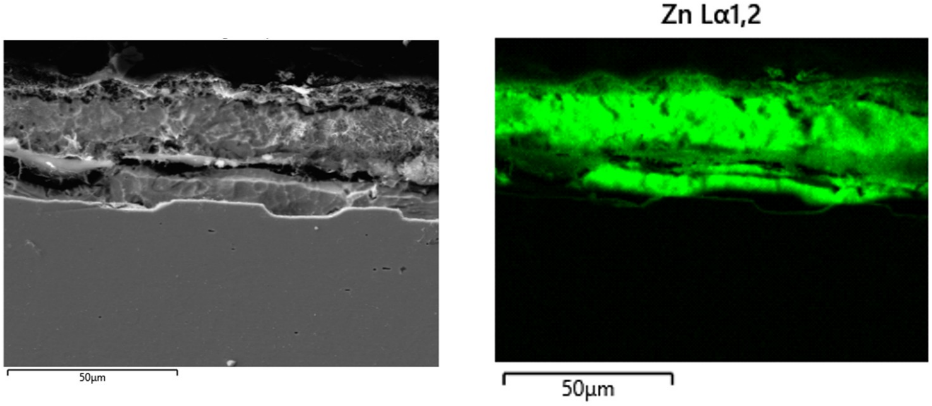

Figure 4.4. Base material EDS and SEM image exhibiting zinc presence

The EDS scan showcased that the major elements found in the microstructure are iron (Fe), zinc (Zn), manganese (Mn), carbon (C), oxygen (O), aluminium (Al) and Nickel (Ni). The distribution of each element is presented in Figure 4.5. Figure 4.4 specifically focuses on the zinc presence of the coating on the base material surface.

Specifically, the distributions of iron, zinc, and manganese in Figure 4.5 distinctly illustrate the interface between the steel substrate and the zinc coating. Both the steel (Table 3.1) and the zinc coating (Table 3.2) are known to contain aluminium. The presence of aluminium and oxygen within the coating can be attributed to the potential formation of aluminium oxide (Al_2O_3). Given the significantly higher melting point of Al_2O_3 compared to zinc, approximately 2072 °C [45] versus 420 °C, this oxide layer could potentially inhibit the flow of liquid zinc into the steel microstructure, thereby mitigating the risk of LME.

4.1.2. EBSD of the Base Material

The base material's phase map (Figure 4.6) reveals austenite as the dominant phase, which aligns with expectations for TWIP steels that are inherently austenitic. Furthermore, Panel b‘s high-angle grain boundaries indicated by the orange lines comprise 68% of grain boundaries observed in the base material. Additionally, the unique grain colour map, presented in Figure 4.6, reveals a fine-grained microstructure with an average

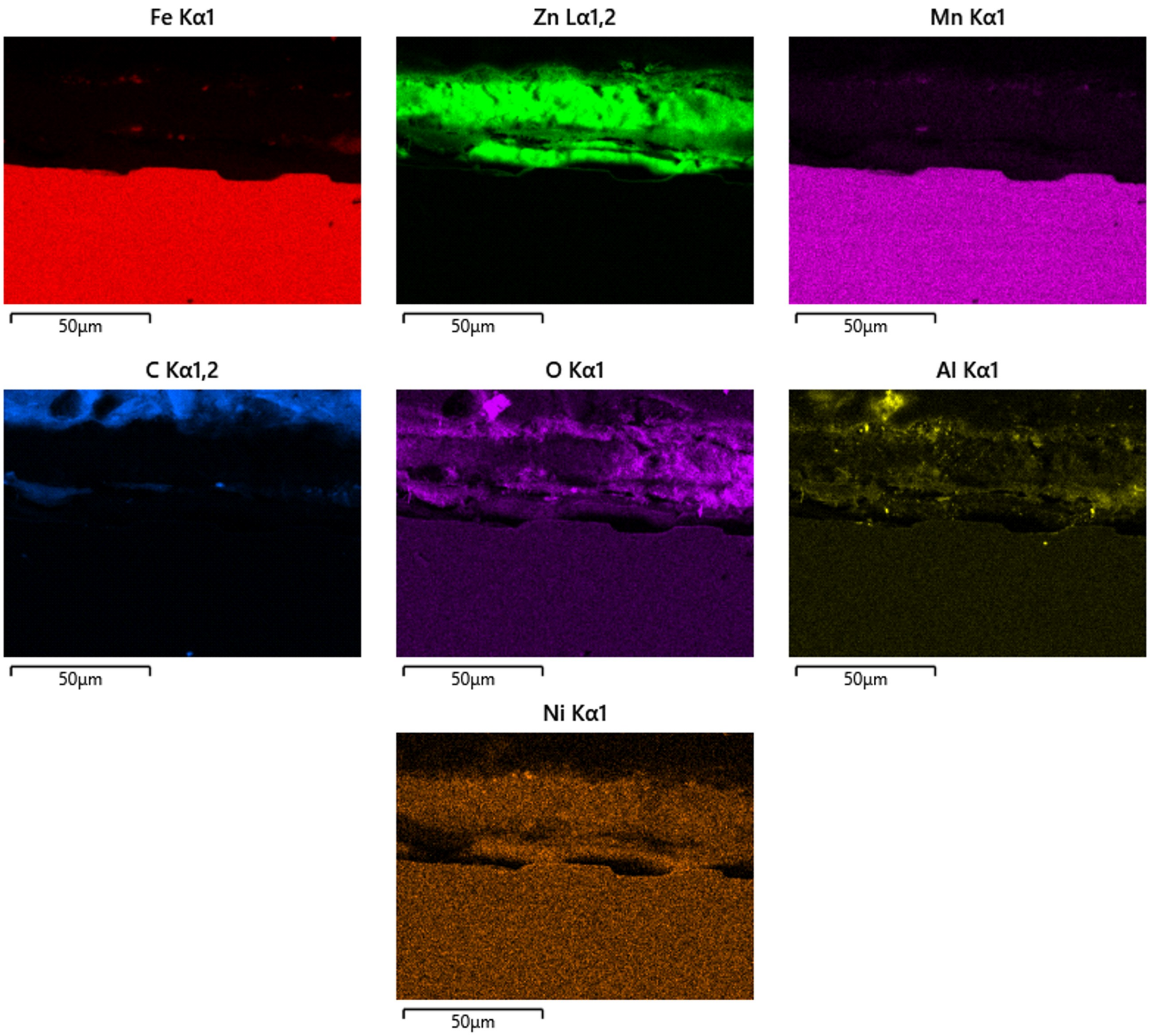
Fe Kα1
Zn Lα1,2
Mn Kα1
C Kα1,2
O Kα1
Al Kα1
Ni Kα1

Figure 4.5. EDS scan of all major elements found in the microstructure

grain size of 16.05 μm, exhibiting characteristics consistent with those observed in the corresponding phase map.

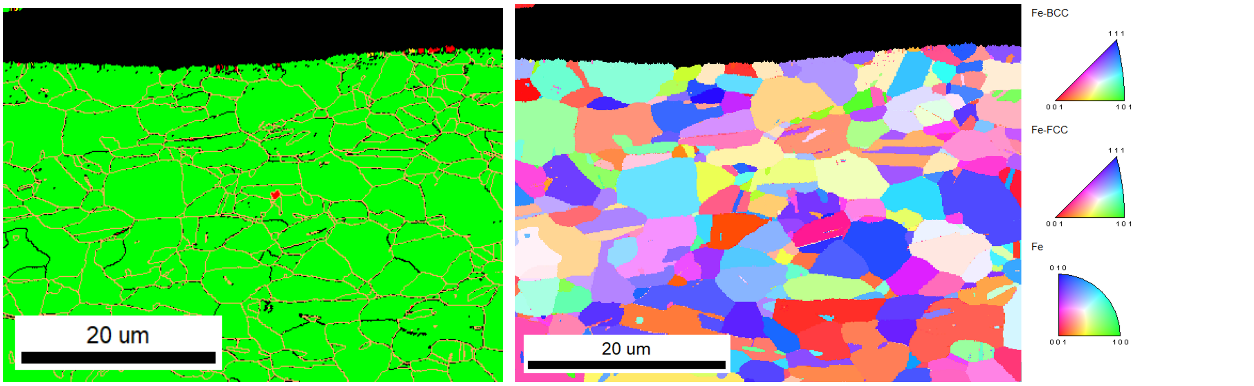

(a) (b)

Figure 4.6. (a) Phase map with green particles showing fcc grains, red particles showing bcc grains, black lines showing low angle grain boundaries and orange lines showing high angle grain boundaries, and (b) unique grain colour map of the base material

4.2. Optical microscopy

In this chapter, the optical microscopy images and analytical results of the welded samples are evaluated.

4.2.1. Double Sheet Samples

Microscopic examination of the double sheet samples via optical microscopy reveals no cracks within the welding region neither in the sample-electrode interface, nor in the shoulders. This absence of cracking is consistent with observations presented in Figure 4.7.

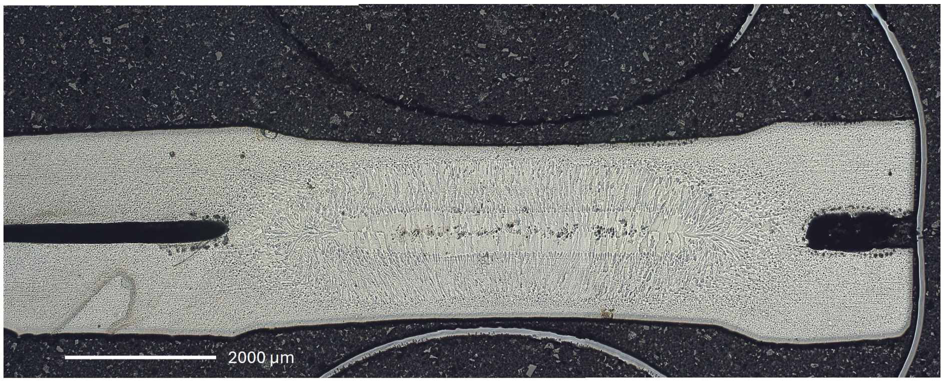

Figure 4.7. Optical microscopical image of HT-55 double sheet sample

4.2.2. Triple Sheet Samples

Figure 4.9 displays a series of optical micrographs from various triple sheet samples, showing the evolution of the crack formation with increasing hold time during the RSW process. The cracks are seen only on the TWIP side of the samples.

Figure 4.8 provides a schematic of the location of the cracks and the identification of the crack types with respect to the location of the electrode. Table 4.1 presents the four primary crack types observed in AHSS grades, which are in line with the characteristic of TWIP steels. These crack types will subsequently

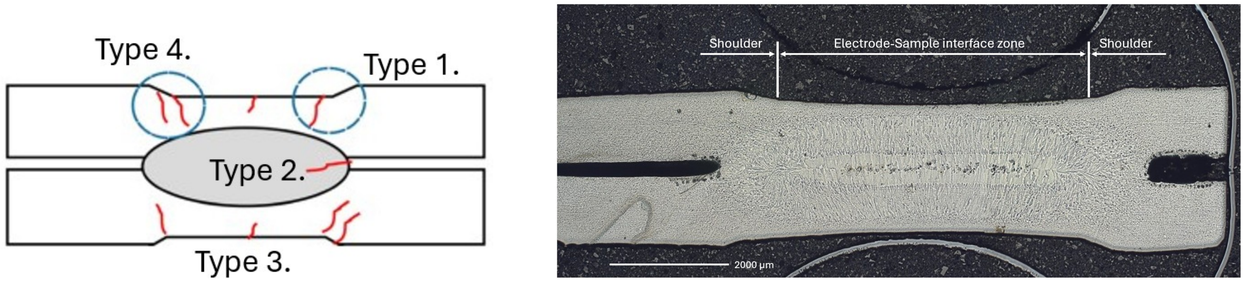

(a) LME crack types

(b) Location of shoulder zones and the electrode-sample interface zone

Figure 4.8. Crack identification methods used in the study

be categorized as either ’shoulder cracks’ or ’interface cracks’, based on their respective locations, depicted in Figure 4.8(b). Type 2 cracks are disregarded in this study.

Table 4.1. Crack types present in TWIP after RSW

Crack type	Attributes	Identification in study
Type 1	Periphery cracks	Shoulder crack
Type 3	Short nugget cracks	Interface crack
Type 4	Cracks originating from faying sheet notches	Shoulder crack

Panels (a) and (b) of Figure 4.9 depict the presence of the cracks in the HT-05 sample, primarily concentrated within the sample-electrode interface region. These cracks are categorized as interface cracks and have a range of depth from 21.7 μm to over 300 μm. Darker regions suggest the presence of porous areas, potentially indicating impurities or remnants from the sanding/polishing preparation phase.

As the hold time increases, samples, such as HT-55 in Panel (c) and HT-105 in Panel (d) of Figure 4.9, demonstrate several interface cracks. The most cracks are observable in Panels (c) and (d) of Figure 4.9, with 8 and 5 cracks, respectively. However, Panel (d) also presents the initial occurrence of a shoulder crack. At HT-155 in Panel(e), a shoulder crack can be seen, whereas for HT-205 in Panel (d) neither shoulder, nor interface cracks are present. Panel (g), representing the HT-255, shows a shoulder crack along with a zinc build-up in the proximity of the crack. This phenomenon is likely attributed to the displacement of liquid zinc towards the periphery during the welding phases, followed by its solidification during the holding period. The HT-305 sample seen in Panel (h) also exhibit a shoulder crack, with a depth of over 330 μm. Finally, the HT-355 sample in Panel (i) displays no surface cracks. This suggests that extended hold times during the RSW process may mitigate LME; however, further evaluation is required for definitive confirmation.

These findings, along with Figure 4.9, support a shift in crack types with increasing hold time. At hold times such as HT-05, HT-55 and HT-105; interface cracks are predominant. This trend changes with increasing hold time, as the shoulder cracks become present from HT-105 to HT-155, concurrently with the gradual disappearance of the interface cracks. This shift in crack location indicates an alteration in the stress distribution, presumably connected to residual stresses. The solidification behaviour of the weld nugget also shifts as a function of hold time. The presence of periphery cracks at longer hold times suggests potential issues related to the heat-affected zone or localized stress concentrations at the outer edges of the weld.

Cracks are consistently observed between the sheets, progressing towards the weld nugget, irrespective of the hold time, as depicted in several Panels, such as (c) and (e), of Figure 4.9. This consistency in the crack location indicates a persistent weakness or stress concentration within the joint. While these observations are noteworthy, a thorough investigation into whether these cracks are LME-induced, along with the precise

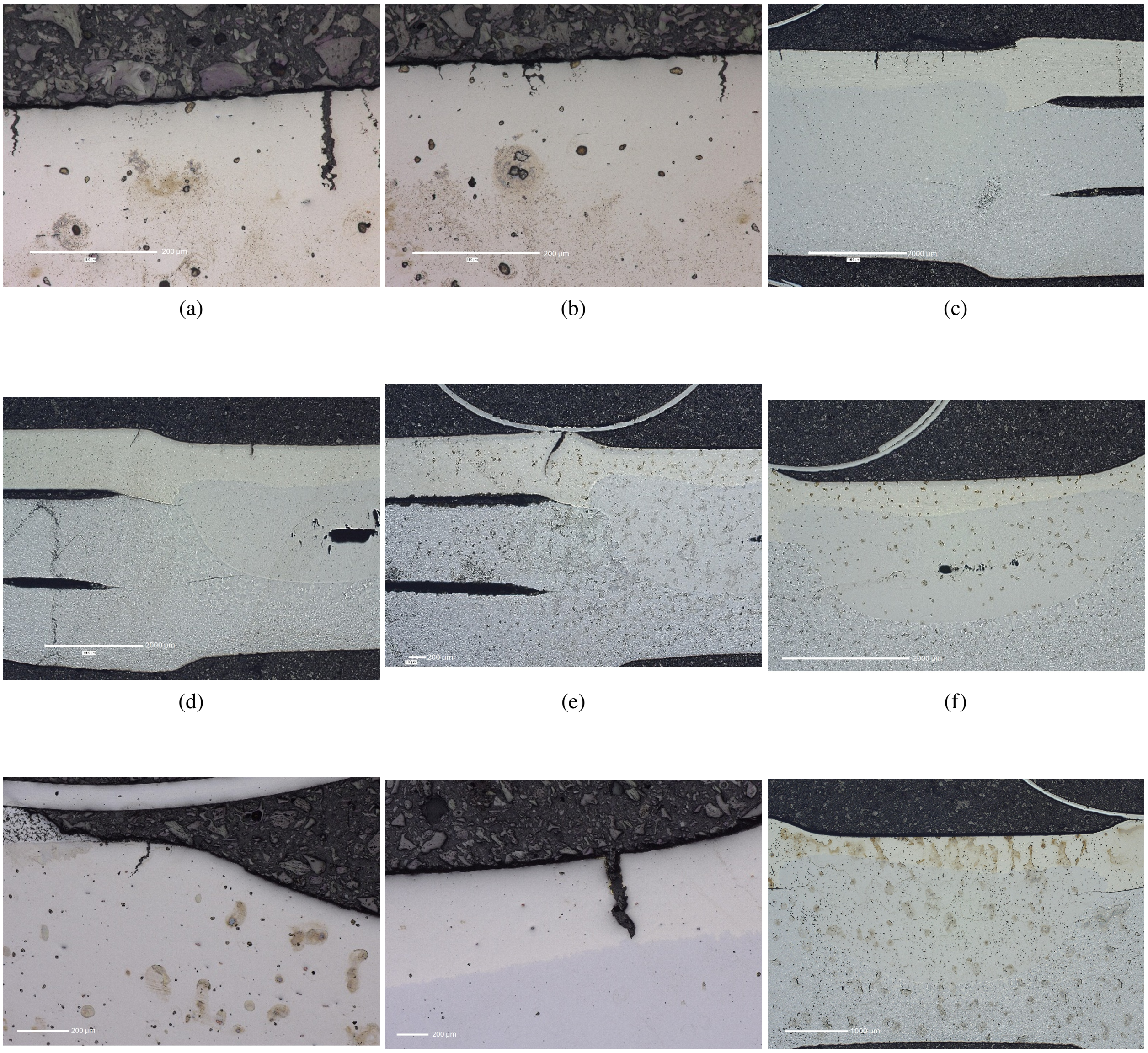

(a) (b) (c)

(d) (e) (f)

(g) (h) (i)

Figure 4.9. Optical microscopy images of triple sheet samples (a) HT-05 sample with 500x (b) HT-05 sample second location with 500x (c) HT-55 with 40x (d) HT-105 sample with 40x (e) HT-155 sample with 40x (f) HT-205 sample with 40x (g) HT-255 sample with 200x (h) HT-305 sample with 200x (i) HT-355 sample with 40x magnification

mechanisms of their initiation and propagation, falls outside the scope of this thesis. Therefore, future studies should focus on comprehensive analyses utilizing SEM, EDS, and EBSD to evaluate these phenomena. Additionally, the presence of dark spots throughout the samples are most likely results of a non-sufficient cleaning phase during the sample preparation.

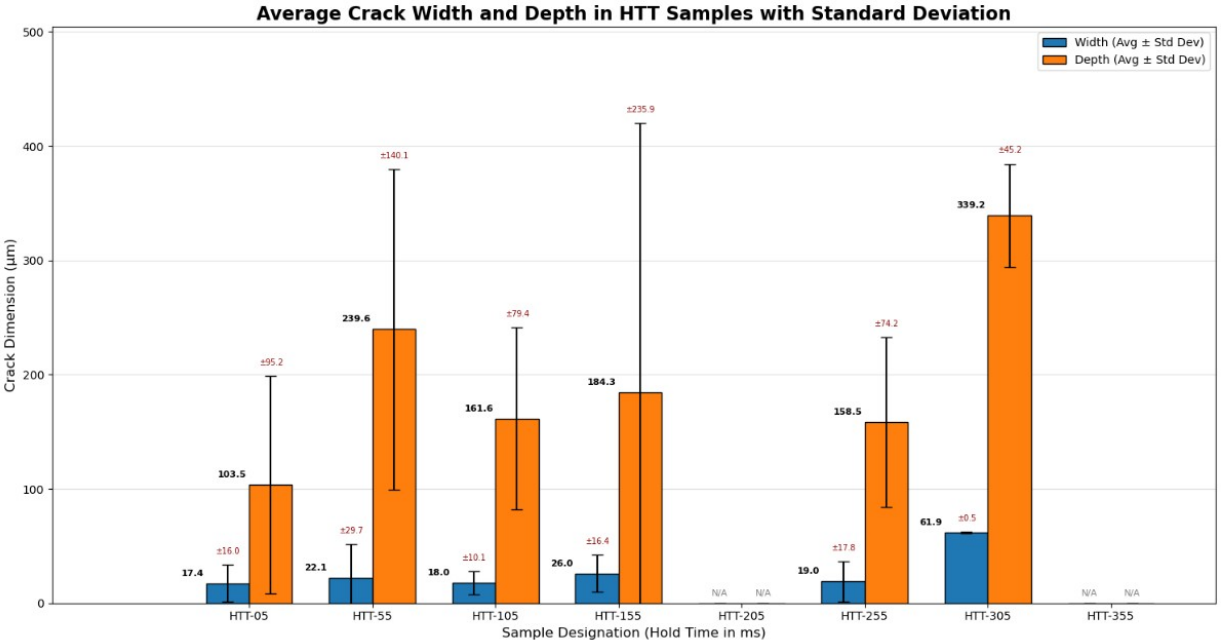

Figure 4.10. Average and standard deviation of crack width and depth

Measurements of average crack width and depth according to Figure 3.3 in Section 3.4.1, presented in Figure 4.10, reveal notable trends. The average crack depth generally increases with hold time for samples exhibiting cracks. This increase is particularly evident between the HT-05 and HT-155 samples; for instance, HT-55 samples exhibit an average crack depth approximately two times greater than that of HT-05, with HT-105 and HT-155 samples, also showing average crack depths exceeding 1.5 times larger. Furthermore, individual cracks demonstrate greater depths and widths with increasing hold time. This observation is coupled with the disappearance of the smaller, more numerous cracks prevalent in samples HT-05, HT-55, HT-105, and HT-155.

This trend is also influenced by the observation that samples with hold times exceeding 105 ms exhibit fewer cracks, contrasting the increase in crack number observed between HT-05 and HT-105. Figure 4.11 illustrates the total number of cracks for each hold time. Notably, samples HT-205 and HT-355 display no cracks. Moreover, samples from HT-155 show less than 20% of the average crack quantity observed in samples up to HT-105. At a hold time of 105 ms, both electrode-sample interface cracks and shoulder cracks are present, indicating the precise hold time at which the shift in crack location initiates. This phenomenon persists in HT-155, with a further reduced number of interface cracks (four in HT-155 compared to twelve for HT-105). Subsequently, only shoulder cracks are observed in samples that exhibit cracking.

Figure 4.12 displays the average distance of cracks from the sample centreline. Please keep in mind that the exact locations of the cross-sections may vary according to Section 3.2, and the data should be interpreted with this in mind. The electrode has a diameter of 32 mm. With the exception of the crack-free HT-205 and HT-355 samples, an overall trend of increasing crack distance from the sample centreline is observed with increasing hold time. This finding is consistent with the observed shift from interface cracks to shoulder cracks as hold time increases.

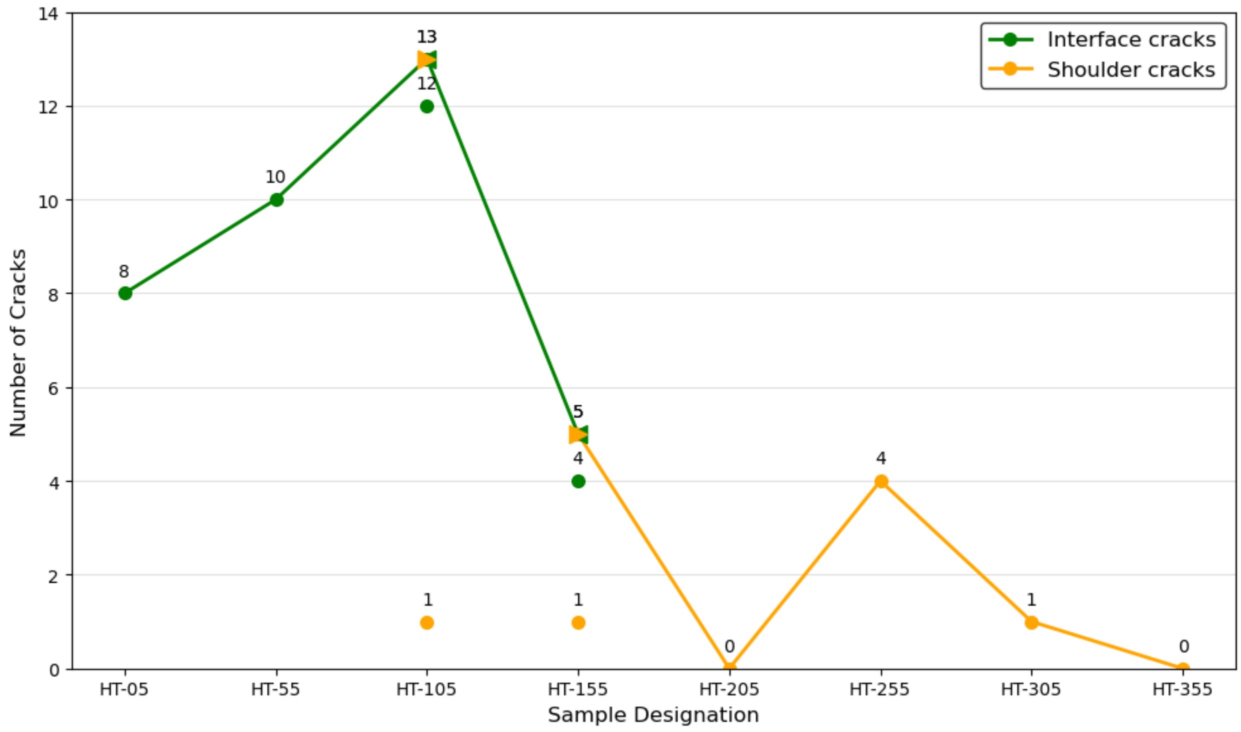

Figure 4.11. The number and location of cracks in each sample

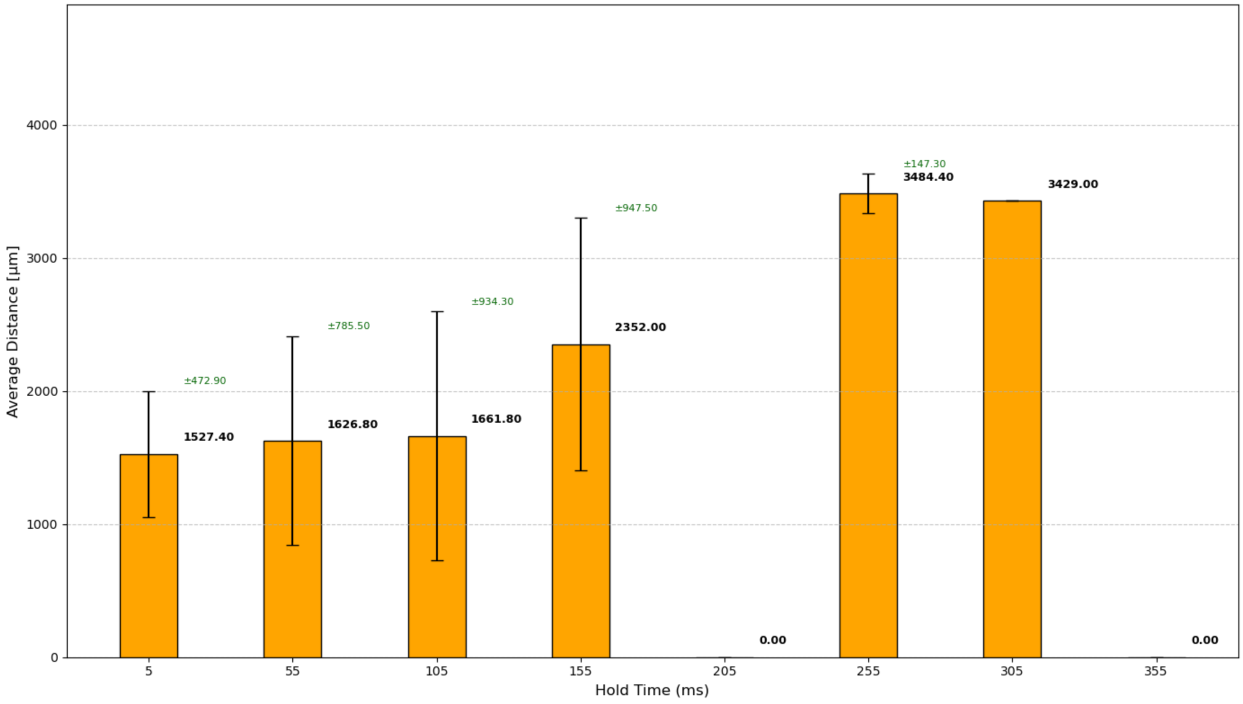

Figure 4.12. Average and standard deviation of crack centreline distances

These findings suggest that longer hold times initially reduce the number of LME cracks, thereby suppressing LME formation. However, the remaining individual cracks at longer hold times are deeper and wider compared to those observed at shorter hold times.

4.3. EDS

This section presents the results of the EDS analyses performed on specific locations of interests: cracks for samples that exhibit cracks, and the shoulder surface with zinc build-up for samples with no cracks. Figure 4.13 displays the EDS analysis results for four selected triple sheet samples.

Panel (a) presents the EDS analysis of an interface crack within the HT-55 sample. The zinc distribution in this region is notable and is primarily concentrated on the surface adjacent to the crack, with a higher concentration observed also within the crack itself. This distribution pattern suggests that it is indeed an LME crack.

Panel (b) of Figure 4.13 illustrates the surface EDS evaluation of the the HT-205 sample's right shoulder. No cracks are visible in this region, however the zinc distribution is most prominent on the sample surface within the shoulder region, indicating a zinc build-up of 5-10 μm thickness.

In Panel (c), the EDS scan results for the HT-255 sample are presented. The presence of a zinc build-up with the thickness of approximately 10-12 μm on the shoulder surface is noticeable, along with zinc presence within the crack itself. This further validates its characterization as an LME crack.

Panel (d) shows the crack in the HT-305 sample. The EDS analysis reveals a strong presence of zinc both on the shoulder surface and within the crack. The zinc build-up is more prominent than in previous cases, with a thickness of at least 15 μm. Therefore, it can be concluded that this crack in the HT-305 sample is LME-induced.

These post-RSW zinc layer thicknesses are less than half of the initial coating thickness on the base material.

4.4. SEM of welds

In this section the SEM images will be evaluated. Figure 4.14 and Figure 4.15 display a collection of SEM images from the triple sheet samples. The primary objective of the SEM analysis is to provide a more detailed examination of cracks and deformities previously identified through optical microscopy, as well as to detect those not observed with optical methods.

Panels (a) and (b) of Figure 4.14 present the HT-05 sample at different magnifications. The visible cracks are located near the right shoulder (300-1000 μm from the shoulder) of the sample but remain within the electrode-sample interface zone, classifying them as interface cracks. Panel (a), at 40x magnification, reveals a crack extending from the surface, whereas Panel(b), a 1000x magnification view of this crack, shows the rough edges and internal features of the crack.

Panels (c) and (d) focus on the HT-55-1 sample, also displaying Type 3 cracks located near the right shoulder. The cracks observed in this sample are wider (22.1 μm compared to 17.4 μm of the HT-05) than those in the HT-05 samples discussed above, as these cracks also exhibit larger average depth (239,6 μm compared to 103.5 μm of the HT-05 samples). Some of these cracks, such as the rightmost one, were not detectable by optical microscopy, underscoring the use case for SEM. Panel (d), at 100x magnification, shows cracks still present in the electrode-sample interface. This indicates that despite potential reductions in overall crack quantity with increased hold time, localized stress concentrations or defects can still lead to crack formation.

Panel (e) displays the HT-105 sample at 100x magnification, focusing on a crack at the left shoulder of the sample. This crack appears less severe or extensive compared to those observed in samples with lower hold times, as three of the five cracks depicted are below 100 μm in depth. In addition, Panel (f) presents an image from the HT-155 sample at 100x magnification, focusing on a crack at the left shoulder. This crack corresponds to the Type 1 periphery/shoulder crack previously identified through optical microscopy. It is a

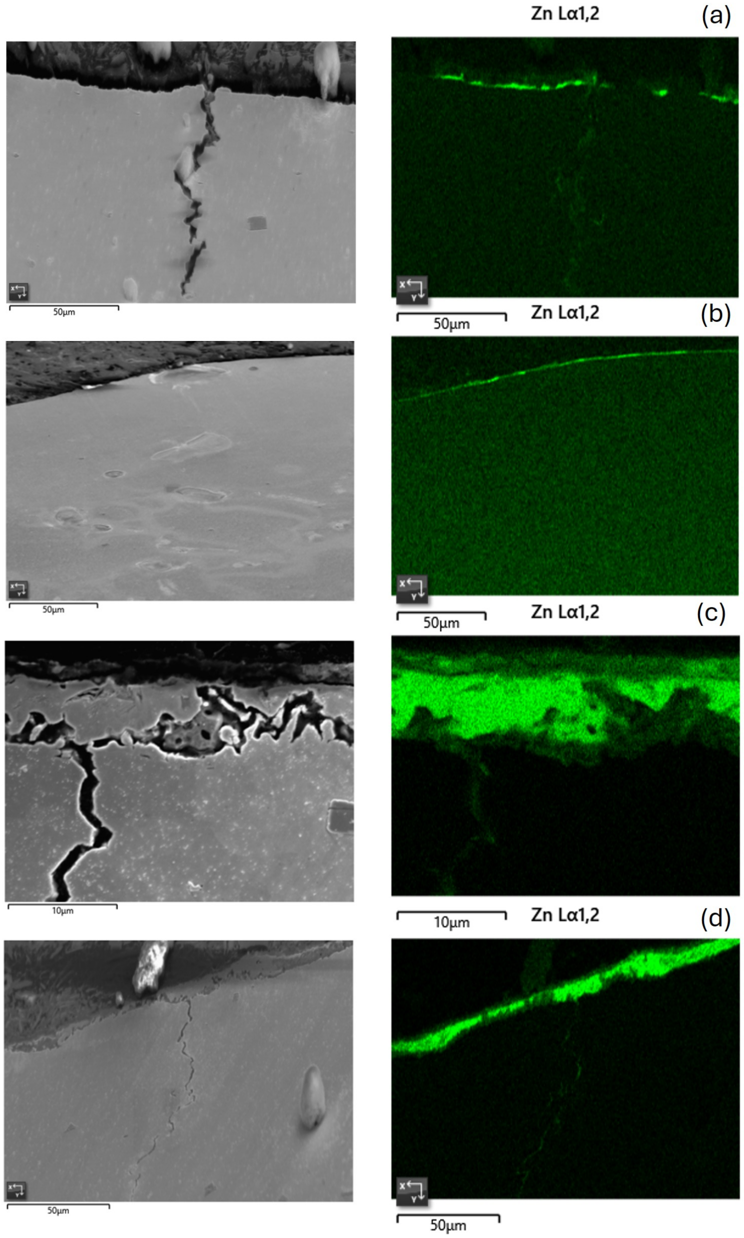

Figure 4.13. EDS and SEM images of several triple sheet samples, showcasing the zinc presence over various hold times: (a) HT-55; (b)HT-205; (c) HT-255; (d) HT-305

substantial crack, with a depth of 653.2 μm and width of 39.4 μm.

The remaining Panels(g), (h), and (i) present samples of HT-205, HT-255 and HT-305, respectively. Panel (g), from the HT-205 sample at 40x magnification, shows no crack presence in the left shoulder region. Panel (h), from the HT-255 sample at 40x magnification, focuses on the right shoulder and shows zinc build-up on the shoulder. This build-up is likely due to liquid zinc being expelled by the electrode during the RSW process, as previously discussed. Lastly, Panel (i), from the HT-305 sample at 40x magnification, shows a crack near the left shoulder, which was also observed in Panel (h).

Figure 4.15 presents SEM images of triple sheet samples ranging from HT-05 to HT-155 ms hold times. These images provide further detailed insight into the crack morphology, complementing previous optical and

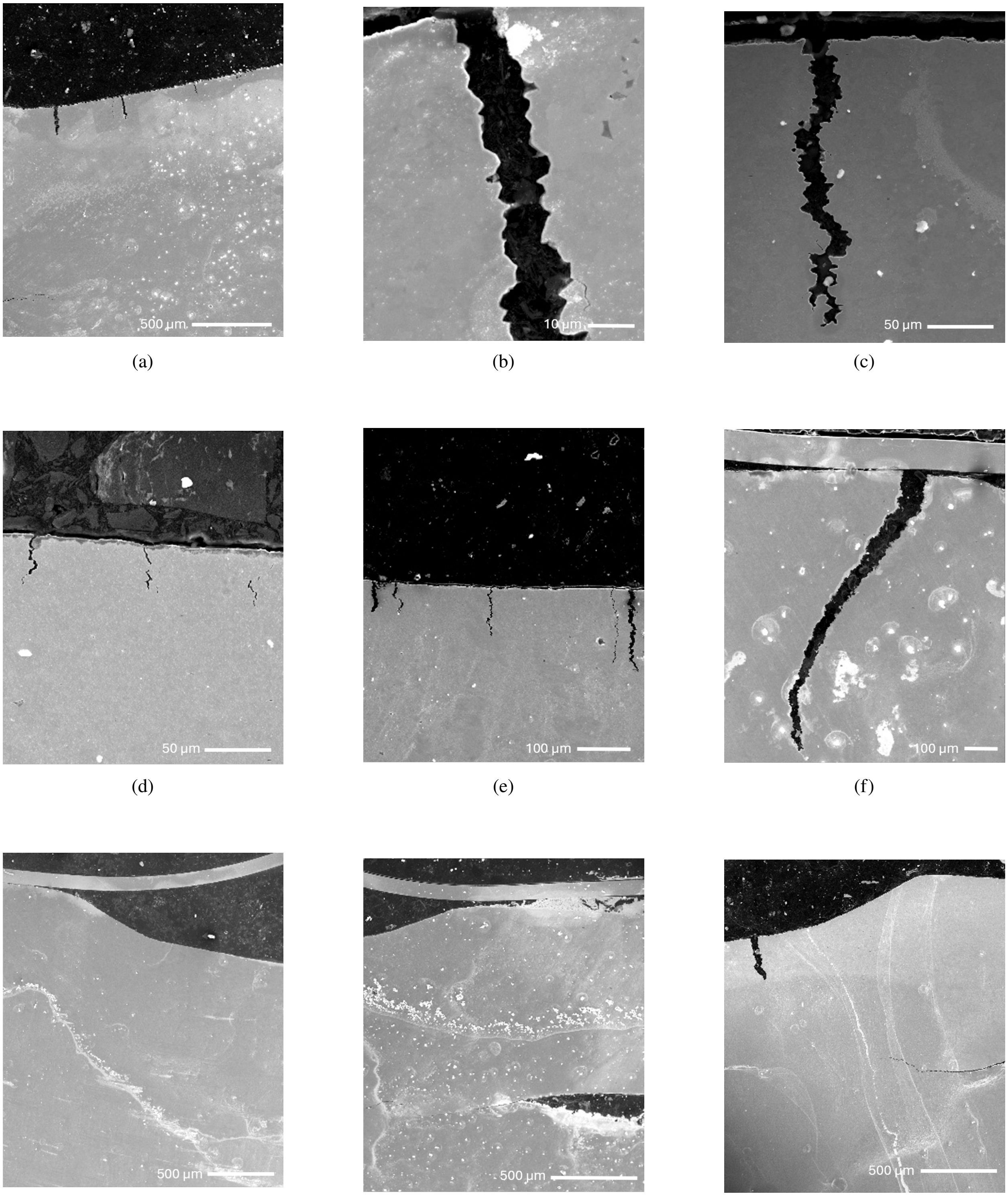

(a) (b) (c)

(d) (e) (f)

(g) (h) (i)

Figure 4.14. SEM microscopy images of triple sheet samples at (a) HT-05 sample with 40x magnification, (b) HT-05 sample with 1000x magnification (c) HT-55 with 350x magnification, (d) HT-55 sample with 350x magnification, (e) HT-105 sample with 100x magnification, (f) HT-155 sample with 100x magnification, (g) HT-205 sample with 40x magnification, (h) HT-255 sample with 40x magnification (i) HT-305 sample with 40x magnification

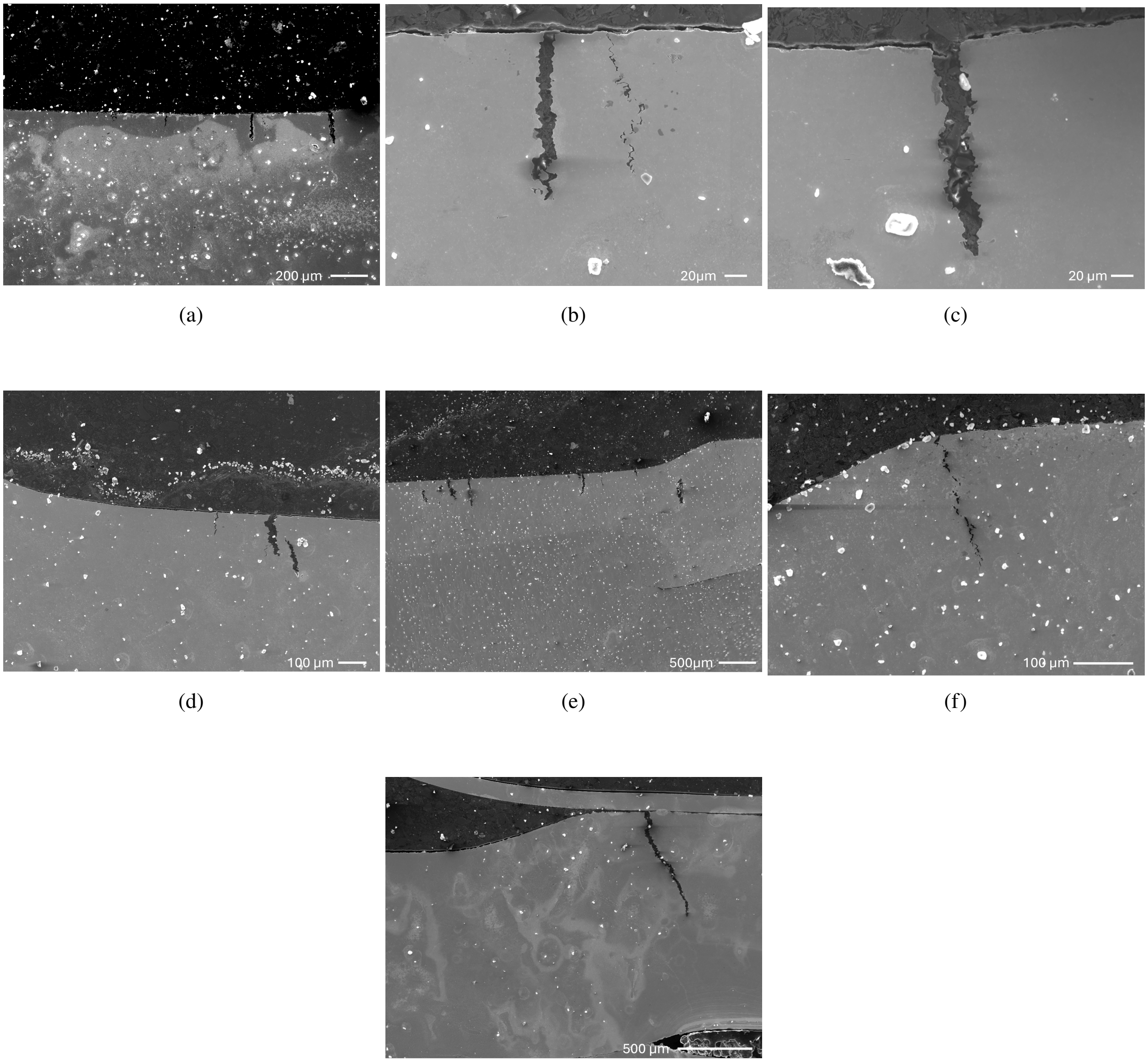

(a) (b) (c)

(d) (e) (f)

(g)

Figure 4.15. SEM microscopy images of triple sheet samples at (a) HT-05 sample at 60x magnification, (b) HT-05 sample at 370x magnification (c) HT-05 at 400x magnification, (d) HT-55 sample with 90x magnification, (e) HT-105 sample with 33x magnification, (f) HT-105 sample with 190x magnification, (g) HT-155 sample with 55x magnification

tabletop SEM analyses.

Panels (a), (b), and (c) of Figures 4.15 display different regions and magnifications of the HT-05 sample, primarily focusing on cracks on the right side of the interface region. Panel (a) provides an overview of multiple cracks at 60x magnification. All of these cracks are below 200 μm in depth. Panel (b) provides a magnified view of cracks closer to the left shoulder at 370x magnification, with depths of 73.4 and 70.9 μm. Panel(c), at an even higher magnification of 400x, focuses on the leftmost crack, which has a depth of 154 μm and a width of 14.1 μm . The SEM higher resolution provides greater detail of the crack boundaries and internal features compared to the initial observations. These cracks exhibit an irregular path, suggesting a complex fracture mechanism.

Panel (d) shows the HT-55 sample at 90x magnification, displaying the cracks located near the right shoulder. These cracks all display depths below 120 μm, with at least one of them having a width below 10 μm. Panel (e) focuses on the HT-105 sample at 33x magnification, showing the right shoulder, while Panel (f), at 190x magnification, focuses on a crack at the right shoulder of the same sample. This right shoulder crack has a depth of 131 μm with a width of 5.3 μm. Panel (g) depicts the HT-155 sample at 55x magnification, concentrating on a crack at the right shoulder. This is the same crack seen in Panel (f) with dimensions of 653.2 μm in depth and 39.4 μm of width.

4.5. EBSD

In this section the EBSD results are discussed along with figures and tables of this chapter depicting these results.

First, Figure 4.16 shows the phase maps of the various samples. Panels (a) and (b) exhibit sample HT-05, where long (179.6 and 70.9 μm respectively) and intergranular cracks are visible, following the boundaries of the green fcc grains. The few smaller, isolated black regions are likely remaining polishing agents. The high-angle grain boundary (HAGB) fraction is 87.2%, indicating a microstructure dominated by high-energy boundaries. The intergranular nature of the cracks and the substantial percentage of HAGBs suggest that these are LME cracks. These finding are in line with the discussion in 2.4.1.

Panel (c) of Figure 4.16 displays the phase map of sample HT-55, where the majority of the indexed area consists of austenite, with a very small fraction of iron bcc. The prominent crack is largely intergranular, following the grain boundaries of the austenite grains. The majority of the grains are HAGBs. As austenitic steels are susceptible to LME, and LME cracks typically occur along high-energy grain boundaries due to preferential zinc wetting (discussed in 2.4.1), the observed cracks are consistent with LME in TWIP steels. For the HT-105 sample, two EBSD scans were performed on two cracks 244.2 and 150.5 μm deep, in Panels (d) and(e). The microstructure of these samples is mainly austenitic and both cracks are intergranular, following the fcc grain boundaries. The HAGB fraction is somewhat lower than for the HT-55 sample (approximately 86% HAGBs), but still over 73% in both cases, indicating that LME is likely present at 105 ms hold times.

In Panel (f), a long (653.2 μm) and wide (39.2 μm) intergranular crack with a tortuous path is visible. The microstructure is dominantly austenitic, with fraction of HAGBs higher than in the previous samples, above 90%. The crack appears larger and more extensive than in previous cases, suggesting that LME is present and potentially severe at 155 ms hold times.

In contrast to previous samples, no crack is visible in the phase map for the HT-205 sample Panel(g). Existing unindexed regions are remnants from the sample preparation phase. The microstructure is still mainly austenitic, with an HAGB fraction of approximately 81%, comparable to previous samples. The absence of a large, continuous intergranular crack suggests that the LME phenomenon might be significantly mitigated at 205 ms hold time.

Due to the large fraction of unindexed parts and poor readability of the outlier HT-255 sample, these results are not used in order not to distort the trend outlined across the other samples. In future research a sample preparation with even longer cleaning phases should be used to deter such unindexed EBSD scans.

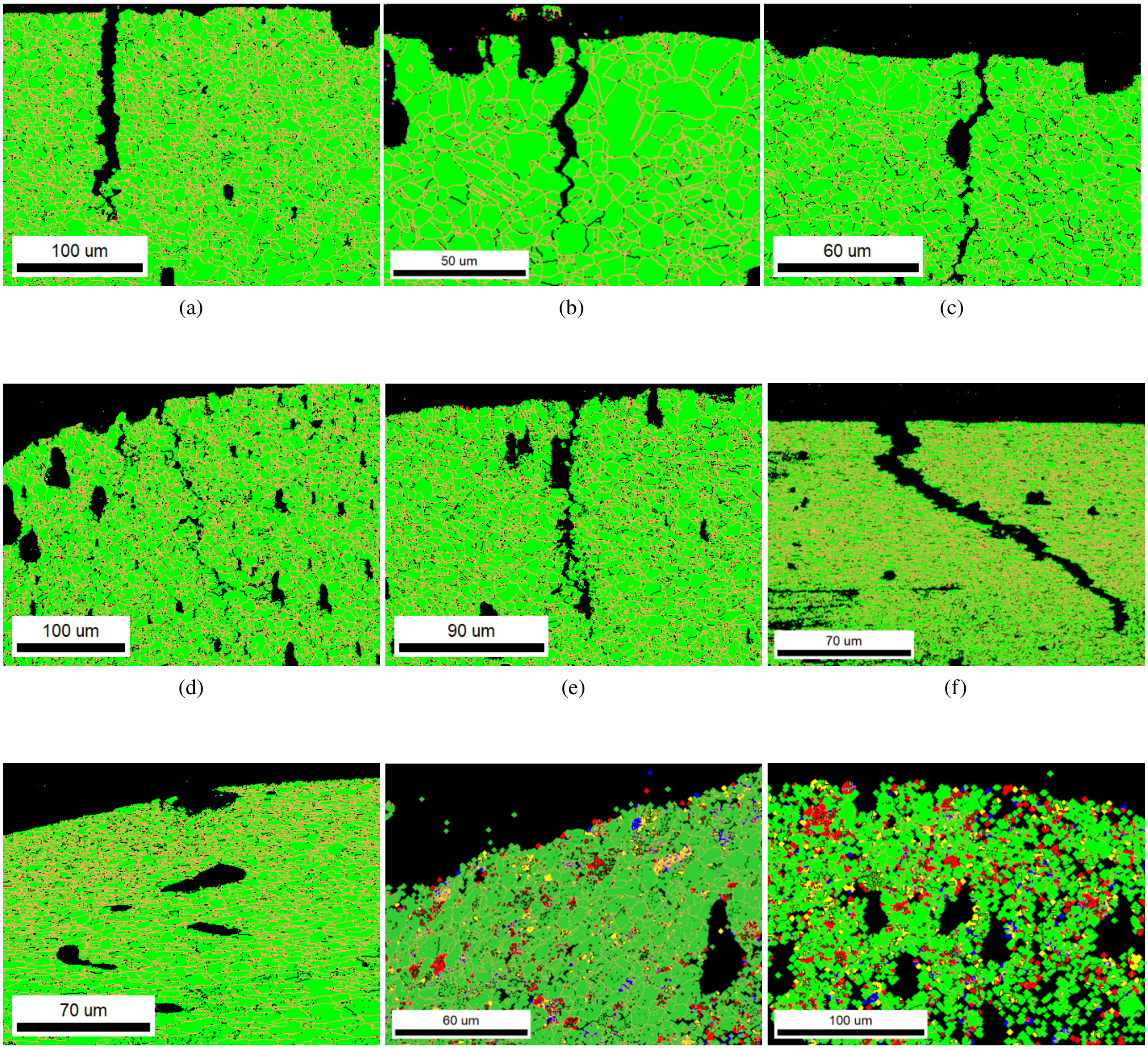

(a) (b) (c)

(d) (e) (f)

(g) (h) (i)

Figure 4.16. Phase map of (a) HT-05 sample (b) HT-05 sample showing other crack (c) HT-55 sample (d) HT-105 sample (e) HT-105 sample showing other crack (f) HT-155 sample (g) HT-205 sample (h) HT-305 sample and (i) HT-355 sample with green particles showing fcc grains, red particles showing bcc grains, black lines showing low angle grain boundaries and orange lines showing high angle grain boundaries

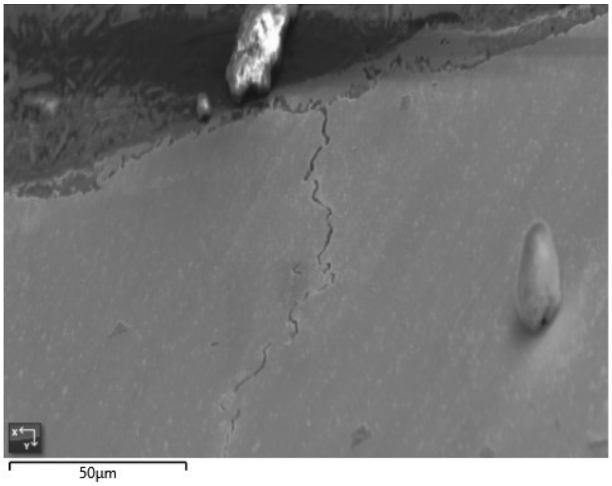

Figure 4.17. SEM image of sample HT-305, showing the crack for better identification in the phase and unique colour grain maps

Panel (h) shows the phase map of the HT-305 sample with a crack 98 μm deep and 9.9 μm wide. The microstructure remains mainly austenitic. A notable FeZn phase is present, however, due to the large fraction of unindexed regions, this could be a misindexation. If confirmed, it would indicate severe LME. The large fraction of unindexed regions necessitated several data cleaning cycles, resulting in the crack appearing very thin on the phase map. Overall, with an 82.9% HAGB fraction and a mainly austenitic microstructure, the sample is similar to previous ones. Figure 4.17 assists in identifying the crack location for both the phase and unique colour grain maps.

Panel (i) of Figure 4.16 presents sample HT-355, exhibiting major fractions of unindexed parts, similar to HT-305, but no cracks are present. The austenite fraction, although still high, dropped to approximately 50% due to the high volume of unindexed parts. The HAGB fraction, while predominantly high angle, decreased to 67.6%, representing a notable reduction compared to previous samples.

In conclusion, the microstructure is consistently dominated by fcc iron across all samples, indicating the preservation of the austenitic nature of the TWIP steel after the welding process. The presence of intergranular cracks and the high fraction of high-angle grain boundaries across most samples strongly suggests the consistent presence of LME. The noticeable decrease in the HAGB fraction in the HT-355 sample, coupled with the absence of cracks, suggests a potential mitigation of LME at longer hold times. The detection of a potential FeZn phase in the HT-305 sample further highlights the role of zinc in LME.

The unique grain colour map in Panels (a) and (b) of Figures 4.18 presents the HT-05 sample. In both figures cracks are propagating along grain boundaries, and such grains display various crystallographic orientations, thereby reinforcing the intergranular nature of the cracks. Panel (c) displays HT-55 and shows that the grains along the crack are relatively equiaxed, with a range of different grain sizes and orientations. The different orientations on the two sides also support the intergranularity of the cracks. The HT-105 sample also exhibits a polycrystalline nature, similar to the HT-55 sample. The black, unindexed areas in Panels (d) and (e), other than the two visible cracks, are most likely remnants from the sample preparation phase. The orientation differences of grains on the two sides of the crack seen in Panel (f) suggest that the crack is intergranular. In Panel (g), the HT-205 sample does not present any cracks, but has a variety of crystallographic orientations. The unique grain colour map evaluation of sample HT-255 is not included in this study, due its high fraction of unindexed regions, which could lead to misleading results driven by incomplete sample preparation. This unique grain colour map of sample HT-305 visually reinforces the phase map. This unique grain colour map shows a highly fragmented and complex microstructure, however large unindexed

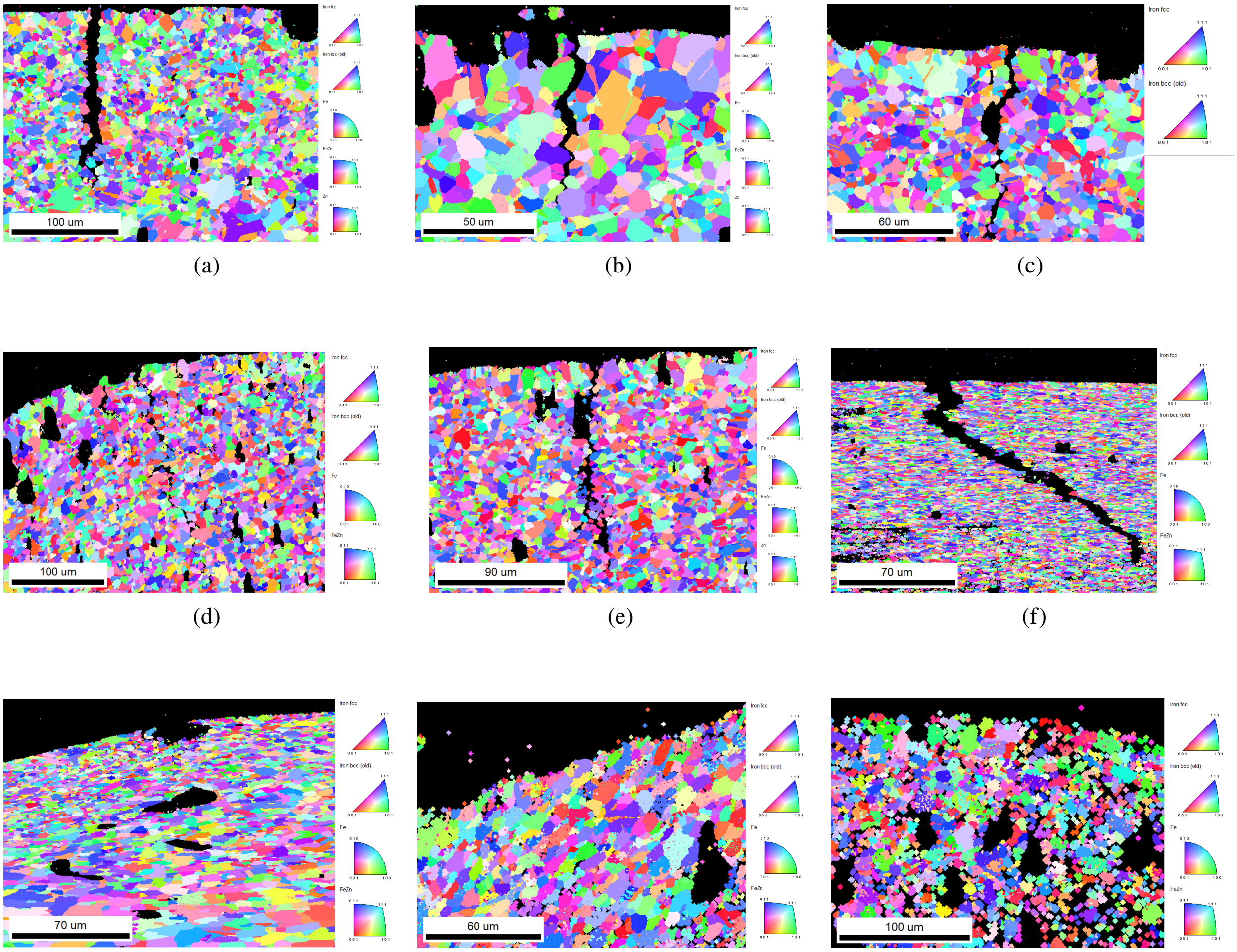

(a) (b) (c)

(d) (e) (f)

(g) (h) (i)

Figure 4.18. Unique grain colour map of (a) HT-05 sample (b) HT-05 sample showing other crack (c) HT-55 sample (d) HT-105 (e) HT-105 sample showing other crack (f) HT-155 sample (g) HT-205 sample (h) HT-305 sample (i) HT-355 sample

areas are present. The indexed regions show a fine grain structure for the fcc phase, with scattered other phases, and the different grain orientations on the two sides of the crack in Panel (h) supports its intergranular nature. The IPF in Panel (i) shows major unindexed parts, but also showcases a fine microstructure.

Overall, across all samples where cracks are present, the unique grain colour maps consistently reinforce the intergranular nature of these cracks, with grains along the crack paths displaying varying crystallographic orientations. The microstructures generally exhibit a polycrystalline nature. The increasing presence of unindexed regions in unique grain colour maps at at hold times exceeding 255ms indicates challenges in obtaining clear grain data, possibly due to increased microstructural complexity or sample preparation issues.

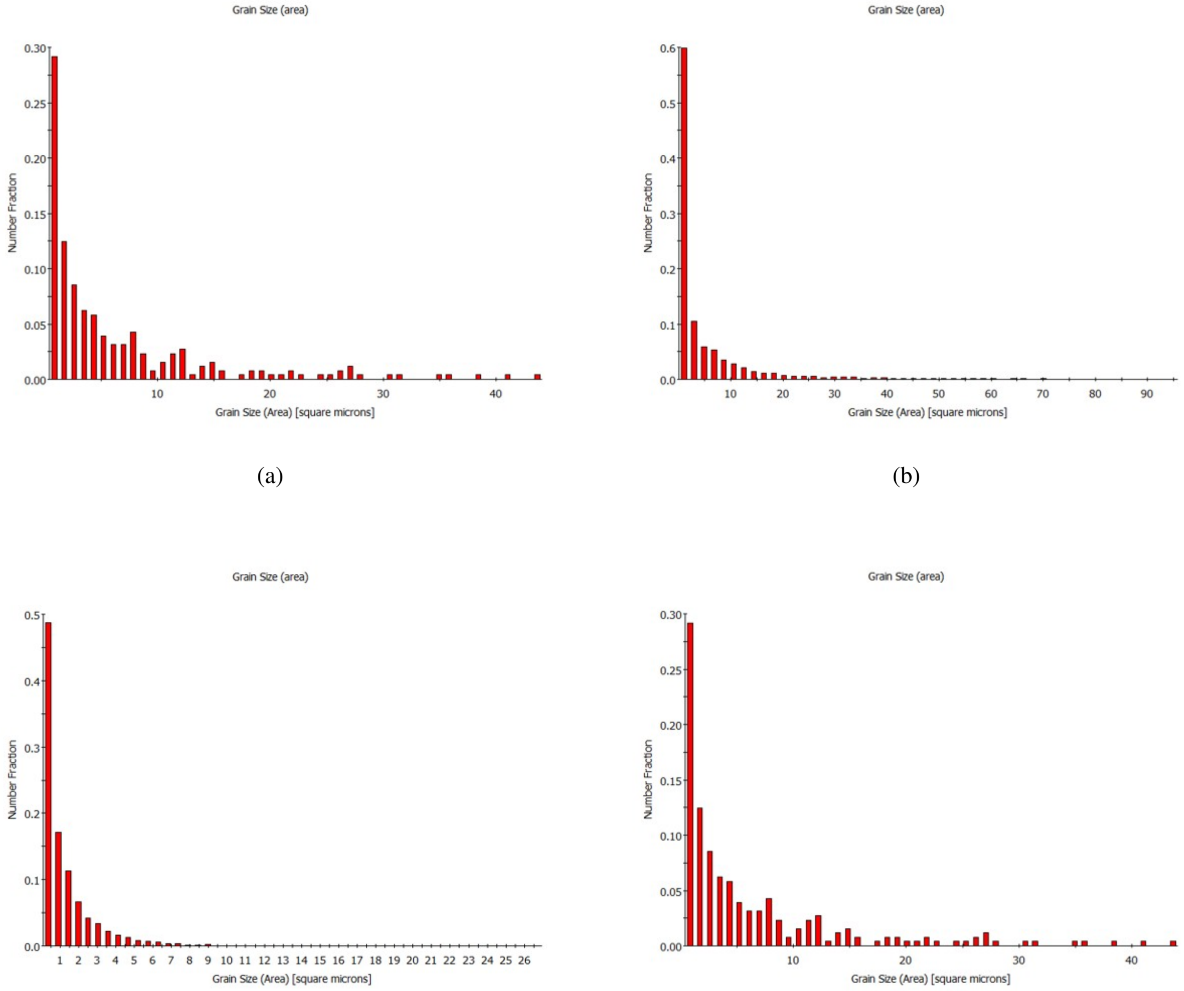

(a)

(b)

(c)

(d)

Figure 4.19. Grain size distribution across several samples, (a) Base material, (b) Sample HT-55, (c) Sample HT-155 (d) Sample HT-355

Figure 4.19 illustrates the grain size distribution of the (a) Base material, and samples HT-55, HT-155, and HTT-355, in Panels (b), (c), and (d), respectively. When interpreting the results, it is crucial to account for the variations in the scales of both the grain size and number fraction axes. The grain structure of the samples becomes coarser when compared to the base material. The quantity of larger grains increases with the hold time increasing. With longer hold times, as seen in Panel (d), where the peak at smaller grains broadens compared to the earlier results, while at larger grain sizes also become more present. The remaining grain size distribution graphs, both by ’Total grain area’ (Section 7.6.1) and ’Number of fractions’ (Section 7.6.2), can be found in the Appendix.

EBSD results are analysed to determine the distribution (average and standard deviation) of grain size and those of grain shape’s major and minor axes, using EDAX OIM Analysis 8 software. Table 4.3 presents the distribution of grain size, while Tables 4.4 and 4.5 show the corresponding values for the major and minor axes of grain shape, respectively. The summa area of the scans, provided in Table 4.2, is calculated to normalize the average grain values, facilitating comparative analysis across samples.

Table 4.2. Calculated summa area for samples

Sample	Summa Area of scan [μm^2]
Base Material	1629.43
HT-05	9905
HT-55	13331
HT-105	36131
HT-155	22090
HT-205	23715
HT-255	728857
HT-305	15647
HT-355	32960

Table 4.3. Average and standard deviation of Grain Size for sample, calculated using EDAX OIM Analysis 8 software

Sample	Average Grain Size [μm^2]	Standard Deviation[μm^2]
Base Material	16.05	11.05
HT-05	35.82	25.78
HT-55	27.99	30.65
HT-105	26.81	24.98
HT-155	3.21	2.79
HT-205	59.56	39.69
HT-255	-	-
HT-305	43.13	40.32
HT-355	56.91	51.81

Figures 4.20, 4.21 and 4.22 illustrate the average and standard deviations of grain size, major axis, and minor axis for each sample, respectively. While a linear evolution with hold time is not observed, the trends in average grain size and standard deviation values are consistent across all three parameters. This consistency indicates an isotropic response of the grains to the processing changes. A notable example of this consistency is the sharp drop observed at the HT-155 sample across all three tables.

A series of graphs were generated to represent the percentage of the total area occupied by each grain size

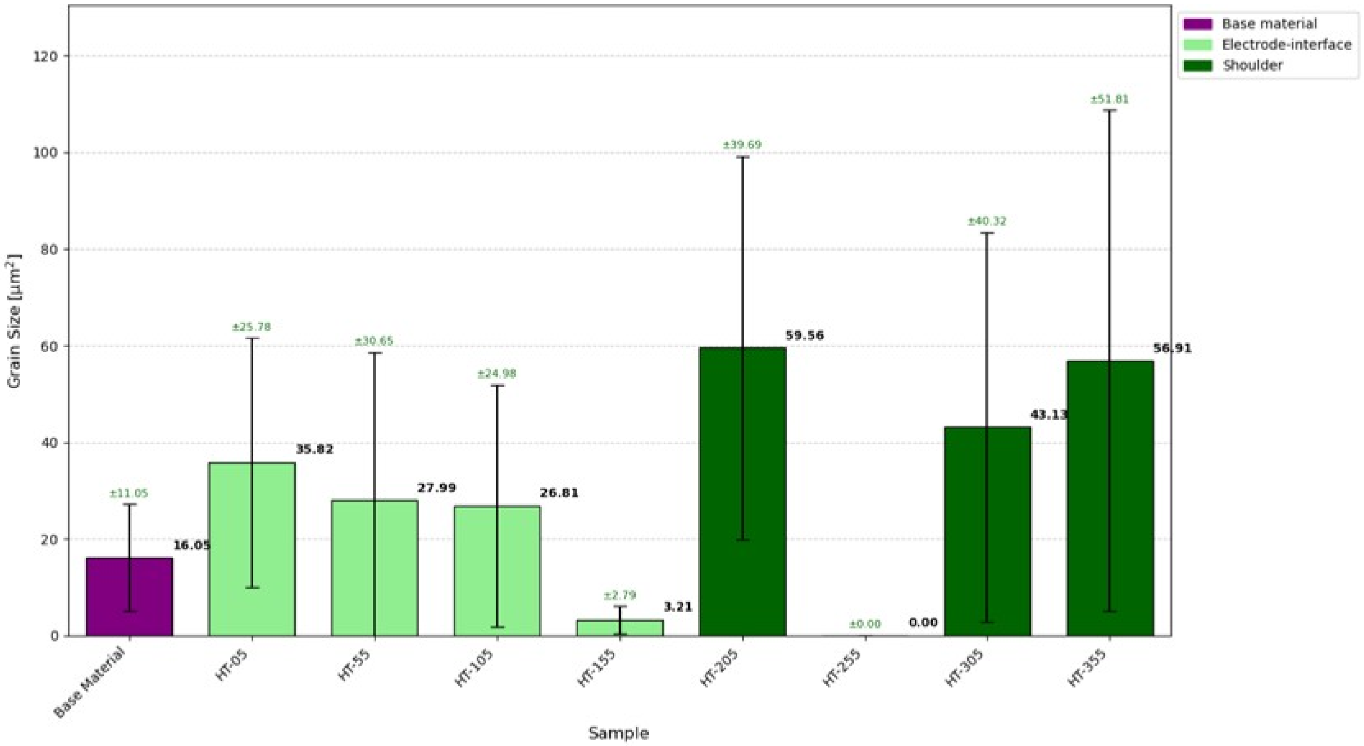

Figure 4.20. Average and standard deviation of overall grain size

Table 4.4. Major axis average and standard deviation of Grain Size for each sample, calculated using EDAX OIM Analysis 8' software

Sample	Average Major Axis Size [μm]	Standard Deviation[μm]
Base Material	3.26	1.45
HT-05	5.37	3.70
HT-55	3.79	2.04
HT-105	5.23	2.78
HT-155	1.79	0.97
HT-205	5.52	3.89
HT-255	-	-
HT-305	4.36	2.78
HT-355	4.59	2.78

type, as shown in Figure 7.2 in the Appendix.

At short hold times, specifically 05 ms and 55 ms, the microstructure is characterized by very fine grains, with distinct peaks at the smallest sizes (below 5μm) and a relatively narrow spread. Grain growth initiates at 55 ms, leading to a broader distribution. At hold times such as 105 ms to 155 ms, the formation of larger grains becomes apparent, seen in Panel (b) of Figure4.19. A fluctuating behaviour is observed between 155 ms and 355 ms. For instance, while the majority of grains for HT-155 are below 6μm (seen in Panel (c) of the same figure), the distribution is much broader for HT-355 with high distribution until 20μm, and occasional

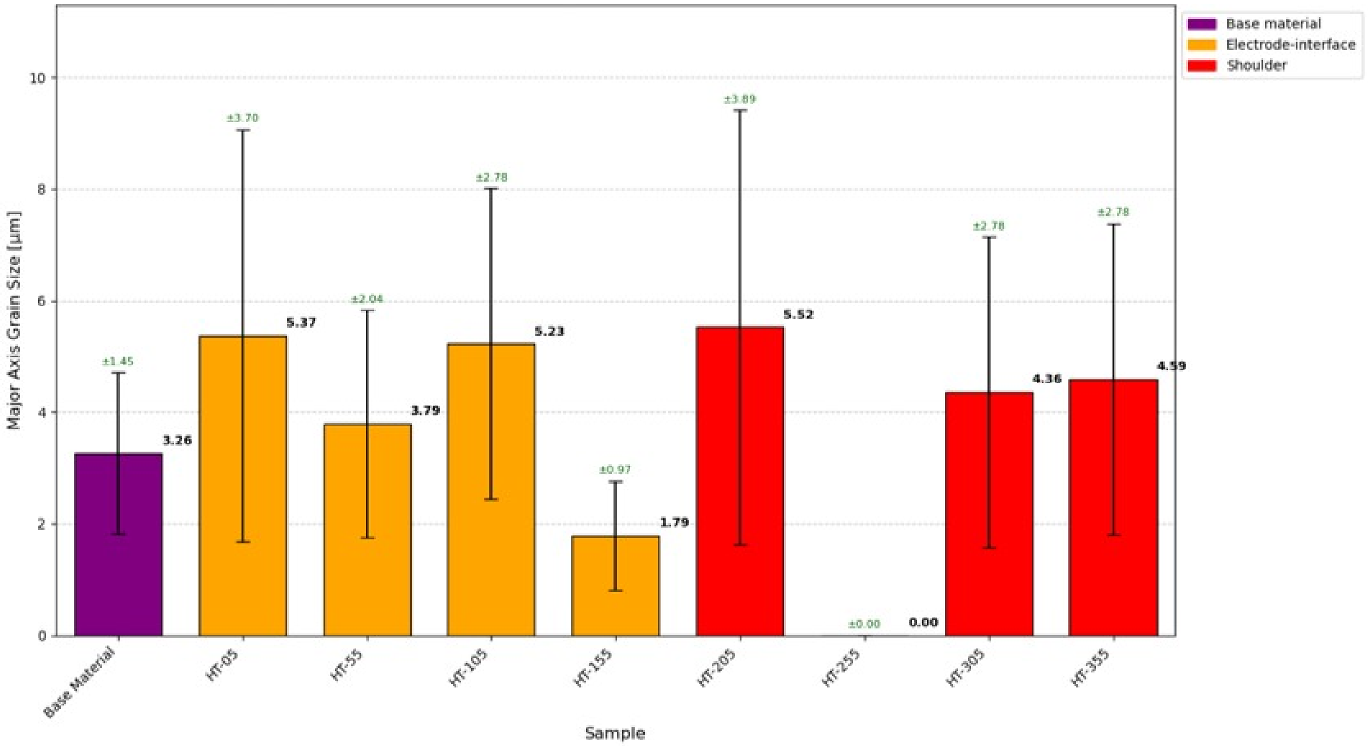

Figure 4.21. Major axis average and standard deviation of Grain Size

Table 4.5. Minor axis average and standard deviation of Grain Size and for each sample, calculated using EDAX OIM Analysis 8' software

Sample	Average Minor Axis Size [μm]	Standard Deviation[μm]
Base Material	1.35	0.68
HT-05	2.53	1.67
HT-55	1.84	1.05
HT-105	2.44	1.20
HT-155	0.52	0.20
HT-205	1.44	1.00
HT-255	-	-
HT-305	1.77	1.00
HT-355	2.13	1.15

peaks above 50μm as well (seen in Panel (d)).

The overall grain size in Figure4.20 demonstrates a fluctuating, but generally increasing trend with hold time after an initial period. The base material exhibits an average grain size of approximately 16.05 μm. For HT-05 shows an average grain size of approximately 35.82 μm, indicating an initial increase. This trend continues for HT-55 (27.99 μm) and HT-105 (26.81 μm). A decrease is observed at HT-155, with a significantly finer average grain size of 3.21 μm, which will be discussed in Chapter 5. Subsequently, for longer hold times, the grain size increases, with HT-205 (59.56 μm), HT-305 (43.13 μm), and HT-355 (56.91

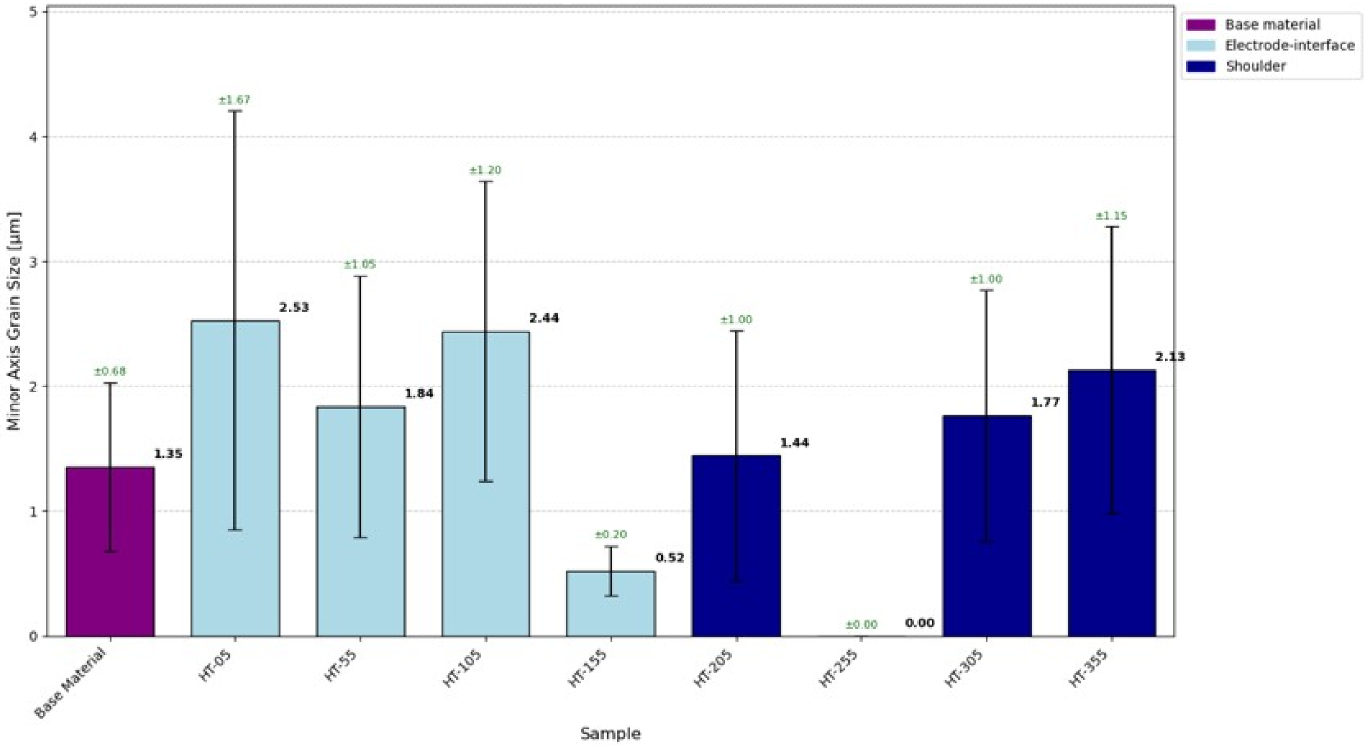

Figure 4.22. Minor axis average and standard deviation of Grain Size

μm) exhibiting larger grain sizes, particularly in the shoulder region.

In Figure4.21, the analysis of the major axis grain size reveals similar tendencies. The base material has an average major axis grain size of 3.26 μm. HT-05, HT-55, and HT-105 samples show average major axis grain sizes of approximately 5.37 μm, 3.79 μm, and 5.23 μm, respectively. Consistent with the overall grain size, a decrease is evident at HT-155 (1.79 μm) . Following this, HT-205, HT-305, and HT-355 display increased major axis grain sizes, approximately 5.52 μm, 4.36 μm, and 4.59 μm, respectively. The standard deviations for the major axis also follow the general trend of being larger for larger average grain sizes.

The minor axis grain size seen in Figure4.22 largely follows the patterns observed for the overall and major axis grain sizes. The Base Material shows an average minor axis grain size of 1.35 μm. HT-05, HT-55, and HT-105 exhibit values of approximately 2.53 μm, 1.84 μm, and 2.44 μm, respectively. The pronounced reduction at HT-155, as this sample has an average minor axis size of 0.52 μm is again a consistent feature across all grain size parameters. Subsequent samples, HT-205, HT-305, and HT-355, demonstrate increased minor axis grain sizes of approximately 1.44 μm, 1.77 μm, and 2.13 μm, respectively.

Across all evaluated grain size parameters (overall, major axis, and minor axis), a consistent pattern emerges: There is an initial increase in grain size from the base material at hold times, such as HT-05, HT-55 and HT-105, followed by a significant refinement at HT-155 ms. This refinement is characterized by a notable decrease in average grain size and a reduction in standard deviation, indicating a more uniform and finer microstructure. Beyond HT-155 ms, a re-coarsening of the grain structure is observed, albeit with some fluctuations. The consistency of these trends across all three grain shape parameters suggests an isotropic response of the material's grain structure to the processing conditions. The varying standard deviations indicate changes in the homogeneity of the grain size distribution with increasing hold time.

Due to its poorly indexed scans, the dataset of sample HT-255 is not taken into account during the evaluation and calculation phases, as it does not accurately represents the sample, and could give rise to false trends.

5. Discussion

LME is a phenomenon that occurs during the RSW of zinc-coated TWIP steel. This process involves the penetration of liquid zinc along the steel's grain boundaries. For LME to occur, several conditions must be met. The temperature must be high enough to melt the zinc, but not so high that the zinc evaporates. The presence of high-angle grain boundaries, particularly in fcc structures, facilitates the penetration of the liquid zinc. This process is further promoted by the presence of tensile stresses.

The primary process parameters in RSW are the electrode force, welding current, and weld time, which are responsible for creating the weld nugget and determining the conditions at the plate surfaces. This thesis, however, focuses on a less commonly studied parameter, the holding time. This is the duration for which the electrode force is maintained after the welding current is switched off. The specific welding conditions used in this study are detailed in Table 3.4.

This section provides a concise overview of the microscopic evaluation results, aiming to establish a foundation for understanding of the underlying effects, processes, and theories that govern the observed changes in crack behaviour with varying hold times. These proposed mechanisms and theories are further substantiated by findings from the relevant existing literature.

5.1. Optical Microscopy and SEM results

This section synthesises findings from optical microscopy and SEM evaluations, establishing a basis for understanding the underlying mechanisms that influence crack behaviour as hold times vary.

For the double-sheet samples, neither optical microscopy, nor SEM reveals any visible cracks within the weld region. This observation suggests that the welding parameters, identical to those used for the triple-sheet samples, either effectively mitigate LME in double-layered configurations, or necessitate specific optimisation for such geometries.

In contrast, a pronounced difference is observed in the triple-sheet samples. Most of these samples display a distinct progression of crack formation with increasing hold time. At lower hold times, numerous cracks appear evident, primarily localised at the sample-electrode interface. These cracks exhibit variable width and depth, which is consistent with Type 3, short nugget cracks described in [34].

During the RSW process, the weld nuggets in both the double-sheet and triple-sheet samples are found to be of comparable dimensions. Specifically, the nugget width is approximately 6300 μm and the nugget height is around 1800 μm in both cases. The primary distinction between these samples is the nugget's distance from the sample surface, which is close to 200 μm for the double-sheet configuration and 700 μm for the triple-sheet configuration. Since the same welding parameters are applied to both, the observed difference may be attributed to variations in the stress state of the samples. These stresses appear to be insufficient to initiate cracking in the double-sheet samples. There is also the possibility that more zinc evaporated in case of the double-sheet samples, due to the welding parameters being set for the thicker, triple-sheet ones. To determine what drives this difference, future research should incorporate modelling and in-situ temperature measurements to better understand the role of Joule heating and the stresses present in the welding process.

A noticeable reduction in crack quantity is observed with increasing hold time, with a transition occurring between the HT-105 and HT-155 samples. This transition is marked by the emergence of Type 1 and Type 2, so called 'shoulder cracks', which become more prevalent at higher hold times. Beyond HT-255, interface cracks are no longer visible, with only shoulder cracks being present. This spatial shift, from more centrally located interface cracks to shoulder cracks at the weld periphery, indicates a possible influence of either stress distribution or heat distribution factors during the solidification phase post-welding. These are, in turn, affected by the duration of the hold time. Furthermore, a visible zinc build-up is also identified in all samples subjected to longer hold times. This is most likely attributed to the mechanical expulsion of liquid zinc towards the outer periphery of the sample due to the electrode during the welding process.

Next, the quantitative analysis of crack dimensions validates these qualitative observations. A consistent trend of fewer, but deeper cracks is associated with longer hold times. While an initial increase in crack number is observed up to the HT-105 sample, some longer hold time samples are entirely crack-free. Moreover, crack distance measurements reveal an increasing average distance between cracks and the sample's centreline at longer hold times, supporting the observed migration of cracks from the interface towards the shoulder regions. These findings must be interpreted with caution, however, as the measured cross sections could differ either due to the cutting method mentioned in Section 3.2, or the thickness of material that was lost in sanding and polishing sequences.

These findings imply that while extended hold times may suppress the formation of LME-related cracks, the cracks that do form tend to be more substantial in depth.

To further substantiate the optical microscopy findings and provide further insights, a series of SEM analyses are conducted, allowing for higher-resolution examination. This proves beneficial, as many very thin cracks (width below 5 μm), often proximal to those identified optically, are only discernible under higher magnification SEM. The SEM results consistently confirm the findings of optical microscopy tests, reinforcing the crack-free observations for the HT-205 and HT-355 samples. The fore mentioned zinc build-up is also more distinctly visible under SEM. Additionally, the SEM helps reveal irregular crack paths, which strongly indicate the intergranular nature of these cracks, consistent with LME mechanisms ([46]).

5.2. EDS results

For the HT-55 sample, zinc is not only located on the sample surface adjacent to the cracks, but also observed within the cracks. Its uniform distribution in the cracks indicates that it is LME-induced, and suggests that crack propagation is not hindered due to insufficient zinc availability. The EDS scan of HT-205 reveals no shoulder cracks, however, a zinc build-up present on the shoulders suggests that the coating migrated to these regions in liquid phase during the welding process, most likely due to the electrode. The HT-255 sample presents a similar observation, where zinc is not only visible within the crack itself but also as a build-up on the surface. This surface accumulation verifies the findings from both optical microscopy and SEM, which initially indicated the presence of such a build-up. The zinc content within this crack confirms its classification as an LME crack. Also for HT-305, EDS analysis confirms the presence of zinc within the crack. A zinc deposit is found on the sample surface, further supporting the findings from SEM and optical microscopy: the zinc coating demonstrably migrates towards the shoulders with increasing hold time. Therefore the thickness of the zinc build-up on the shoulders also increases with the hold time, however the thickness of the build-up is never larger than 50-60% of the original zinc coating's thickness on the base material.

5.3. EBSD results

Across all samples, the microstructure is predominantly composed of fcc iron, indicative of the stable austenitic phase characteristic of TWIP steels, as seen in Figure 4.16. This consistency underscores that the welding process largely preserves the austenitic nature of the base material. Cracks observed in samples HT-05 (Panels (a) and (b) of Figure 4.16), HT-55 (Panel (c)), HT-105 (Panels(d) and (e)), and HT-155 (Panel (f)) are consistently intergranular, propagating along the boundaries of the fcc grains. This intergranular nature is further corroborated by the unique grain colour maps (Panels (a-f) of Figure 4.18), where cracks are observed to traverse regions with distinct crystallographic orientations on either side. This reinforces the crack propagation along grain boundaries. The significant fractions of HAGBs, ranging from 86% to over 90% in samples where cracks are prominent (e.g., HT-05, HT-55, HT-105, HT-155), are consistent with the known susceptibility of austenitic steels to LME, where preferential wetting of high-energy grain boundaries by liquid zinc facilitates crack initiation and propagation. The extensive and tortuous crack path in HT-155 (653.2 μm long, 39.2 μm wide) suggests a potentially severe LME phenomenon at this hold time.

In stark contrast, the HT-205 sample (Panel (g) of Figure 4.16) shows no visible cracks, despite possessing a HAGB fraction comparable to previous samples (approximately 81%). This suggests a significant mitigation of LME at 205 ms hold time. The HT-255 sample is excluded from the study due to a large fraction of unindexed regions, indicative of either poor sample preparation or significant microstructural complexity hindering reliable EBSD analysis. This highlights the critical importance of meticulous sample preparation for accurate EBSD data. For HT-305 (Panel (h)), a crack is present, although it appears very thin after data cleaning. The presence of a notable Fe-Zn phase, if confirmed and not due to misindexation, would strongly support the presence of severe LME due to zinc penetration. The SEM image (Figure 4.17) for HT-305 aids in identifying the crack location, emphasizing the utility of correlative microscopy. The HT-355 sample (Panel (i) of Figure 4.16) also exhibits substantial unindexed regions and a reduced HAGB fraction (67.6%), but notably, no cracks are present. This reduction in HAGBs, coupled with crack absence, may suggest a further mitigation of LME at longer hold times.

The quantitative analysis of grain size, including overall average, major axis, and minor axis grain sizes, along with their standard deviations (Tables 4.3, 4.4, and 4.5; Figures 4.20, 4.21, 4.22, and their normalized counterparts), reveals a complex, non-linear evolution with hold time. A striking feature is that all samples have an average grain size larger than the base material, with the exception of the HT-155 sample. A decrease in all grain size parameters is observed from HT-05 to HT-155, would indicate grain refinement taking place at this treatment. However, these average grain sizes are larger than the average grain size of the base material, and the standard deviations are also too high to comprehensively state that this is indeed a grain refinement taking place between HT-05 and HT-155. The grain size values increase again for samples HT-205, HT-305 and HT-355. The reduction in standard deviation at HT-155 suggests a more homogeneous and finer microstructure.

These refined grain sizes observed in the HT-155 sample can be attributed to the analysed area being located at the periphery of the shoulder region. For future research, additional scans should be conducted with attention to both the interface and shoulder regions for further comparability. This analysis should be performed even if cracks are not present in those areas, to serve as a baseline. Such an approach would allow for a clearer understanding of the evolution of grain size changes, as the current variations in scanned locations across different samples make direct comparisons difficult.

5.4. Potential underlying processes and causes

The fore mentioned results point to hold time having a significant influence on the LME susceptibility of the material, thereby affecting crack quantity, size, and distance from the centreline along with surface zinc presence.

The observed differences in crack location can primarily be attributed to the water-cooling system of the electrode. As demonstrated in Section 4.2.2 and Figure 4.12, increasing hold time correlates with an increased average crack distance from the sample centreline. Furthermore, the zinc accumulation on the sample shoulders with hold times above 155 ms without cracks in the electrode-interface region are in line with Sections 4.2.2 and 4.4. This can be directly linked to the electrode's cooling effect. Piott et al. [47] show that RSW heat transfer in aluminium is dominated by conduction to water-cooled electrodes, exhibiting a high heat transfer coefficient approximately 2000 times higher than that of the ambient air, as shown in Figure 5.1. These results can be generalized to TWIP steels, despite that aluminium is a better heat conductor than austenitic steels.

Consequently, while some heat dissipation occurs to the surrounding air, its contribution is minor compared to the substantial cooling effect by the electrodes. Furthermore, their study establishes that the thermal contact conductance between electrodes and sheets can be considered ideal. The heat dissipation paths, as suggested by by Piott et al. [47], include:

Conduction within the material ($\mathbf{Q}_Q$) The heat generated by the Joule heating is conducting through the base material.

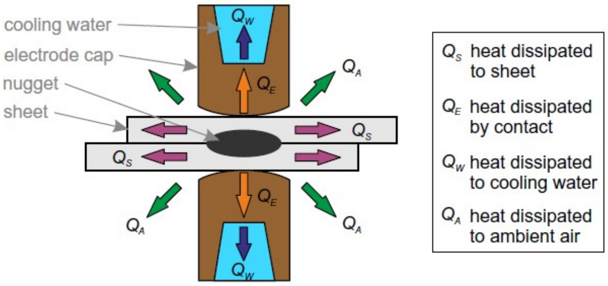

Figure 5.1. Different heat dissipation paths during RSW [47]

Conduction to the electrodes (Q_E) and Forced Convection (Water-cooling of the electrodes) (Q_W) The most significant heat transfer pathway, where efficient conduction occurs across the hot sheet-cold electrode interface under ideal thermal contact. The forced convection due to the water-cooling is a critical mechanism for maintaining electrode temperature and a main heat dissipation path from the weld zone. Numerical sensitivity analyses confirm its substantial influence on both electrode and sheet temperatures.

Natural Convection and Thermal Radiation (Q_A) A minor contributor, typically accounting for only 13-25% of overall heat dissipation.

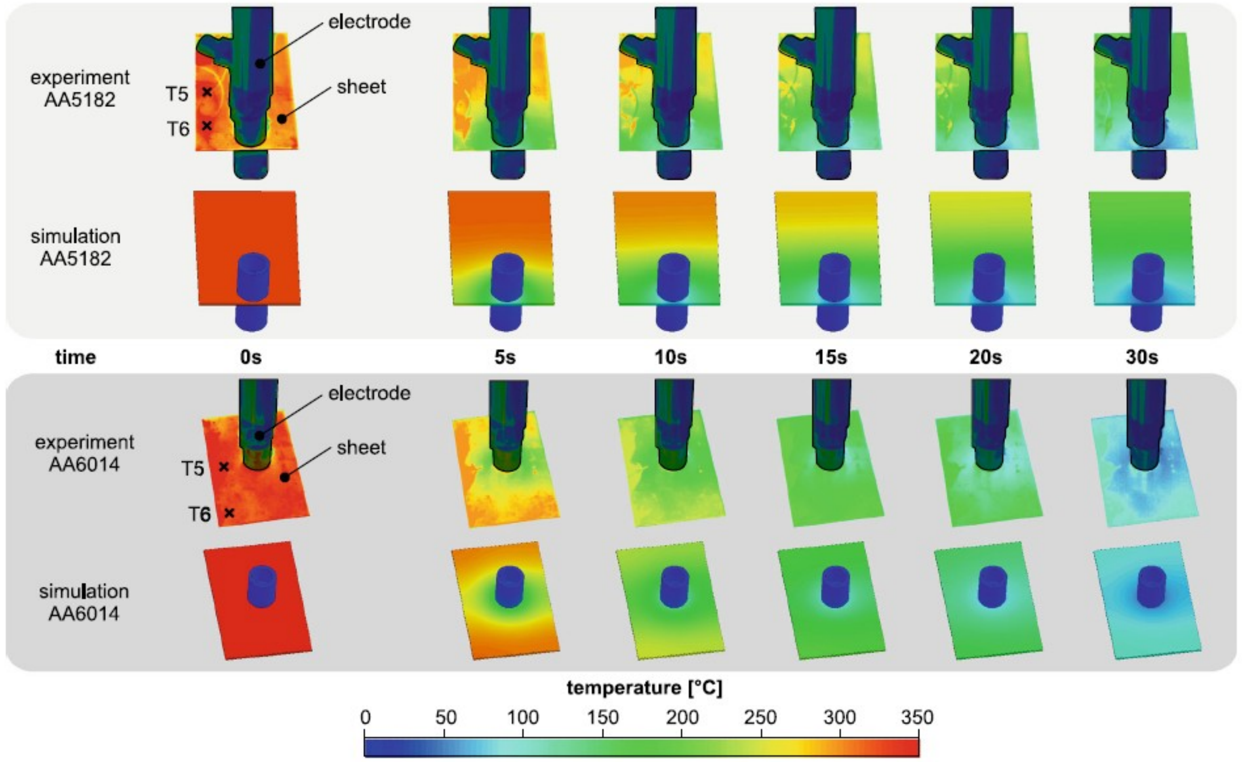

Figure 5.2. Simulated and experimental outcomes[47]

Figure 5.2 further illustrates the cooling evolution of the base material. The core finding of Piott et al. [47]'s work is that the majority of heat generated during RSW is dissipated through the water-cooled electrodes, providing an efficient and important mechanism for temperature control.

Applying these findings suggests that the water-cooled electrodes are responsible for the solidification of zinc on the sample surface. For shorter hold times, the limited contact duration with the electrode allows the liquid zinc to flow more extensively towards the inner regions of the electrode-sample interface, as heat dissipation is less efficient due to ambient air exposure. Conversely, longer hold times result in major zinc deposits on the shoulders. This is attributable to the electrode physically pushing the liquid zinc towards the shoulders, simultaneously blocking its flow towards the interface area, and facilitating its solidification through enhanced heat dissipation to the water-cooled electrodes. The zinc build-up on the shoulders could explain the crack size differences observed in Section 4.2.2 and Figure 4.10. Given that all samples originate from the same steel sheet and thus had comparable initial zinc coating thickness, the total zinc available for LME is constant across samples. As established in Section 2.4.1, zinc availability significantly influences LME in TWIP steels. The electrode-induced zinc accumulation on the shoulders at longer hold times leads to a localised increase in zinc availability, resulting in deeper cracks in these regions compared to samples with shorter hold times, where zinc is more evenly distributed across the surface. The broader distribution at lower hold times simultaneously explains the higher number of cracks observed in Figure 4.11, albeit with lower individual zinc availability per crack, leading to smaller crack dimensions.

The increased cooling rate, a direct consequence of the electrode's presence, also plays a role in these phenomena. According to Eftekharimilani et al. [48], in a RSW process with a 200 ms hold time, the cooling time to the solidification temperature of zinc (693 K) is approximately 180 ms (estimated from Figure 5.3). Longer hold times, due to the cooling effect of the electrodes, likely shorten the cooling duration, thereby increasing the estimated cooling rate of 6150 K/s. The subsequent accelerated cooling reduces the time available for liquid zinc to migrate towards susceptible electron-interface regions before solidification, effectively preventing it from fuelling LME cracking in the interface region.

It's crucial to acknowledge that the findings from Eftekharimilani et al. are derived from a simulation, not direct measurements as the latter are hard to initiate, and may therefore differ from experimental reality. Nevertheless, the simulation provides a plausible explanation for the observed differences in crack locations. Specifically, the result indicates that zinc solidifies approximately 180 ms after the current is stopped. This timing explains why samples with hold times below 180 ms present cracks in the interface region, as some zinc might be still in liquid form that can flow toward this area. With the increased hold time, the amount of still liquid zinc decreases, hence it can flow shorter distances towards the interface region. Thus the increasing average distance of cracks from the centreline of the sample. In contrast, for hold times above 180 ms, zinc fully solidifies on the shoulders, which would account for cracks being found in these locations instead.

Rathod et al.[49] use finite element modelling to investigate the effects of welding parameters on the thermal and stress evolution of a DP steel grade and an austenitic stainless steel grade. According to their research, temperature changes during the welding process are influenced by the density, specific heat and the thermal conductivity of the material, along with internal heat generation. They find that material properties are in fact temperature dependent, making it difficult to model RSW accurately, due to the significant changes in temperature [49]. They emphasize the importance of optimal heat control, as excessive heat can cause reduced weld strength along with a deterioration in welding quality. Higher currents result in higher temperature and better fusion, however, above the optimum heat, expulsion can form. Weld time also increases weld strength, while decreasing the strength value above a certain amount of cycles due to the softening of the HAZ [49]. The role of heat dissipation is also discussed: excess heat usually radiates either to the base metal or it is released into the atmosphere [49]. Figure 5.4 shows the temperature distribution in the sample and the electrode during the welding process. The immediate surrounding of the electrode shows temperatures that are higher than the melting point of Zn.

Rathod et al. [49] also find that a compressive stress is present during the welding process, especially between the faying sheets. The compressive stress ultimately leads to a sufficient metallurgical structure of the welded joint with an ideal strength. They conclude that this phenomena is driven by the applied electrode pressure, along with the thermal expansion [49]. That is, higher shear strengths can be achieved by an optimal

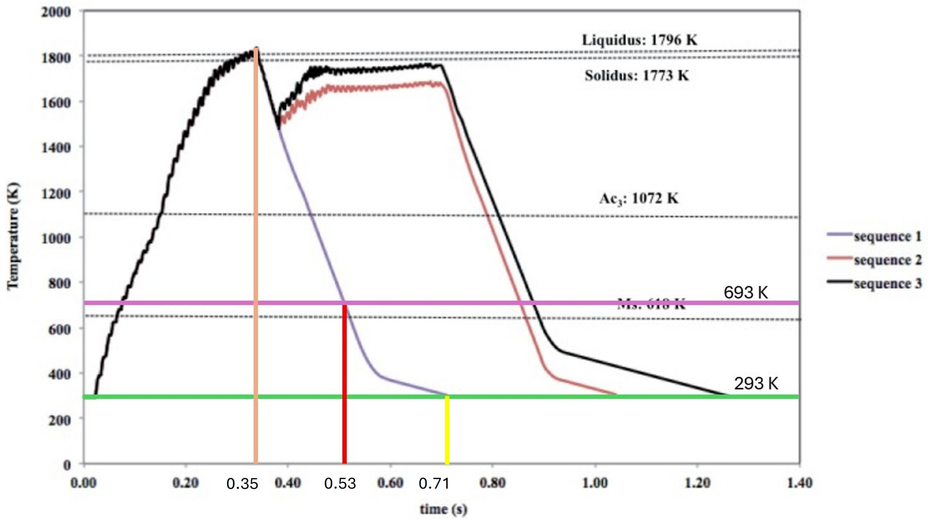

Figure 5.3. Simulated thermal history of the primary weld edge for different welds, with sequence 1 showing that of the single pass RSW weld [48]

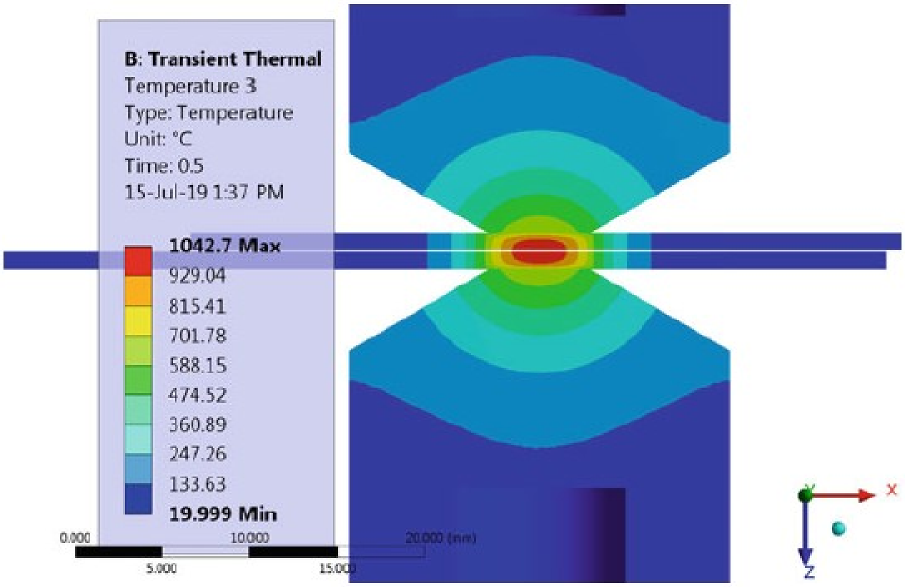

Figure 5.4. Finite element model of the temperature states during the RSW process of DP steel [49]

welding current and time, as the optimal value of these parameters leads to a favourable stress state within the weldment. This stress state results in a good metallurgical structure, avoiding formation of voids, while also condensing the weld nugget, resulting in a more compact weld. However, the application of excessive time or current can lead to the softening of the HAZ and other unfavourable microstructural changes. This can impact the stress-carrying capacity of the joint [49]. In addition, electrode pressure is also important, as up to a certain point shear strength concurrently increases with electrode pressure. On the other hand, lower electrode pressure reduces the resistance, which also affects the heat generation and stress [49]. Figure5.5 presents the stress states in the sample during the welding process, which showcases an Equivalent (Von Mises) stress subjected on the sample. Notably, that the maximum stress is located in the weld nugget, with

750.49 MPa, while there is a drop in stress values in the shoulder regions: stresses present decrease from 499.55-583.2 MPa to just 415.9 MPa, followed by an increase to the initial range of 499.55-583.2 MPa. This pattern suggests that there is a unique stress relation in the shoulder regions of the samples.

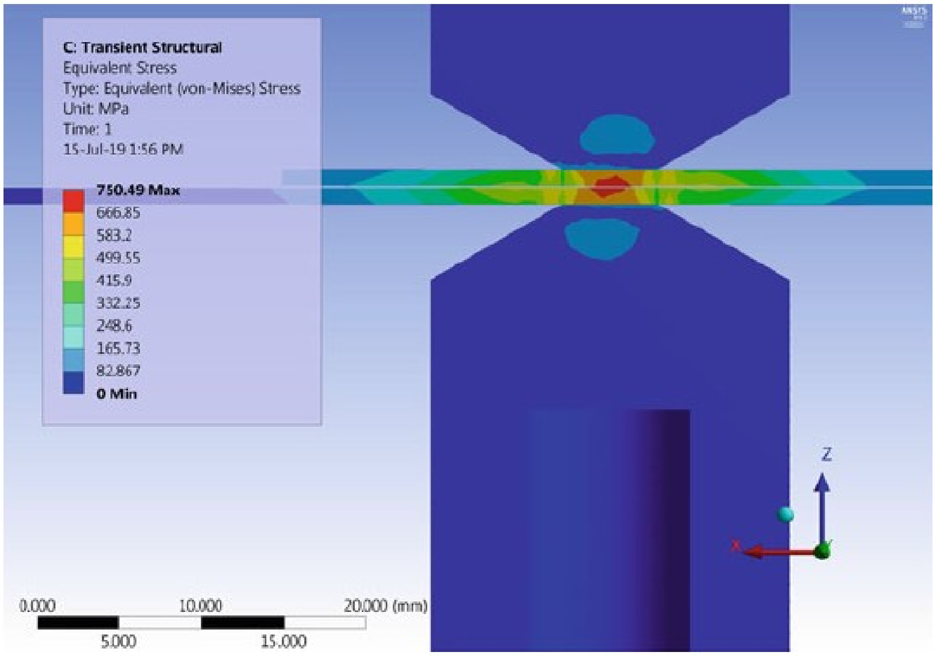

Figure 5.5. Finite element model of stress states during the RSW process of DP steel [49]

Another effect of the electrode-driven increased cooling rate is the microstructural differences seen in Figure 4.19 in Section 7.6 and the figures in Section 5.3. A clear pattern of grain coarsening can be seen for both the interface region and the shoulder samples when compared with the base material. With increasing the hold time, there is a decrease of average grain size present for the samples respectively, however as already mentioned the standard deviation is so large that these decreases should not be accounted for as refinement. Jang et al. [50] show that higher cooling rates generally result in a finer grain structure. This suggests a direct connection between the microstructure becoming finer and hold time length. This connection is important, as microstructures with finer grains have a larger amount of grain boundaries, which mitigates LME formation and propagation. However, it is noteworthy that the high fraction of high angle grain boundaries in the microstructure of mainly austenitic TWIP samples is very susceptible to LME according to Section 2.4.1. Thus, this finer microstructure in the interface zone when compared to the shoulder zone most likely plays a part in the forming cracks being generally smaller than those located in the shoulders, where grains tend to be larger. Notably, the coarsening process of grains happens with the same ratio for both the whole grain, the major and the minor axes, as shown in the figures of Section 5.3. This implies that the grains retain their shapes following their growth.

An additional force driving LME in the samples is the role of stresses and their impact on the mechanical behaviour and LME susceptibility. This section investigates how welding parameters alter these stresses. To discuss this possibility, the effect of zinc on the mechanical properties of steel must first be established. Ling et al. [51] investigate the influence of zinc and the consequent LME effects on the mechanical properties of steel. Their findings indicate a significant reduction in the overall strength and ductility of the material after the RSW process. This reduction manifests as lower tensile shear strength and/or premature failure of the welded joint under mechanical loading. The decreased overall strain capacity of galvanized materials compared to their non-galvanized counterparts, along with energy reductions within the critical LME susceptible temperature range, are illustrated in Figure 5.6. Beal [5] report similar results regarding the relationship between mechanical properties and the presence of zinc, specifically a reduction in strength and ductility, as depicted in Figure 5.7. However, this Figure depicts Gleeble test results which testing method is generally more homogeneous than real-life RSW processes, meaning that the latter is less predictable and could showcase even more dramatic changes due to the presence of liquid Zn.

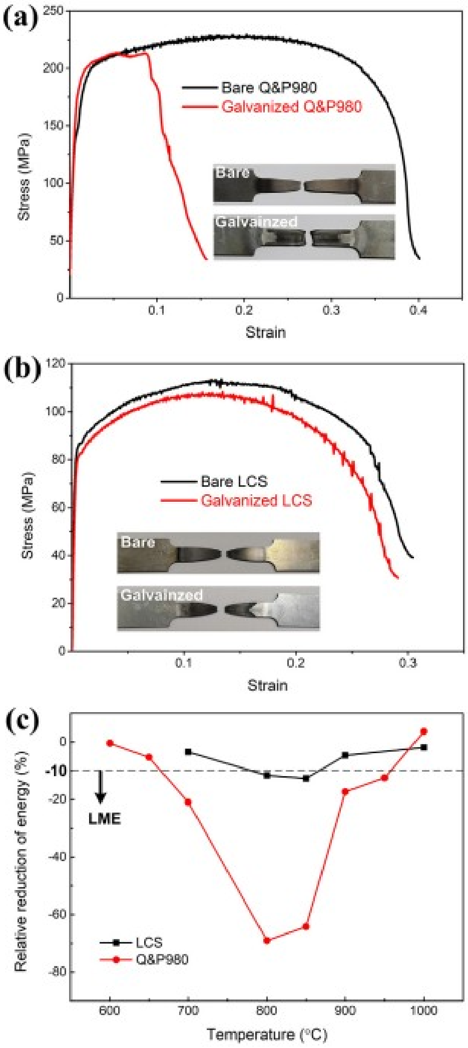

Figure 5.6. Tensile curves of (a) bare and galvanized Q&P980, (b) bare and galvanized LCS at 800 °C, and (c) relative reduction of energy at different temperatures [51]

Furthermore, Beal et al. [6], specifically focus on zinc-induced LME in high-manganese content TWIP steels, and identify a ductility trough, representing a temperature range where severe embrittlement is prominent.

This reduction effect is further exacerbated by the presence of residual stresses, as Bai et al. [52] indicate that LME is sensitive to the residual stresses present in the material. During the cooling process, the shrinkage of the material leads to the development of internal tensile stresses, which can facilitate the formation of LME micro-cracks. They argue that residual stresses reduce tensile strength of materials with a high yield point more, compared to their low yield point counterparts [52]. The question then arises whether, and if so, how do welding parameters affect residual stresses. Rihan et al. [53] study these questions, using

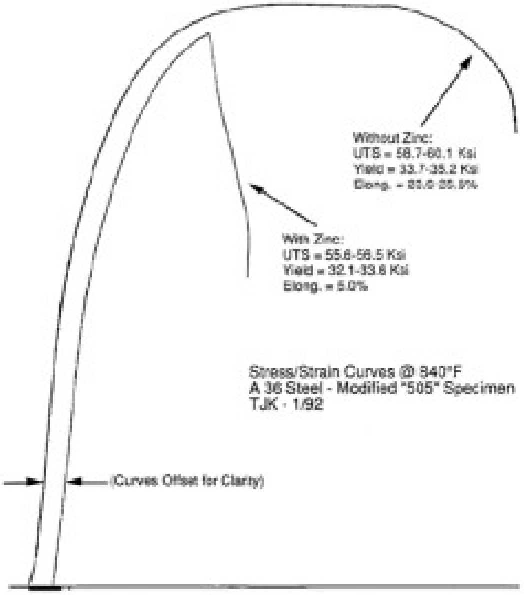

Figure 5.7. Stress-strain curves of A36 steel grade: galvanized versus non-galvanized material [5]

a simplified computational model to predict stresses and critical nugget size. Their model reveals that an increase in both weld time and weld current consistently decrease residual stresses, primarily due to a more gradual temperature gradient after welding. Increasing the electrode force yields similar outcomes, leading to smaller residual stresses (from over 300 MPa to around 200 MPa, around 30% decrease), mainly because the electrode force yield compressive stresses on the sample surface, thereby reducing it's tensile residual stress [53]. Cha et al. [54] also evaluate the impact of welding parameters on residual stresses in 304 type austenitic stainless steel. Their main finding is that increasing weld current, weld time, and electrode force, all lead to a reduction in residual stresses within the microstructure, in line with the results of Rihan et al. [52]. The underlying reason identified is the creation of a lower temperature gradient through material thickness during the application of a higher heat input during RSW, minimizing thermal strain and stress concentration throughout the microstructure [54].

Such findings directly relate to the LME behaviour of the TWIP steel grade investigated in this thesis. Firstly, prolonged application of compressive stresses via the electrode force, commonly occurring with a longer hold time, generally reduces residual stresses in the electrode-interface region. This, however, is not the case in the shoulder region, where the compressive forces from the electrodes are less effective. Eftekharimilani et al. [55] simulate residual stress values in their research. The simulation results show that in the weld centre, stresses reach up to 450 MPa, with the highest value of 500 MPa being at the weld edge. They claim that the residual stresses in the electrode-sample interface can also be approximately 500 MPa. This distinction is crucial when considering that the increased cooling rate due to the water-cooling system of the electrodes promoting cooling of the sample, both during the hold time and in later stages. Consequently, this high cooling rate, coupled with the reduced effect of compressive forces in the shoulder region, could contribute to the formation of fewer but larger LME cracks in samples with a longer hold time. Conversely, in the electrode-interface region, the presence of compressive forces and the sharp cooling rate somewhat counteract one another, resulting in LME, but with cracks of smaller size for samples with shorter hold times.

These findings suggest that altering the hold time during RSW plays an equally significant role in mitigating LME as other welding parameters. Ideally, a longer hold time would be preferred to achieve a higher cooling rate, which could prevent liquid zinc from flowing into the electrode-interface region by solidifying it completely. This would, in turn, limit large-scale zinc contamination and reduce the area susceptible to LME cracks. However, as observed in samples with the longest hold times, this exacerbates LME cracking on the shoulders, as the entire sample's zinc pool accumulates and solidifies at these locations. Figures 4.10 and 4.11 illustrate the contrasting outcomes: either a larger number of overall smaller cracks spread over a wider area, or fewer but larger cracks concentrate specifically in the shoulder region. Nevertheless, this increased cooling rate also results in a steeper temperature gradient that promotes LME due to non-uniform thermal expansion. The observed increase in grain size across all hold times relative to the base material, particularly in samples with hold times exceeding 205 ms, can be attributed to recrystallization. In both the interface and shoulder regions the steel undergoes recrystallization, however, the resulting grain growth differs due to variations in cooling rates. The interface region, being in direct contact with the water-cooled electrode, experiences a faster cooling rate, restricting significant grain coarsening. Conversely, in the shoulder region, the electrode has less contact, making heat dissipation through the electrode less dominant. Here, heat is primarily dissipated into the ambient air, resulting in a slower cooling rate that provides more time for grain growth.

In summary, the primary reason for the difference in grain sizes between the interface and shoulder samples is their location-dependent cooling rates. The reduced effect of electrode cooling in the shoulder region leads to slower heat dissipation, and consequently, larger grain sizes compared to the interface. It is important to note that the compressive stresses from the electrode are applied to the sample for a longer duration with increased hold time, further reducing residual stresses in the interface region compared to shorter hold times. This should ultimately reduce the overall stresses present in the samples, thereby mitigating LME in this region. However, these compressive stresses have a diminished effect on the shoulder region, leaving it having a different stress-state than of the interface zone. Overall, the properties of the exact stress-state of the shoulders remain unknown to us. Summarily, the complex relationship between hold time and LME can be summarized in four key points:

1) Shorter hold times lead to greater flow of liquid zinc towards the inner regions of the electrode-sample interface due the zinc not solidifying completely, resulting in a larger number of smaller cracks distributed across a wider surface area.
2) Longer hold times cause zinc to accumulate and solidify on the shoulders of the samples due to the physical blocking and cooling effect of the electrode. This leads to fewer but larger LME cracks specifically in the shoulder regions.
3) A grain coarsening is seen when compared to the base material. While there is no clear physical explanation to why this is happening, the austenitic microstructure of TWIP steels, characterized by a high-fraction of HAGBs, is susceptible to LME. According to relevant studies, the increased cooling rate stemming from water-cooled electrodes should lead to a finer microstructure, that would mitigate LME by strain partitioning along the increased number of grain boundaries.
4) Longer hold times, by applying compressive stresses through the electrode force for an extended duration, can reduce residual stresses in the interface region (approximately 30% reduction), thereby mitigating LME in that area. However, this effect is different in the shoulder region, which might contributing to the formation of the larger cracks seen.

The primary challenge in definitively identifying the directional impact of hold time on LME lies in the fact that the observable results are the joint outcome of concurrent interdependent or potentially offsetting effects. Consequently, some aspects, such as a finer microstructure, could simultaneously mitigate *and* propagate LME.

Despite this complexity, it appears that either a very long hold time, such as 355 ms, or a more moderate, medium-length hold time, ranging from 155-205 ms, should be employed in practice. While a 355 ms hold time would significantly hinder production, notably increasing the welding production time and cost of vehicles, it effectively eliminates LME cracks. As an illustrative example, if a chassis has 5000 welded joints produced at 155-205 ms hold times, increasing the latter would lead to approximately 30 minutes of production time increase per vehicle. Conversely, excessively short hold times (5ms, 55 ms, 105 ms) result in an increased number of cracks, which is undesirable due to the proliferation of potential failure locations. Longer hold times, such as 255 ms and 305 ms, while leading to production time increases comparable to the 155 ms value, still result in large-sized shoulder cracks. Hold times within the 155-205 ms range either present a reduced quantity of cracks (present in both the interface and shoulder regions) that are somewhat smaller than in other cases, or result in no cracks at all. However, there is no physical reason that would explain why the 155 ms sample has such a fine microstructure, and why the 205 ms sample has no cracks, as it is not particularly fine grained, nor does it have lower fcc or HAGB fractions. Therefore, manufacturers face a trade-off between accepting the possibility of LME cracks, albeit at a reduced rate and size, while maintaining vehicle productivity; or implementing a safer, yet considerably costlier hold time that eliminates LME cracks at the expense of significantly diminishing production capabilities when considering large-scale vehicle manufacturing.

To provide a more comprehensive and definitively optimal hold time value for LME mitigation, further research is imperative. This future research should ideally incorporate simulations and modelling (FEA, temperature, stress) of the welding process and to understand phenomena at both microstructural and macrostructural scales. Additionally, a more extensive analysis of a larger sample set is necessary to establish robust trends. This includes performing EBSD evaluations at consistent locations across an increased amount of samples, to determine if trends are present at those locations. To ensure the comparability of results, it is crucial to apply more careful sample preparation protocols, including a reproducible cutting method and a standardized sequence for sanding and polishing to consistently achieve the same thickness of material. Additionally, mechanical tests on the samples, and temperature measurements during the welding process are required to enable the isolated assessment of each individual effect, allowing their respective roles to be disentangled, rather than appearing as a joint impact.

6. Conclusion

This thesis investigates the multifaceted influence of hold time during resistance spot welding (RSW) on liquid metal embrittlement (LME) susceptibility of a zinc-coated TWIP steel grade. The analysis of existing literature and evaluation of experimental results indicate that hold time is a critical process parameter, process parameter, having an important but not yet clearly understood effect on LME behaviour.

Starting with the optical microscopy evaluation, the main crack locations are identified. For the double sheet samples, where two layers of TWIP steels were welded together, no cracks were found. The triple sheet samples where a TWIP and two DX54 sheets were welded together. These samples were further evaluated by two types of SEM microscopes, to analyse the cracks and other phenomena on a deeper scale. EDS was used to evaluate the chemical composition of the cracks. This analysis verified that the cracks are LME induced, due to the presence of zinc in them, and also demonstrated that a notable zinc build-up is present on the shoulders of the samples with a longer hold time. To identify the orientation of the grains, EBSD scans were used. The EBSD scans also revealed that the microstructure of the samples is mainly austenitic with a dominantly high angle grain boundary fraction, which observation indicates the susceptibility to LME in all cases due to these factors. Next, these scans were used to evaluate the average grain size by average grain size graphs, that reveals an overall grain coarsening at both the electrode-sample interface and the shoulder regions when compared to the base material. It is noteworthy that the grain coarsening process is observed to be isotropic, maintaining the original shape of the grains.

The primary finding of this thesis is that hold time has a prominent impact on the location and characteristics of LME-induced cracks: Samples with a shorter hold times (up to 155 ms) value generally exhibit a larger number of cracks, predominantly in the electrode-interface region. Conversely, longer hold times (from 205 ms upwards) lead to fewer but deeper cracks that were concentrated on the sample shoulders, or no cracks at all. There is also an evolution of the average distance of cracks from the centreline of each sample: With the hold time increasing, the average distance also increases with it, however, these data might be affected by the differences in the cross section locations. These distinct findings are attributed mainly to the dominant heat dissipation path towards the water-cooled electrodes during hold time, and the flow dynamics of liquid zinc. The water-cooled electrodes represent a far more efficient heat dissipation path than the ambient air. With an increase in hold time, the prolonged contact with the water-cooled electrodes results in a complete solidification of liquid zinc in both the electrode-interface and shoulder regions. This effectively constrains the migration of zinc towards the central weld nugget, promoting its solidification on the shoulders where zinc has already been accumulated due to the electrode pushing its liquid form there. This localized zinc accumulation on the shoulders in turn, leads to a higher local concentration of zinc, which results in the formation and propagation of larger, albeit fewer cracks on the shoulders. At longer hold times, the electrode also blocks the flow of zinc towards the inner parts of the interface region. For shorter hold times, the reduced contact time allows for a more even distribution of liquid zinc across a wider surface area before solidification, leading to a larger number of smaller cracks where zinc is less concentrated per crack site.

Microstructural evolution under varying hold times emerged as another important factor influencing the material's LME susceptibility. As previously mentioned, a clear pattern of grain coarsening was observed in both the interface and shoulder regions, despite the literature establishing that a higher cooling rate typically results in a finer grain structure. While a finer microstructure with its increased grain boundary area is generally understood to mitigate LME propagation due to strain partitioning, the high fraction of high-angle grain boundaries characteristic of austenitic TWIP steel renders it inherently susceptible. Thus the finer grain structure in the interface zone compared to the shoulder regions likely contributes to the slightly smaller cracks observed in that region, most likely due to the more difficult crack propagation paths compared to the coarser grains found in the shoulder regions of the samples.

The role of stresses and their interaction with welding parameters was also studied. Compressive stresses are inherently present during the RSW process due to the electrode force and pressure, along with thermal expansion. This analysis, aligned with existing literature, suggests that longer hold times, through prolonged application of electrode pressure, lead to a reduction of tensile stresses in the electrode-interface region. This localized reduction in tensile stresses, combined with the sharp cooling rate from the electrodes, appear to create a complex stress state that allows LME to occur, but potentially limits the maximum crack size in the interface region. In contrast to the interface regions, the shoulders experience less direct compressive forces, and therefore are more susceptible to tensile stresses. These stresses combined with the localized high zinc availability at longer hold times facilitate the formation of larger cracks. This interplay highlights the complicated relationship between thermal gradients, mechanical forces and LME susceptibility.

These findings enhance current understanding of the subject in two ways. Manufacturers face a trade-off: either opt for an extended hold time (approximately 355 ms), which effectively eliminates LME cracks but adds a substantial 30 minutes to the welding production time per vehicle when counting with 5000 spot welds, or choose a hold time between 155-205 ms. The latter represents a practically optimal duration, as it either results in fewer and smaller cracks (across both the interface and shoulder regions) or no cracks. Shorter hold times such as 5-105 ms appear to lead to an unacceptably high number of smaller cracks, increasing potential failure points. While hold times between 255 and 305 ms also significantly increase production time, and still result in large shoulder cracks. Ultimately, practical implementation requires balancing LME crack reduction with production efficiency. However, no physical explanation was found whether why the 155 ms and 205 ms hold dime values are so favourable for LME mitigation.

The analysis identifies several promising paths for future research. A more detailed quantitative correlation between the average grain size in different weld regions and the LME crack dimensions is needed, as it would offer valuable insights. Computational modelling and simulations, for example FEA would shed light on this correlation, by including the temperature-dependent material properties, precise heat transfer coefficients, and the dynamic stress evolution throughout the entire RSW cycle. This would enable a more detailed understanding of the underlying mechanisms, with a chance to evaluate how each of these provided properties and coefficients affect the process. Finally, these approaches could be used to disentangle the complex influence of microstructure fineness on LME susceptibility.

Acknowledgments

I would like to thank everyone who helped me during my master's studies, especially during my thesis project:

First and foremost, I would like to thank my supervisors, Dr.ir. MJM Hermans, and Gautham Mahadevan. Their constant availability and willingness to help is very much appreciated, and their flexibility during the planning of measurements and meetings has been invaluable. They were always available for questions and suggestions, and regularly directed me toward the right path when new questions arose. Thank you also for the countless occasions when I just happened to step into your offices without an appointment to ask immediate questions and always received answers.

I would like to thank Dr. Ing. Yan Ma for his interest and availability to be part of the thesis committee. Without him, I would not have been able to defend my thesis this summer.

I would like to thank Dr. Yaiza Gonzalez Garcia, Prof.Dr.ir. JMC Mol, and Can Özkan for their support throughout previous research projects and for always having a moment to chat about university and everyday topics.

I would also like to thank DP Sharma Mainali, Agnieszka Kooijman, and Richard Huizenga for their assistance during laboratory and data evaluation work and for their availability. Without them, these tasks would have taken much longer.

I would like to thank my friends, who were there for me throughout the two years, with whom I could always speak, share progress or difficulties alike, and who always found a way to make even the hardest days better. I thank them for the infinite discussions we had, most of which turned into joking around after a while, which all of us needed at that moment. Köszönöm Búlcsú, Csili, Dani, Józsi, Kokó, Pali, Vili, Zsombi. Dziękuję Paweł. Obrigado Elvis. I wrote your names in alphabetical order so nobody gets upset about the order :D

I would like to thank everyone present in our online sports community for the discussions, debates, and collective match-watching, as it helped me release pressure during my everyday life.

Last but certainly not least, I would like to thank my family. I would like to thank my Mother and my Sister for staying strong during their illnesses and treatments, while always whispering in my ear that I should not focus on them but on my studies. Luckily I managed to do both. Consequently, I would like to thank my Father and my Brother-in-law for taking care of them as much as they did. I need to thank all of them for pushing me throughout the two years, even though I was sometimes a bit frustrated by it, and for helping me whenever I needed it with decisions and obstacles. I also have to thank my dog Lizi, who managed to be the happiest every time I was home, even though everyone else was happy too. I would also like to thank every other broader family member and friend for looking out for us.

References

[1] N. Baluch, Z. Udin, and C S Abdullah. Advanced high strength steel in auto industry: an overview. *Eng. Technol. Appl. Sci. Res.*, 4:686–689, 08 2014. doi: 10.48084/etasr.444.

[2] T.B. Hilditch, T. de Souza, and P.D. Hodgson. 2 - properties and automotive applications of advanced high-strength steels (ahss). In M. Shome and M. Tumuluru, editors, *Welding and Joining of Advanced High Strength Steels (AHSS)*, pages 9–28. Woodhead Publishing, 2015. ISBN 978-0-85709-436-0. doi: https://doi.org/10.1016/B978-0-85709-436-0.00002-3. URL `https://www.sciencedirect.com/science/article/pii/B9780857094360000023`.

[3] E. Spišák, L. Kascak, and J. Viňáš. Application of resistance spot welding in car body production. *Acta Mechanica Slovaca*, 19:28–34, 10 2015. doi: 10.21496/ams.2015.012.

[4] Y. Ikeda, R. Yuan, A. Chakraborty, H. Ghassemi-Armaki, J.M. Zuo, and R. Maaß. Early stages of liquid-metal embrittlement in an advanced high-strength steel. *Materials Today Advances*, 13:100196, 2022. ISSN 2590-0498. doi: https://doi.org/10.1016/j.mtadv.2021.100196. URL `https://www.sciencedirect.com/science/article/pii/S2590049821000667`.

[5] Coline Beal. Mechanical behaviour of a new automotive high manganese twip steel in the presence of liquid zinc. 03 2011.

[6] Coline Beal, Xavier Kleber, Damien Fabregue, and Mohamed Bouzekri. Liquid zinc embrittlement of twinning-induced plasticity steel. *Scripta Materialia*, 66(12):1030–1033, 2012. ISSN 1359-6462. doi: https://doi.org/10.1016/j.scriptamat.2011.12.040. URL `https://www.sciencedirect.com/science/article/pii/S1359646211007883`. Viewpoint Set no. 50: Twinning Induced PlasticitySteels.

[7] K. Weman. *Welding Processes Handbook*. Woodhead Publishing Series in Welding and Other Joining Technologies. Woodhead Publishing, 2011. ISBN 9780857095183. URL `https://books.google.hu/books?id=oaNgAgAAQBAJ`.

[8] T. Das. *Resistance Spot Welding: Principles and Its Applications*. IntechOpen, 06 2022. ISBN 978-1-80355-384-9. doi: 10.5772/intechopen.103174.

[9] Gao H. Huizenga R. van der Aa EM. Amirthalingam M. Richardson I. Hermans M. Eftekharimilani, P. Residual stress measurements and model validation of single and double pulse resistance spot welded advanced high strength steel. *Mathematical Modelling of Weld Phenomena 12*, 2018. doi: DOI10.3217/978-3-85125-615-4-22.

[10] B. Gawai and C.M. Sedani. Optimization of process parameters for resistance spot welding process of hr e-34 using response surface method -a review. 05 2019. doi: 10.13140/RG.2.2.31190.09283.

[11] Phillips D. H. Kimchi, M. *Resistance Spot Welding Process Physics and Fundamentals*. Springer International Publishing, Cham, 2023. ISBN 978-3-031-25783-4. doi: 10.1007/978-3-031-25783-4_2. URL `https://doi.org/10.1007/978-3-031-25783-4_2`.

[12] E. Hamid, H. Mohsen, and H. Ayob. New parametric study of nugget size in resistance spot welding process using finite element method. *Materials Design*, 31(1):149–157, 2010. ISSN 0261-3069. doi: https://doi.org/10.1016/j.matdes.2009.06.042. URL `https://www.sciencedirect.com/science/article/pii/S0261306909003343`.

[13] Z. Yu-Jun, X. Lang, S. Yan, Diana M. W., Amberlee S. H., L. Yong-Bing, and E. C. Blair. Online measurement of weld penetration in robotic resistance spot welding using electrode displacement signals. *Measurement*, 168:108397, 2021. ISSN 0263-2241. doi: https://doi.org/10.1016/j.measurement.2020.108397. URL `https://www.sciencedirect.com/science/article/pii/S0263224120309325`.

[14] Taiwo Abioye, Anas Norazman, M. Irfan, A. Anasyida, and Hussain Zuhailawati. Parametric optimization for resistance spot-welded thin-sheet aluminium alloy 5052-h32. *Arabian Journal for Science and Engineering*, 44, 04 2019. doi: 10.1007/s13369-019-03869-9.

[15] X. Wu. *6 - Advanced high-strength steel tailor welded blanks (AHSS-TWBs)*. Woodhead Publishing Series in Welding and Other Joining Technologies. Woodhead Publishing, 2011. ISBN 978-1-84569-704-4. doi: https://doi.org/10.1533/9780857093851.2.118. URL `https://www.sciencedirect.com/science/article/pii/B978184569704450006X`.

[16] O. Bouaziz, S. Allain, C.P. Scott, P. Cugy, and D. Barbier. High manganese austenitic twinning induced plasticity steels: A review of the microstructure properties relationships. *Current Opinion in Solid State and Materials Science*, 15(4):141–168, 2011. ISSN 1359-0286. doi: https://doi.org/10.1016/j.cossms.2011.04.002. URL `https://www.sciencedirect.com/science/article/pii/S1359028611000179`.

[17] W. Bleck. New insights into the properties of high-manganese steel. *International Journal of Minerals, Metallurgy and Materials*, 28:782–796, 05 2021. doi: 10.1007/s12613-020-2166-1.

[18] J.; Kim J.-S.; Jeon J. B.; Kim S. K.; Chang Y. W. Jung, J. E.; Park. Temperature effect on twin formation kinetics and deformation behavior of fe-18mn-0.6c twip steel. *Metals and Materials International*, 20:27–34, 2014. ISSN 2005-4149. doi: 10.1007/s12540-014-1008-y. URL `https://doi.org/10.1007/s12540-014-1008-y`.

[19] M. D.; Miller-V. M. Norkett, J. E.; Dickey. A review of liquid metal embrittlement: Cracking open the disparate mechanisms. *Metallurgical and Materials Transactions A*, 52(6):2158–2172, 2021. ISSN 1543-1940. doi: 10.1007/s11661-021-06256-y. URL `https://doi.org/10.1007/s11661-021-06256-y`.

[20] C.F. Old. Liquid metal embrittlement of nuclear materials. *Journal of Nuclear Materials*, 92(1):2–25, 1980. ISSN 0022-3115. doi: https://doi.org/10.1016/0022-3115(80)90136-1. URL `https://www.sciencedirect.com/science/article/pii/0022311580901361`.

[21] M.H. Razmpoosh, C. DiGiovanni, Y.N. Zhou, and E. Biro. Pathway to understand liquid metal embrittlement (lme) in fe-zn couple: From fundamentals toward application. *Progress in Materials Science*, 121:100798, 2021. ISSN 0079-6425. doi: https://doi.org/10.1016/j.pmatsci.2021.100798. URL `https://www.sciencedirect.com/science/article/pii/S0079642521000220`.

[22] C. F. Old and P. Trevena. Embrittlement of zinc by liquid metals. *Metal Science*, 13(8):487–495, 1979. doi: 10.1179/030634579790438390. URL `https://doi.org/10.1179/030634579790438390`.

[23] A. Gornakova, Boris Straumal, S. Tsurekawa, L.-S Chang, and Alexey Nekrasov. Grain boundary wetting phase transformations in the zn-sn and zn-in systems. *Reviews on Advanced Materials Science, v.21, 18-26 (2009)*, 21, 09 2009.

[24] M.H. KAMDAR. Liquid metal embrittlement. In C.L. BRIANT and S.K. BANERJI, editors, *Embrittlement of Engineering Alloys*, volume 25 of *Treatise on Materials Science Technology*, pages 361–459. Elsevier, 1983. doi: https://doi.org/10.1016/B978-0-12-341825-8.50015-5. URL `https://www.sciencedirect.com/science/article/pii/B9780123418258500155`.

[25] C. DiGiovanni, A. Ghatei Kalashami, E. Biro, and N.Y. Zhou. Liquid metal embrittlement transport mechanism in the fe/zn system: Stress-assisted diffusion. *Materialia*, 18:101153, 2021. ISSN 2589-1529. doi: https://doi.org/10.1016/j.mtla.2021.101153. URL `https://www.sciencedirect.com/science/article/pii/S2589152921001563`.

[26] V. V. Dmukhovskaya, I. G.; Popovich. A phenomenological model of embrittlement of metals under conditions of the adsorption action of liquid metal media. *Soviet materials science : a transl. of Fiziko-khimicheskaya mekhanika materialov / Academy of Sciences of the Ukrainian SSR*, 18:461–467, 1983. ISSN 1573-885X. doi: 10.1007/BF00729424. URL `https://doi.org/10.1007/BF00729424`.

[27] J. Zhao, C. Ding, G. Wu, and J. Zhang. Role of aluminum on liquid metal embrittlement susceptibility for zn–al–mg/sn coated hot-formed steels. *Journal of Materials Research and Technology*, 19:747–764, 2022. ISSN 2238-7854. doi: https://doi.org/10.1016/j.jmrt.2022.05.092. URL `https://www.sciencedirect.com/science/article/pii/S2238785422007530`.

[28] J.-H. Kang, S.-H. Hong, J. Kim, and S.-J. Kim. Zn-induced liquid metal embrittlement of galvanized high-mn steel: Strain-rate dependency. *Materials Science and Engineering: A*, 793:139996, 2020. ISSN 0921-5093. doi: https://doi.org/10.1016/j.msea.2020.139996. URL `https://www.sciencedirect.com/science/article/pii/S0921509320310662`.

[29] A. Ghatei Kalashami, C. DiGiovanni, M.H. Razmpoosh, F. Goodwin, and N.Y. Zhou. The effect of silicon content on liquid-metal-embrittlement susceptibility in resistance spot welding of galvanized dual-phase steel. *Journal of Manufacturing Processes*, 57:370–379, 2020. ISSN 1526-6125. doi: https://doi.org/10.1016/j.jmapro.2020.07.008. URL `https://www.sciencedirect.com/science/article/pii/S1526612520304333`.

[30] A. Chakraborty, R. Ghosh, M. Sudan, and A. Mondal. Improvement in hot dip galvanized coating microstructure and properties by pre-metallic deposition on steel surface: A comprehensive review. *Surface and Coatings Technology*, 449:128972, 2022. ISSN 0257-8972. doi: https://doi.org/10.1016/j.surfcoat.2022.128972. URL `https://www.sciencedirect.com/science/article/pii/S0257897222008933`.

[31] Wufeng D., Hua P., Ming L., Shujuan W., Kai D., and Yulai G. Three-dimension characterization of the liquid metal embrittlement crack in the resistance spot welded joint of the advanced high strength steel. *Materials Today Communications*, 34:105322, 2023. ISSN 2352-4928. doi: https://doi.org/10.1016/j.mtcomm.2023.105322. URL `https://www.sciencedirect.com/science/article/pii/S2352492823000120`.

[32] F. E. Wang. Chapter 6 - mechanical properties. In Frederick E. Wang, editor, *Bonding Theory for Metals and*

Alloys (Second Edition), pages 157–191. Elsevier, second edition edition, 2019. ISBN 978-0-444-64201-1. doi: https://doi.org/10.1016/B978-0-444-64201-1.00006-3. URL `https://www.sciencedirect.com/science/article/pii/B9780444642011000063`.

[33] A. Lalachan, S. P. Murugan, W.-S. Jin, and Y.-D. Park. Liquid metal embrittlement in zn-coated steel resistance spot welding: Critical electrode-contact and nugget growth for stress development and cracking. *Journal of Materials Processing Technology*, 318:118009, 2023. ISSN 0924-0136. doi: https://doi.org/10.1016/j.jmatprotec.2023.118009. URL `https://www.sciencedirect.com/science/article/pii/S0924013623001541`.

[34] D. Bhattacharya. Liquid metal embrittlement during resistant spot welding of zn-coated high-strength steels. *Materials Science and Technology*, 34:1–21, 04 2018. doi: 10.1080/02670836.2018.1461595.

[35] W. Dong, H. Pan, Mi. Lei, K. Ding, and Y. Gao. Zn penetration and its coupled interaction with the grain boundary during the resistance spot welding of the qp980 steel. *Scripta Materialia*, 218:114832, 2022. ISSN 1359-6462. doi: https://doi.org/10.1016/j.scriptamat.2022.114832. URL `https://www.sciencedirect.com/science/article/pii/S1359646222003281`.

[36] Z. Ling, M. Wang, L. Kong, and K Chen. Towards an explanation of liquid metal embrittlement cracking in resistance spot welding of dissimilar steels. *Materials Design*, 195:109055, 2020. ISSN 0264-1275. doi: https://doi.org/10.1016/j.matdes.2020.109055. URL `https://www.sciencedirect.com/science/article/pii/S0264127520305906`.

[37] D. Scheiber, K. Prabitz, L. Romaner, and W. Ecker. The influence of alloying on zn liquid metal embrittlement in steels. *Acta Materialia*, 195:750–760, 2020. ISSN 1359-6454. doi: https://doi.org/10.1016/j.actamat.2020.06.001. URL `https://www.sciencedirect.com/science/article/pii/S1359645420304250`.

[38] M.H. Razmpoosh, A. Macwan, F. Goodwin, E. Biro, and Y. Zhou. Crystallographic study of liquid-metal-embrittlement crack path. *Materials Letters*, 267:127511, 2020. ISSN 0167-577X. doi: https://doi.org/10.1016/j.matlet.2020.127511. URL `https://www.sciencedirect.com/science/article/pii/S0167577X20302160`.

[39] T. Auger, S. Hémery, M. Bourcier, C. Berdin, May Martin, and I. Robertson. Crack path in liquid metal embrittlement: Experiments with steels and modeling. *Frattura ed Integrità Strutturale*, 10:250–259, 01 2016. doi: 10.3221/IGF-ESIS.35.29.

[40] Yuki Ikeda, Seungchang Han, Theophilus Wallis, Reza Darvishi Kamachali, and Robert Maaß. On the preference of liquid-metal embrittlement along high-angle grain-boundaries in galvanized steels. *Scripta Materialia*, 265:116723, 2025. ISSN 1359-6462. doi: https://doi.org/10.1016/j.scriptamat.2025.116723. URL `https://www.sciencedirect.com/science/article/pii/S1359646225001861`.

[41] Elahe Akbari, Philipp Kürnsteiner, Katharina Steineder, Martin Gruber, Martin Arndt, Ilse Letofsky-Papst, Robert Sierlinger, and Heiko Groiss. Insight into grain boundaries with reduced liquid metal embrittlement susceptibility in a boron-added 3rd generation advanced high strength steel. *Materials Design*, 237:112584, 2024. ISSN 0264-1275. doi: https://doi.org/10.1016/j.matdes.2023.112584. URL `https://www.sciencedirect.com/science/article/pii/S0264127523010006`.

[42] S.; Mehling C.; Choi-K. W.; Macwan A.; Biro E.; Zhou N. Y. DiGiovanni, C; Bag. Reduction in liquid metal embrittlement cracking using weld current ramping. *Welding in the World*, 63:1583–1591, 2019. ISSN 1878-6669. doi: 10.1007/s40194-019-00790-5. URL `https://doi.org/10.1007/s40194-019-00790-5`.

[43] C. Beal, X. Kleber, D. Fabregue, and M. Bouzekri. Embrittlement of a zinc coated high manganese twip steel. *Materials Science and Engineering: A*, 543:76–83, 2012. ISSN 0921-5093. doi: https://doi.org/10.1016/j.msea.2012.02.049. URL `https://www.sciencedirect.com/science/article/pii/S0921509312002675`.

[44] R. Ashiri, M. Shamanian, H. Reza Salimijazi, Md A. Haque, J.-H. Bae, C.-W. Ji, K.-G. Chin, and Y.-D. Park. Liquid metal embrittlement-free welds of zn-coated twinning induced plasticity steels. *Scripta Materialia*, 114:41–47, 2016. ISSN 1359-6462. doi: https://doi.org/10.1016/j.scriptamat.2015.11.027. URL `https://www.sciencedirect.com/science/article/pii/S1359646215300671`.

[45] Thallada Vinod Kumar and Benjaram Reddy. Catalytic combustion over cheaper metal oxides. *Catalytic Combustion*, pages 105–140, 03 2011.

[46] Stan Lynch. A review of underlying reasons for intergranular cracking for a variety of failure modes and materials and examples of case histories. *Engineering Failure Analysis*, 100:329–350, 2019. ISSN 1350-6307. doi: https://doi.org/10.1016/j.engfailanal.2019.02.027. URL `https://www.sciencedirect.com/science/article/pii/S1350630718314985`.

[47] Michael Piott, Alexandra Werber, Leander Schleuss, Nikolay Doynov, Ralf Ossenbrink, and Vesselin Michailov.

A study of the heat transfer mechanism in resistance spot welding of aluminum alloys aa5182 and aa6014. *The International Journal of Advanced Manufacturing Technology*, 111:1–9, 11 2020. doi: 10.1007/s00170-020-05650-x.

[48] E. Parisa. *Towards intrinsically safe microstructures in resistant spot welded advanced and ultra high strength automotive steels*. PhD thesis, Delt University of Technology, 2019.

[49] Sagar Rathod, Sunil Ghunage, and B. B. Ahuja. A thermo-mechanical finite-element analysis of resistance spot welding of dual-phase steel and austenitic stainless steel. In M. S. Shunmugam and M. Kanthababu, editors, *Advances in Simulation, Product Design and Development*, pages 507–519, Singapore, 2020. Springer Singapore. ISBN 978-981-32-9487-5.

[50] Ki-Nam Jang, Tae-Kyu Kim, and Kyu-Tae Kim. The effect of cooling rates on carbide precipitate and microstructure of 9cr-1mo oxide dispersion strengthened(ods) steel. *Nuclear Engineering and Technology*, 51, 09 2018. doi: 10.1016/j.net.2018.09.021.

[51] Zhanxiang Ling, Min Wang, Liang Kong, and Ke Chen. Towards an explanation of liquid metal embrittlement cracking in resistance spot welding of dissimilar steels. *Materials Design*, 195:109055, 2020. ISSN 0264-1275. doi: https://doi.org/10.1016/j.matdes.2020.109055. URL `https://www.sciencedirect.com/science/article/pii/S0264127520305906`.

[52] Xue Bai, Yun Han, Guangrui Jiang, Huasai Liu, and Yongqiang Zhang. The influence of pre-plating on the lme phenomenon of advanced high strength steel. *Journal of Physics: Conference Series*, 2174:012062, 01 2022. doi: 10.1088/1742-6596/2174/1/012062.

[53] Yaser Rihan, S. Ayyad, and M.I. Elamy. A study on the residual stresses in resistance spot welding. *i-manager's Journal on Material Science*, 3:28–32, 09 2015. doi: 10.26634/jms.3.2.3504.

[54] B-W. Cha and S-J. Na. A study on the relationship between welding conditions and residual stress of resistance spot welded 304-type stainless steels. *Journal of Manufacturing Systems*, 22(3):181–189, 2003. ISSN 0278-6125. doi: https://doi.org/10.1016/S0278-6125(03)90019-7. URL `https://www.sciencedirect.com/science/article/pii/S0278612503900197`.

[55] Parisa Eftekharimilani, H. Gao, R. Huizenga, E.M. Aa, M. Amirthalingam, Ian Richardson, and Marcel Hermans. Residual stress measurements and model validation of single and double pulse resistance spot welded advanced high strength steel. 09 2018.

[56] R. KUZIAK, R. KAWALLA, and S. WAENGLER. Advanced high strength steels for automotive industry. *Archives of Civil and Mechanical Engineering*, 8(2):103–117, 2008. ISSN 1644-9665. doi: https://doi.org/10.1016/S1644-9665(12)60197-6. URL `https://www.sciencedirect.com/science/article/pii/S1644966512601976`.

7. Appendix

The Appendix serves as a deposit for supplementary information that are not essential for a fundamental comprehension of the core study, still provides valuable context, detailed methodologies and expanded datasets. Its inclusion aims to offer readers the opportunity for deeper exploration of specific aspects, without interrupting the primary narrative flow of the main body.

7.1. Electrode shapes

In this section the different Electrode shapes used in RSW are discussed in further detail.

The most common is the Truncated Cone Electrodes, good for general-purpose welding. Good heat-concentration and pressure distribution are usual properties of these electrodes, which are ideal for welding thin or medium thickness sheets [8]. Another type are the dome electrodes, mostly utilized for welding thicker materials with higher thermal conductivity. They provide a better heat distribution and prevent the excessive localized heating to occur. Flat electrodes are also used, especially for very thin sheets or in cases when a large weld nugget is a requirement [8]. Wider heat distribution is provided using flat electrodes, however it is not as commonly used as the previous two types. Radial electrodes are designed for high heat applications, thus provide a very concentrated heat source [8]. Materials with high thermal conductivity are usually welded with this electrode, and it is also used when deep welds are needed [8]. Eccentric and Offset Eccentric electrodes are also used. Eccentric electrodes are mainly used for weldings in corners or confined spaces, with the offset enabling the welding of these difficult-to-reach areas. Thus it is used for components that have complex geometries [8]. The Offset Eccentric Electrodes are similar to the Eccentric ones, however they have a much larger offset. Usually used for welding in tight corners or to reach deep into the workpiece [8]. The required weld size, the thickness and complexity of workpieces and the material's thermal conductivity all affect the choice of electrode [8].

7.2. Power supply components

The power supply used during resistance spot welding has different components. One of these main components is the transformer, which reduces the input voltage to a lower voltage (1-20 V), all while increasing the current to very high values (even up to 10000-100000 A) [8]. This transformation is crucial to generate the required heat during resistance spot welding [8]. The capacitor bank is also an important part, as this is the component that stores the energy, which it releases in short bursts to the welding transformer, basically providing the high current for the welding process [8]. The third main component is the Control System, which regulates the welding process [8]. It does so by controlling the timing of the current pulse, the duration and magnitude of such pulse, and the pressure applied by the electrodes [8].

There are a key factors that affect the performance of the power supply. The transformer capacity is an important one, as it must be able to provide sufficient current and voltage [8]. The capacitor bank size and the control system accuracy also have high importance, as they need to be able to store enough energy for each welding cycle and be able to precisely regulate each cycle [8]. Electrode design must be chosen wisely for each work, and the condition of the electrodes should be monitored regularly to make sure the heat transfer is efficient and no damage is caused [8].

7.3. Types of High Strength Steels discussed in length

In this section the types of high strength steels that were only briefly mentioned in the main text are elaborated further on.

7.3.1. Dual-Phase (DP) steels

Dual-Phase (DP) steels have a distinctive microstructure which consists of a ferritic matrix interspersed with islands of a hard martensitic phase [15]. Due to this, the strength of this steel grade generally correlates directly with the volume fraction of the martensitic phase embedded in the ferritic matrix[56]. These types of steel are usually produced by hot-rolling that is followed by a controlled cooling from the austenite phase that is found in the hot-rolling products. Cold-rolled sheets can also be heat-treated as an alternative, but in this case rapid cooling is needed from the two-phase (austenite-ferrite) region to transform the austenite into martensite. This process can be effectively implemented through continuous production lines equipped with continuous heating/annealing and hot-dip processes for quenching and surface coating [15].

7.3.2. Complex-Phase (CP) Steels

CP steels have very high ultimate tensile strength and complex microstructure, mainly characterized by a small amount of martensite, retained austenite and pearlite, all which are embedded in a ferrite-bainite matrix [15] [56]. This is achieved through extreme grain refinement, which is done through delayed recrystallization or the precipitation of microalloying elements (Ti, Nb). Due to this CP steels have a much higher yield strength and equivalent tensile strengths (approx. 800 MPa) compared to their Dual-Phase counterparts. Their high energy absorption capacity and substantial residual deformation capability are also the signature properties of this steel grade [15].

7.3.3. Martensitic (MS) Steels

Martensitic steel grades undergo an almost complete austenite-martensite transformation during quenching or some form of post-forming heat treatment. The result is a microstructure that has a martensitic matrix with ferrite and bainite fractions, which allow this grade to have the highest strengths among the multiple-phase steel grades, surpassing even 1.6 GPa. Post-quench tempering is a usual process to improve the quality and ductility of the steel [15].

7.3.4. Ferritic-Bainitic (FB) Steels

Ferritic-bainitic steels, also called Stretch Flangeable (SF) or High Hole Expansion (HHE) steels have an enhanced edge stretch capability, due to their microstructure which is built up from bainite and ferrite. Strengthening is done with a combination of grain refinement and second-phase hardening of the bainite. It is also available as a hot-rolled product, as this grade has a higher strain hardening exponent and total elongation than other High-Strength Low-Alloy (HSLA) steels with equivalent strength. The grade possesses an excellent weldability, and also has favourable safety performances and fatigue properties [15].

7.3.5. Transformation-Induced Plasticity (TRIP) Steels

TRIP steels exhibit a unique microstructure comprising retained austenite particles embedded within a ferrite matrix [15] [56]. In addition to the requisite 5% volume fraction of retained austenite, varying amounts of martensite and bainite are typically present, as the production process often involves an isothermal hold at an intermediate temperature, facilitating the formation of bainite. The elevated silicon and carbon content in TRIP steels significantly contributes to the substantial volume fraction of retained austenite in the final microstructure. During sheet forming operations, applied stress or strain induces a transformation from retained austenite to martensite phases, this transformation is accompanied by volume expansion, contributing to enhanced plasticity during stamping, particularly under tensile mean stress conditions [15].

7.4. Hot-Formed (HF) Steels

HF steels are developed to have an enhanced formability and reduced springback. Stamping for this grade is performed at elevated temperatures of 900-950 Celsius, within the austenitic region, which results in excellent formability (elongation up to 50%). Quenching in a water-cooled die will result in high yield strength (above 600 MPa), and ultimate yield strength higher than 1300 MPa at room temperature. Typical stamping cycle times range from 20 to 30 seconds per press cycle. However, multiple parts can be stamped concurrently, allowing for the production of two or more parts per cycle. Hot-formed boron steels are commonly employed for safety and structural components. A surface coating, such as aluminum-silicon, is often applied to form a dense Fe-Al-Si surface layer at elevated temperatures, effectively reducing oxidation [15].

7.5. List of Systems Susceptible to LME

This section discusses the systems susceptible to LME that were left out of the main text due to them not being directly tied to the topic of the research.

Bismuth: Can embrittle several ferrous alloys, with the severity of it being dependent on alloy composition and the heat treatment of the solid metal [20].

Antimony: Embrittles carbon, silicon, and chromium steels at high temperatures, while its presence as an alloying addition to lead significantly enhances embrittlement [20].

Cadmium: Embrittles Zircaloy-2, contributing to cladding failures in nuclear reactors, while also embrittling titanium alloys and steel grades, particularly in tempered and quenched condition [20].

Caesium: Embrittles Zircalo cladding in nuclear fuel elements similar to Cadmium, but does it especially under dynamic loading conditions [20]. There is limited data on how it affects ferrous alloys [20].

Copper: Embrittles various steels, including austenitic stainless steels [20]. Surface cracking of ingots during hot-rolling is a common observation [20].

Indium: It embrittles some of the ferrous metals, with the embrittle temperature being influenced by the microstructure and strength of the metal [20].

Gallium: Embrittles notched mild steel, with limited data on its effect on other materials [20].

Lead: Embrittles several steel grades, with effect increasing with temperature [20]. Alloying additions to lead enhance its embrittling potency [20].

Lithium: Embrittles some steel grades, but corrosion due to carbon and nitrogen solubility complicates the process [20].

Mercury: Embrittles titanium alloys, zirconium, and some ferrous alloys, particularly those with specific microstructural features [20].

Rubidium: Reports show it embrittles Monel 400, but further research is required [20].

Tellurium: It can embrittle steels, especially if the steel is under combined stress and environmental conditions [20]. The observation of effects is complicated by chemical conditions [20].

Tin: Embrittles various steel grades, including austenitic stainless steels, while also enhancing the embrittling effect of lead [20].

Zinc: Embrittles stainless steel grades at high temperatures due to complex mechanisms such as intermetallic formation and different phase transformations [20].

Sodium: There are limited evidence that sodium plays a role in LME in case of steels, however it does effect corrosion and fatigue more commonly [20].

7.6. Grain size distribution diagrams for EBSD measurement of HTT samples

This chapter of the Appendix presents the complete grain size distributions for all analysed samples, showing both area-related and number-fraction-related data. These comprehensive graphical representations are included to provide full accessibility of the experimental outcomes, contrasting with the selective inclusion of specific examples within the main body of the study, a decision made to maintain the research's narrative coherence and flow.

7.6.1. Grain size distribution diagrams - Area

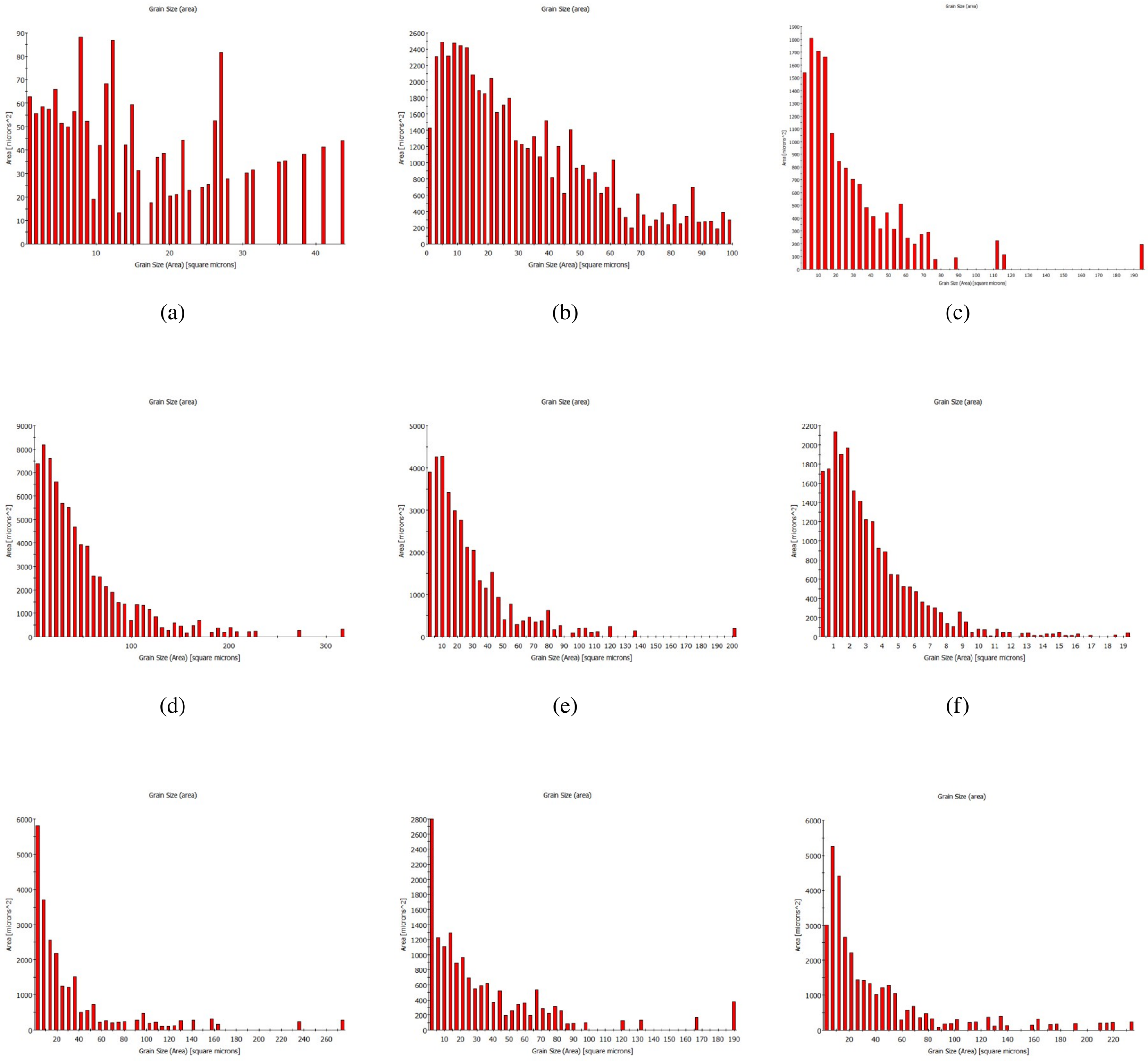

(a) (b) (c)

(d) (e) (f)

(g) (h) (i)

Figure 7.1. Grain size distribution of the (a) Base Material, (b) HT-05 sample, (c) HT-55 sample, (d) HT-105 sample scan 1, (e) HT-105 sample scan 2, (f) HT-155 sample, (g) HT-205 sample, (h) HT-305 sample, (i) HT-355 sample

7.6.2. Grain size distribution diagrams - Number fraction

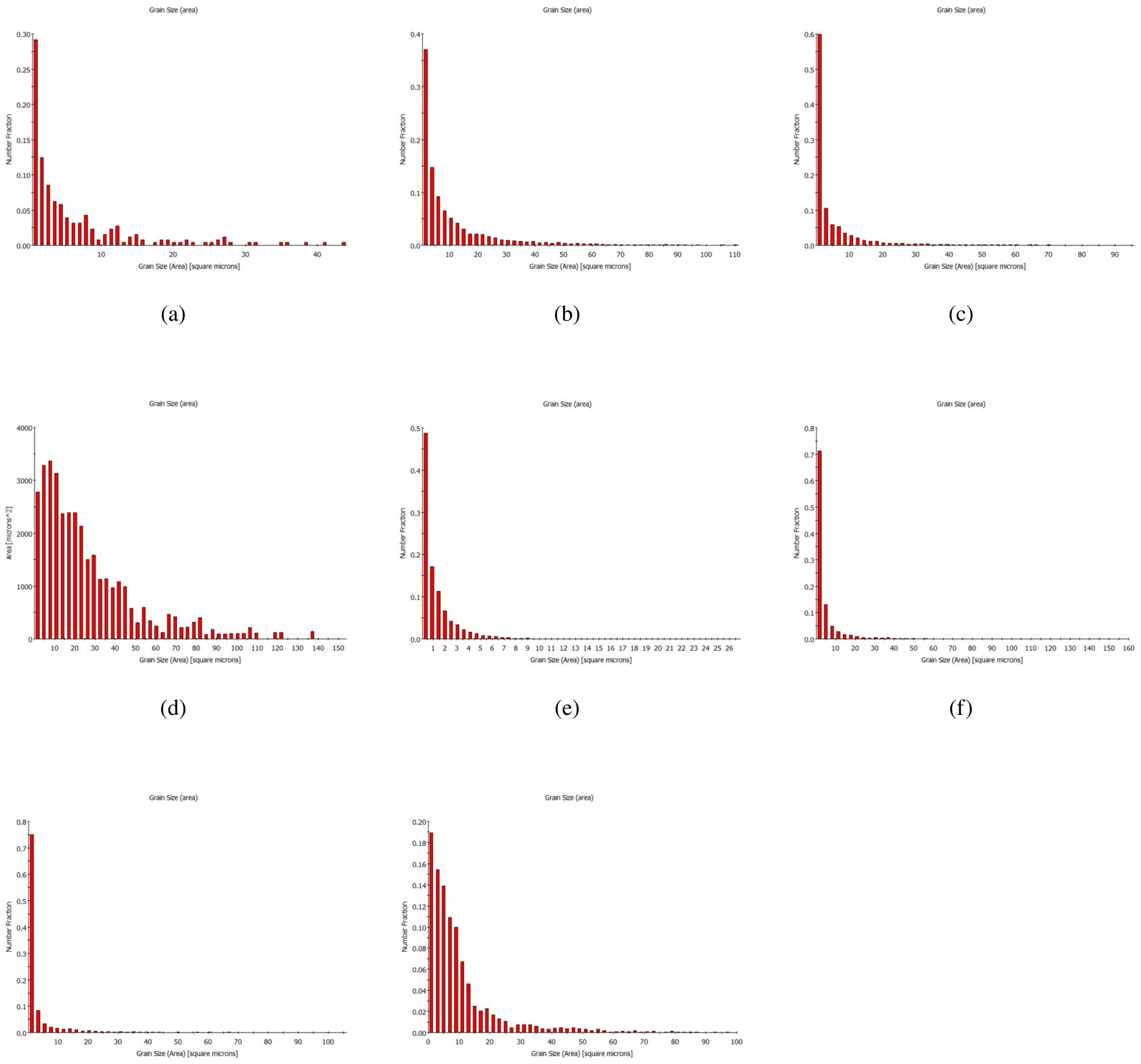

(a)

(b)

(c)

(d)

(e)

(f)

(g)

(h)

Figure 7.2. Grain size distribution - Number Fraction of the (a) Base Material, (b) HT-05 sample, (c) HT-55 sample, (d) HT-105 sample, (e) HT-155 sample, (f) HT-205 sample, (g) HT-305 sample, (h) HT-355 sample